

THESIS

DETECTION OF SMALL NUMBERS OF BARIUM IONS IMPLANTED IN
SOLID XENON FOR THE EXO EXPERIMENT

Submitted by

Shon Cook

Department of Physics

In partial fulfillment of the requirements

For the Degree of Doctor of Philosophy

Colorado State University

Fort Collins, Colorado

Summer 2012

Doctoral Committee

Advisor: William Fairbank

Siu Au Lee

Jacob Roberts

Randy Bartels

ABSTRACT

DETECTION OF SMALL NUMBERS OF BARIUM IONS IMPLANTED IN SOLID XENON FOR THE EXO EXPERIMENT

In an effort to discover the yet-unknown absolute masses of neutrinos, the goal of the Enriched Xenon Observatory is to observe neutrinoless double beta decay of ^{136}Xe . Identification of this very rare decay may be difficult even with the best conventional efforts to reduce and reject radioactive background, thus requiring additional background rejection via detection of the daughter ^{136}Ba nucleus. One method of detection is laser-induced fluorescence of the barium atom in solid xenon.

Spectra of very small numbers of barium atoms in solid xenon, as few as 3 atoms, are reported for the first time. Demonstration of detection of Ba atoms with large fluorescence efficiencies gives promise for detecting single atoms in the near future.

Results from experiments involving implantation of Ba^+ ions in solid xenon are discussed. One narrow excitation peak was discovered from ion beam deposition that was not found in neutral deposits. Five new emission lines are found with this same excitation spectrum. Bleaching, annealing, and laser dependence of these lines are studied. The identification of the new Ba species as Ba^+ or as a barium molecule is discussed.

ACKNOWLEDGEMENTS

I would like to extend my deepest thanks to my advisor, Dr. William Fairbank. Dr. Fairbank has provided me with the opportunity to explore a rich, thought-provoking field of physics, while lending guidance where needed. Working with him has provided me countless wonderful opportunities in the world of physics.

Thesis committee member Dr. Siu Au Lee deserves special thanks for her constant supply of advice, assistance, and occasional loaning of equipment. I also wish to thank Dr. Jake Roberts and Dr. Randy Bartels for being on my committee. Their guidance and inspiration is greatly appreciated.

My fellow graduate students in Dr. Fairbank's group also have my thanks. Kendy Hall, Cesar Benitez-Medina, and Tim Walton have all provided many hours of help. Special thanks are due to Brian Mong, with whom I worked very closely during the course of my graduate school career.

I also wish to thank my family and friends for all of the support given to me over the last several years. Above all, I wish to thank Ms. Thayer Low. Her boundless optimism has been more valuable than I could ever express.

TABLE OF CONTENTS

Abstract	ii
Acknowledgements	iii
1 Introduction	1
1.1 Neutrino Physics	1
1.2 Neutrino Oscillation and Mass	3
1.3 Double Beta Decay	8
1.4 The EXO Experiment	11
1.4.1 EXO 200	12
1.4.2 EXO Full	14
1.4.3 Tagging in SXe	16
1.4.4 Other Tagging Methods	17
2 Theory	22
2.1 Ba^0 , Ba^+ and Ba^{++} Energy Levels	22
2.2 Ba and Ba^+ Interactions with Noble Gas Atoms	26
2.3 Matrix Isolation Spectroscopy	28
2.4 Three Level Model	31
2.5 Ion Implantation in Solid Noble Gases	34
2.6 Fluorescence Efficiency	37
3 Experimental	39
3.1 Ion Beam	39
3.1.1 Ion Source	42
3.1.2 Mass Filter	44

3.1.3	Ion Focusing and Deflection	47
3.1.4	Deceleration	49
3.1.5	Ion Pulsing and Detection	50
3.1.6	Ion Beam Vacuum Generation	55
3.1.7	Neutral Barium Deposition	55
3.2	Cryostat	56
3.2.1	Cryogenic System	56
3.2.2	Gas Deposition	58
3.2.3	Cryostat Vacuum Generation	61
3.3	Optical Setup	62
3.3.1	Lasers and Dye Lasers	62
3.3.2	Collection Optics and Spectrometer	65
3.4	White Light Absorption	69
3.5	Data Collection	71
3.6	Ion Number Calculation and Background Considerations	71
4	Results	74
4.1	Neutral Barium Fluorescence and Absorption in Solid Xenon	74
4.2	Fluorescence Efficiency of Neutral Barium in Solid Xenon	83
4.3	Spectra of Small Numbers of Ba from Ba ⁺ Deposits	84
4.4	Imaging of Barium Atoms	90
4.5	Emission Spectra of Ba ⁺ Implanted in Solid Xenon	95
4.6	Excitation Spectra of Candidate Ba ⁺ Emission Lines	97
4.7	Interpretation of Excitation and Emission Lines of Ba ⁺	101
4.8	Bleaching and Saturation Studies of Ba ⁺	105
5	Conclusion	113
5.1	Summary	113

5.2 Future Work	115
References	115

1 Introduction

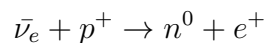
Years after their discovery in the 1930s, neutrinos are some of the most interesting of the elementary particles. Few other particles have remained as enigmatic or undergone so many changes in the scientific community's view as the neutrino. Whether it is their changing of flavor, elusive mass hierarchy, or possible Majorana nature, neutrinos have left a vast field of physics for fascinating experiments to explore. This chapter will discuss the basics of neutrino physics, the double beta decay reaction by which we might learn the absolute neutrino mass, and a new detector to find that double beta decay half life. For such a detector, rejection of all background signals, through positive identification of the daughter products of a double beta decay event, is desired.

1.1 Neutrino Physics

In 1914, it was discovered that the β decay spectrum was continuous [1]. This disagreed with the prevailing theory that β decay was a two-body decay, and should not have a continuous spectrum. In an open letter to a 1930 Tübingen physics conference, Wolfgang Pauli first theorized the existence of a neutral particle of roughly electron mass with spin of $\frac{1}{2}$ in an effort to maintain conservation of energy, momentum, and angular momentum in β decay [2]. Pauli's particle resolved this contradiction, by carrying away the missing energy and angular momentum in the newly theorized particle. Soon after Pauli's proposal, Enrico Fermi published his theory of β decay that incorporated Pauli's particle, dubbing it the "neutrino" in the process [3]. From the shape of the β decay spectrum, Fermi posited that the neutrino was much lighter than the electron, potentially even being entirely massless. In the Standard Model, the neutrino was assumed to be massless.

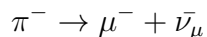
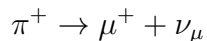
Shortly following Fermi's analysis of the neutrino and the β decay spectrum,

Bethe and Peierls determined that neutrinos born from energies of β decays could penetrate 10^{16} km of solid matter. Thus any process of this kind would be “absolutely impossible to observe” [4] and that “there is no practically possible way of observing the neutrino” [4]. However, a method to detect neutrinos was proposed in 1953 by Cowan and Reines, using a nuclear reactor producing a high neutrino flux [5]. With 10 ft^3 of liquid scintillator surrounded by ninety photomultiplier tubes in the neutrino flux path, Cowan and Reines confirmed in 1956 that neutrinos could, in fact, be detected via a reaction with a proton, producing a neutron and a positron [6]:



with the positron quickly annihilating with an electron. An additional experiment in 1956 by R. Davis, proposed by Alvarez in 1949 [7], showed that two types of neutrinos exist, one being the antiparticle of the other; the electron neutrino (ν_e), which comes from β^+ decay, and the electron antineutrino ($\bar{\nu}_e$), coming from β^- decay [8].

Predicted by several independent groups in the late 1930s [9] [10], the muon neutrino (ν_μ) and muon antineutrino ($\bar{\nu}_\mu$) were first observed by Lederman, Schwartz, and Steinberger at the Brookhaven Alternating Gradient Synchrotron (AGS) [11]. The Danby experiment used a high energy beam of protons from the AGS to create a shower of pions, which then decayed in flight to muons and neutrinos, described by the two reactions:



The muon neutrinos and antineutrinos were observed in a spark chamber located behind an iron shield, through which the muons could not pass.

The discovery of the final flavor of neutrino came in the mid 70’s at the Stanford Linear Accelerator Center by a group led by M. Perl [12]. The SLAC group found

there to be missing energy in the electron-positron reaction $e^+ + e^- \rightarrow e^\pm + \mu^\mp$. Further analysis in 1976 led the group to the conclusion that a new particle was behind the phenomenon [13]. This electron-positron reaction produces what would become known as the tau lepton [14]:

$$e^+ + e^- \rightarrow \tau^+ + \tau^-$$

By analogy with electrons and muons, a corresponding tau neutrino and tau antineutrino; ν_τ and $\bar{\nu}_\tau$ were also expected.

The tau neutrino remained undetected until a Fermilab experiment called DONUT (Direct Observation of the NU Tau) was able to directly observe the particle in July 2000 [15]. The Tevatron particle accelerator was used to create a shower of ν_τ and τ particles, which decayed from D_s mesons. Rarely, a tau neutrino would interact in a nuclear emulsion, allowing for the first observation of this type of neutrino.

1.2 Neutrino Oscillation and Mass

In the late 1960s, experimentalist Ray Davis and theorist John Bahcall started what would come to be known as the Homestake Experiment, with the goal of detecting neutrino interactions from neutrinos emitted from nuclear fusion in the sun. Their detector contained 100,000 gallons of tetrachloroethylene and was located 4850 feet underground in the South Dakota Homestake gold mine. The group used the reaction of

$$\nu_e + {}^{37}\text{Cl} \rightarrow {}^{37}\text{Ar} + e^-$$

The radioactive argon isotope could be removed from the chamber and counted [16]. Physicists working in the Davis group had carefully analyzed the solar model in order to estimate the flux of neutrinos that should go through the experiment, and also the

rate at which neutrinos should be captured by the experiment [17].

The Homestake experiment ran for nearly 25 years, producing a capture rate of 2.56×10^{-36} per target atom per second, or 2.56 Solar Neutrino Unit (SNU) [18]. This was only 27.5% of the 9.3 SNU predicted by Bahcall [19]. Other independently calculated values were also higher than the experimental value, 6.36 SNU (Turck-Chieze and Lopes) [20] and 7.7 SNU (Sackmann, Boothroyd, and Fowler) [21]. After thorough checking of the experimental apparatus and of the solar model, this discrepancy came to be known as the “Solar Neutrino Problem.”

One possibility to account for these “missing” neutrinos was neutrino oscillations, that was first theorized by Pontecorvo in 1957 [22]. Maki, Nakagawa, and Sakata took Pontecorvo’s hypothesis and developed a theory for mixing of neutrino flavors [23], with Pontecorvo adding to the theory again in 1968 [24]. This new theory of neutrino oscillation implied a fascinating new result: if neutrino oscillations are observed, neutrinos would be massive particles, though they had been assumed to be massless in the Standard Model. In 1969, one year after the first Homestake result, Gribov and Pontecorvo published a paper presenting why neutrino oscillations would lead to a decrease in the number of solar neutrinos detected [25].

In the Pontecorvo, Maki, Nakagawa, and Sakata theory, neutrino states of definite flavor are superpositions of states of definite mass, and are related through the so-called PMNS or mixing matrix. Specifically,

$$\begin{pmatrix} \nu_e \\ \nu_\mu \\ \nu_\tau \end{pmatrix} = \begin{pmatrix} U_{e1} & U_{e2} & U_{e3} \\ U_{\mu1} & U_{\mu2} & U_{\mu3} \\ U_{\tau1} & U_{\tau2} & U_{\tau3} \end{pmatrix} \begin{pmatrix} \nu_1 \\ \nu_2 \\ \nu_3 \end{pmatrix}$$

where ν_e , ν_μ , and ν_τ are the flavor eigenstates, and ν_1 , ν_2 , and ν_3 are the mass eigenstates. The mixing matrix, when considering three definite neutrino flavors with

three definite mass eigenstates, is written as

$$U = \begin{pmatrix} c_{12}c_{13} & s_{12}c_{13} & s_{13}e^{-i\delta} \\ -s_{12}c_{23} - c_{12}s_{23}s_{13}e^{i\delta} & c_{12}c_{23} - s_{12}s_{23}s_{13}e^{i\delta} & s_{23}c_{13} \\ s_{12}s_{23} - c_{12}c_{23}s_{13}e^{i\delta} & -c_{12}s_{23} - s_{12}c_{23}s_{13}e^{i\delta} & c_{23}c_{13} \end{pmatrix} \begin{pmatrix} e^{i\alpha_1/2} & 0 & 0 \\ 0 & e^{i\alpha_2/2} & 0 \\ 0 & 0 & 1 \end{pmatrix}$$

where $c_{ij} = \cos \theta_{ij}$ and $s_{ij} = \sin \theta_{ij}$, with θ_{ij} indicating the mixing angle between two eigenstates i and j [26]. The quantity δ is a phase factor for violation of charge-parity symmetry. In the second matrix, α_1 and α_2 are ‘‘Majorana Phases,’’ and have meaning only if the neutrino is a Majorana particle, meaning it is its own antiparticle. These phases are important in the effective mass parameter $\langle m_\alpha \rangle$ measured in double-beta decay, as can be seen in Equation 1.1 [27]:

$$\langle m_\alpha \rangle = \left| \sum_i U_{\alpha i}^2 m_i \right| \quad (1.1)$$

where α is the neutrino flavor (e , μ , or τ).

A neutrino of type α before any propagation (at position $x = 0$ and time $t = 0$) is a combination of the mass eigenstates i :

$$|\nu_\alpha(0, 0)\rangle = \sum_i U_{\alpha i} |\nu_i\rangle$$

As the neutrino propagates, its state is determined by the translation operator $e^{-i(Ht - \vec{P}\cdot\vec{r})}$.

Therefore at time x and time t , the state of the neutrino is determined by [28]:

$$|\nu_\alpha(x, t)\rangle = \sum_i U_{\alpha i} e^{-i(E_i t - p_i x)} |\nu_i\rangle$$

where the energy E_i and the momentum p_i are determined by how the neutrino is produced. The probability of a neutrino of flavor α to oscillate to a β type neutrino

is then the square of the projection of $|\nu_\alpha(x, t)\rangle$ onto $|\nu_\beta(0, 0)\rangle$:

$$P(\nu_\alpha \rightarrow \nu_\beta)(x, t) = \left| \sum_i U_{\beta i}^* U_{\alpha i} e^{-i(E_i t - p_i x)} \right|^2$$

There are cases where, approximately, only two mass eigenstates mix. In these cases, the mixing matrix is simplified to a 2×2 matrix:

$$U = \begin{pmatrix} \cos \theta & \sin \theta \\ -\sin \theta & \cos \theta \end{pmatrix}$$

The probability of a neutrino of flavor α to oscillate to a β type neutrino is then given by

$$P(\nu_\alpha \rightarrow \nu_\beta) = \sin^2(2\theta) \sin^2\left(\frac{\Delta\phi}{2}\right)$$

where $\Delta\phi = \Delta Et - \Delta px$. The energy and momentum of the wave packet (E^c and p^c) are assumed to be the average of their respective components \bar{E} and \bar{p} . This allows for the velocity of the packet to be described as $v = \frac{E^c}{p^c}$. The difference $\Delta\phi$ is then simplified to:

$$\Delta\phi = \frac{\Delta m^2 x}{2\bar{p}}$$

where Δm^2 is the difference of the squares of the masses of the two neutrinos.

In 1975, Wolfenstein [29], with additional work by Mikheyev and Smirnov in 1985, proposed that neutrinos passing through matter would have a different rate of flavor oscillation than in vacuum [30]. This oscillation modification came to be known as the MSW-effect.

There have been many experiments over the last decade to test neutrino oscillation and find the mixing angles and mass squared differences Δm_{ij}^2 . Notably among these are the KEK to Kamioka Long Baseline Neutrino Oscillation Experiment (K2K), Super Kamiokande, the Sudbury Neutrino Observatory (SNOlab), the Kamioka Liquid-

Table 1.1: Summary of results of neutrino oscillation experiments.

Measurement	Value
$\sin^2 \theta_{12}$	$0.320^{+0.015}_{-0.017}$
$\sin^2 \theta_{13}$	$0.026^{+0.003}_{-0.004}$
$\sin^2 \theta_{23}$	$0.49^{+0.08}_{-0.05}$
$m_2^2 - m_1^2$	$7.62 \pm 0.19 \times 10^{-5} eV^2$
$ m_3^2 - m_1^2 $	$2.53^{+0.08}_{-0.10} \times 10^{-3} eV^2$

scintillator Anti-Neutrino Detector (KamLAND), the Tokai to Kamioka (T2K) experiment, the Daya Bay Reactor Neutrino Experiment, and the Main Injector Neutrino Oscillation Search (MINOS). These results are summarized in Table 1.1 [31]. Though these experiments test neutrino oscillations and mass squared differences, they can not give any information on the absolute neutrino mass. Finding the absolute neutrino mass requires a different technique than those used in oscillation experiments. While the sign of Δm_{21}^2 is known, that of Δm_{31}^2 is not. This leads to two possibilities of mass hierarchies. The “normal” hierarchy has ν_3 above ν_1 and ν_2 , whereas the “inverted” hierarchy positions ν_1 and ν_2 above ν_3 , as shown in Figure 1.1.

Though the differences in the squares of the neutrino masses are known, the absolute masses, in addition to δ and the Majorana Phases α_1 and α_2 , are not. This leaves the neutrino mass as a major unanswered question in physics. Methods such as probing the nuclear beta decay endpoint or detection of neutrinoless double beta decay could provide the additional information needed for finding the masses. If the absolute neutrino masses are found to be in the 1 eV range or above, the mass differences are small, with the masses of all of the neutrino types being very close compared to the absolute mass. This scenario is known as degenerate neutrino masses. With absolute masses in the 1 meV range, the mass squared differences provide a much larger spread

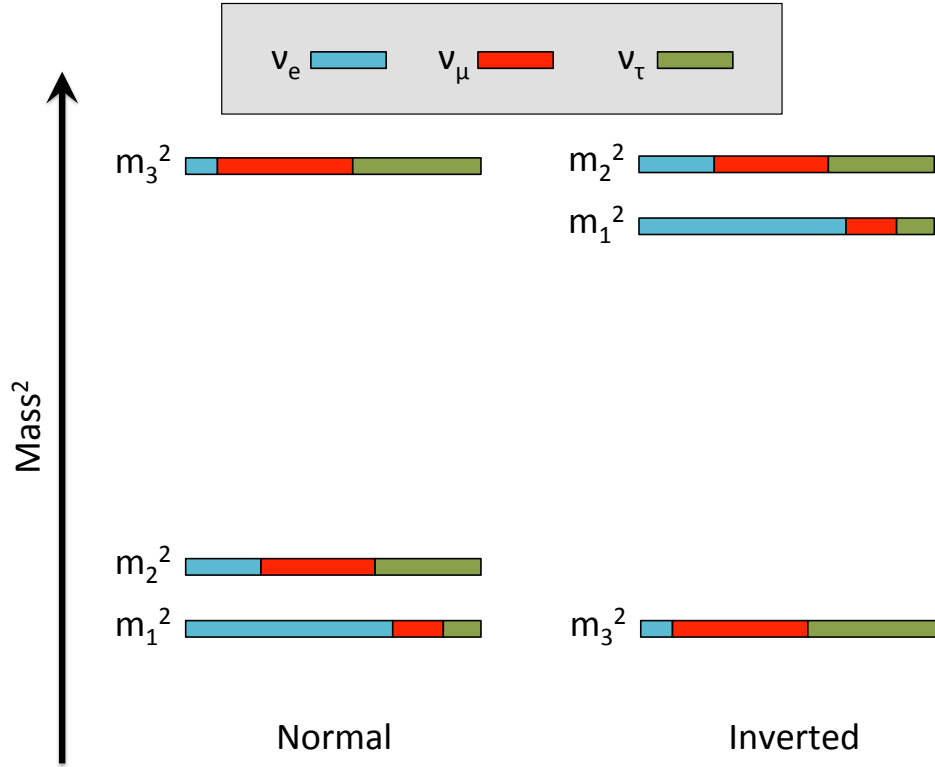


Figure 1.1: Two possible neutrino mass hierarchies.

in neutrino masses.

1.3 Double Beta Decay

Double beta minus decay occurs when two neutrons in a nucleus simultaneously decay into two protons and two electrons, with other exotic, light, neutral particles possibly being produced as well. This decay can occur in two basic forms. In two neutrino double beta decay ($2\nu\beta\beta$), two electrons are emitted along with two electron antineutrinos:

$$(Z, A) \rightarrow (Z + 2, A) + 2e^- + 2\bar{\nu}_e$$

This decay is allowed by the Standard Model, and lepton number is conserved [32]. The $2\nu\beta\beta$ reaction has been observed in about a dozen isotopes, with half-lives in the range of 10^{18} to 10^{21} years [33].

In zero neutrino double beta decay ($0\nu\beta\beta$) two electrons and no neutrinos are emitted:

$$(Z, A) \rightarrow (Z + 2, A) + 2e^{-}$$

This process requires the antineutrino to change from right handed helicity to left handed helicity and become a neutrino, and then be absorbed in the second reaction, as shown with the $0\nu\beta\beta$ reaction in Figure 1.2. Lepton number is not conserved in this decay, and the reaction is forbidden by the Standard model. This zero neutrino decay is yet to be observed, aside from a controversial claim by part of the Heidelberg-Moscow Experiment collaboration [34].

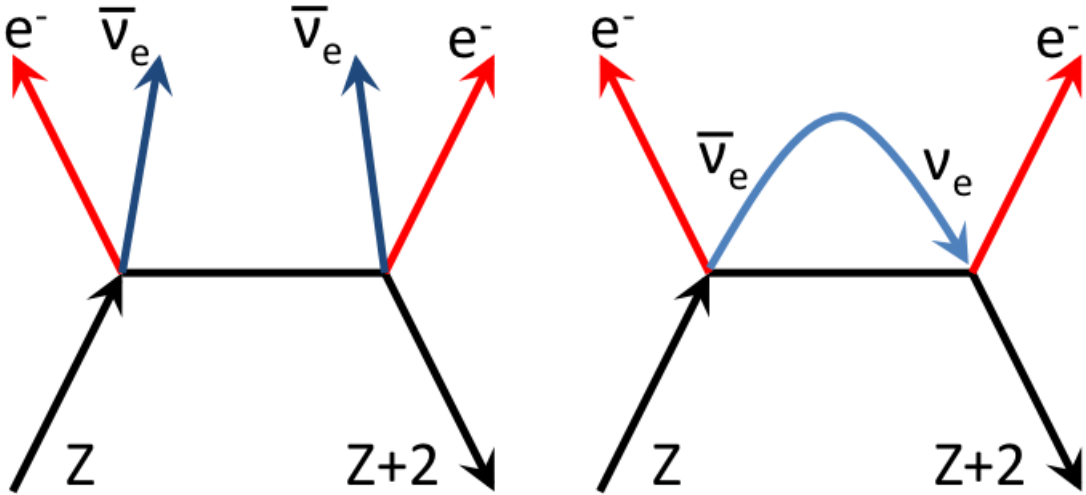


Figure 1.2: Two modes of double beta decay. $2\nu\beta\beta$ is on the left, $0\nu\beta\beta$ on the right. Note that only two electrons are emitted in the 0ν case.

In $2\nu\beta\beta$ decay, the summed electron kinetic energy (K_e) is a continuous spectrum, peaked at a value less than the total energy of the decay (Q). The $0\nu\beta\beta$ spectrum, on the other hand, is a sharp peak with the electron kinetic energy occurring at one

value with very little spread. These two energy spectra are shown in Figure 1.3 [32].

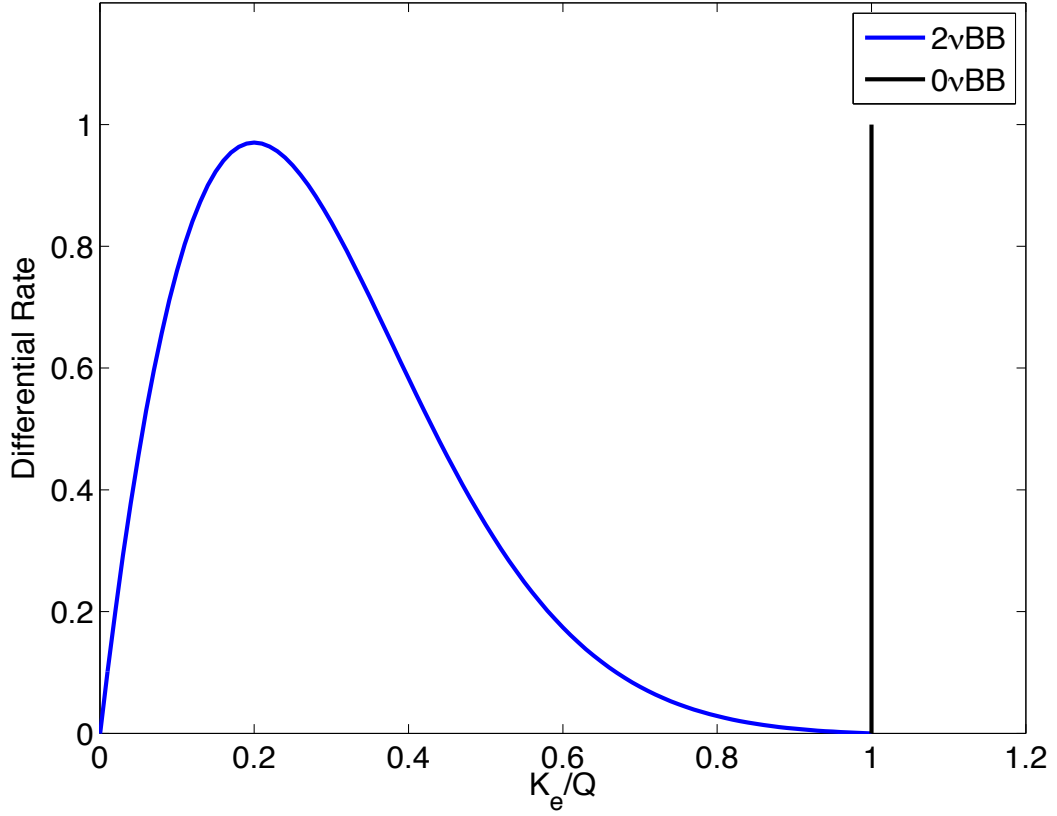


Figure 1.3: Summed electron kinetic energy spectra for the $2\nu\beta\beta$ and $0\nu\beta\beta$ decays. The $2\nu\beta\beta$ spectrum is spread out, and centered at $K_e/Q < 1$, while the $0\nu\beta\beta$ energy is only at $K_e/Q = 1$

If neutrinoless double beta does happen, and neutrinos are, in fact, Majorana particles, the $0\nu\beta\beta$ half-life can be related to the effective neutrino mass as [32]

$$T_{1/2}^{0\nu} = [G^{0\nu}(Q, Z)|M^{0\nu}|^2\langle m_\nu \rangle^2]^{-1}$$

where $G^{0\nu}(Q, Z)$ is a phase space factor dependent on the decay energy Q and the nuclear charge Z , $M^{0\nu}$ is a nuclear matrix element, and $\langle m_\nu \rangle$ is the effective neutrino

mass:

$$\langle m_\nu \rangle = \left| \sum_i U_{\nu i}^2 m_i \right|$$

Because the rate of $0\nu\beta\beta$ decays scales as Q^5 , and the $2\nu\beta\beta$ rate scales as Q^{11} [35], it is important to have a decay with a high Q value in order to observe such rare decays. Assuming an effective neutrino mass in the sub-eV range, a decay half-life of 10^{24} years or longer may be expected. In order to have an experimental time scale of reasonable magnitude, an experiment to measure a half life on this magnitude would require a significant isotopic mass. It is therefore beneficial for the isotope used to be abundant. ^{136}Xe is a promising candidate for use in a $0\nu\beta\beta$ search, considering its high Q value of 2.458 MeV and the natural isotopic abundance of 8.9% [35], . The xenon isotope undergoes double beta decay to ^{136}Ba .

1.4 The EXO Experiment

The Enriched Xenon Observatory (EXO) is an experiment that utilizes a time projection chamber (TPC) to detect the electrons from the $0\nu\beta\beta$ and $2\nu\beta\beta$ decay modes of ^{136}Xe into ^{136}Ba . The first generation experiment, called EXO-200, utilizes 175 kg of xenon enriched to 80% in the 136 isotope. It is currently taking data underground at the Waste Isolation Pilot Plant (WIPP) in Carlsbad, New Mexico. The second generation experiment, EXO Full, will feature one to ten tons of the isotope, and is planned to run from five to ten years. EXO Full is currently in the planning and development phase. To eliminate background, it is designed to feature a method of tagging individual barium decay daughters. If the TPC detects an event, and a barium daughter is successfully tagged from that event, it is then known to be a $0\nu\beta\beta$ or $2\nu\beta\beta$ event. If no barium daughter is tagged after an event, it would likely be a radioactive background event.

1.4.1 EXO 200

The EXO 200 detector is a time projection chamber containing 175 kg of enriched xenon in the liquid phase. This TPC, shown in Figure 1.4, measures 40 cm in diameter and 44 cm in length. It is divided in the middle by a cathode wire plane held at -8 kV, with field shaping rings on either side to keep that field uniform. Each end of the detector contains a plane of avalanche photo-diodes (APD), that collect scintillation light produced in the process of neutralization of ionized xenon. In front of the APD plane, there are two wire grids crossed at 60° to collect the electron signal from ionization. A photograph of the partially constructed TPC is presented in Figure 1.5.

Because the TPC is a liquid-phase detector, it is kept at 167 K. Copper is used for the vessel's body. To reduce the rate of background events, the copper used in constructing the TPC is both as thin as possible at 1.37 mm, and as radio-pure as possible, as were all materials used in the assembly of the experiment. Surrounding the TPC is approximately 50 cm of HFE7000 fluid, used as a heat transfer medium, radiation shield, and pressure equalizing material. The 2300 liters of HFE are contained in a low-background copper cryostat, cooled by closed cycle refrigerators. A computer control system controls the HFE and xenon pressures to be within tens of torr of each other. The cryostat is vacuum insulated and surrounded by a lead shield for further background reduction.

The EXO 200 TPC, cryostat, and all supporting equipment are housed in cleanrooms located in the Waste Isolation Pilot Plant (WIPP) in Carlsbad, New Mexico. The WIPP mine is a salt mine, with the experiment located at 1600 meters of water equivalent depth. The cleanroom is surrounded by panels for detecting cosmic ray muons for further vetoing of false signals. The energy calibration system uses a variety of radioactive isotopes deployed to several different positions around the TPC.

After an engineering run using natural xenon was performed in the fall of 2010,

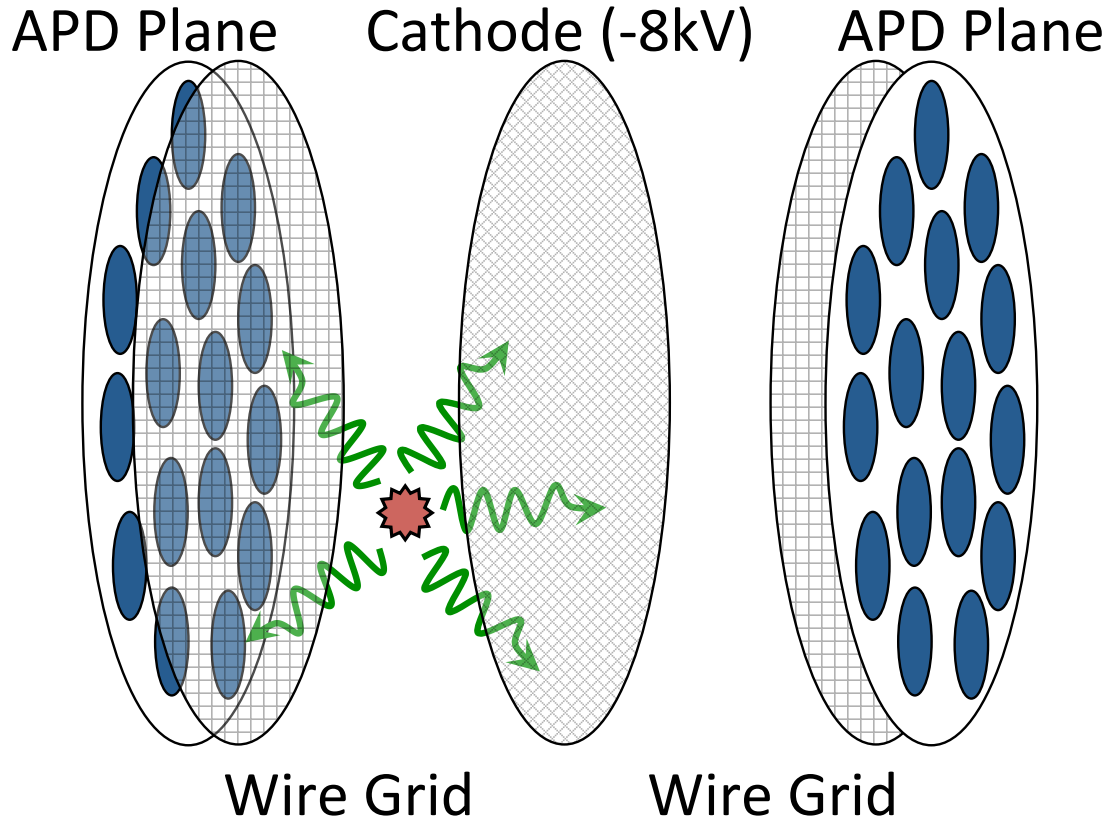


Figure 1.4: Schematic diagram of the EXO-200 detector. Light from a decay is collected by the APDs, while the wire grids collect charge from the reaction.

the TPC was filled with isotopically enriched xenon in early 2011. The experiment has been taking data nearly constantly since then. A publication in August of 2011 reported the discovery of $2\nu\beta\beta$ in ^{136}Xe with this detector, with a half life of $T_{1/2}^{2\nu} = 2.11 \pm 0.04 \pm 0.21 \times 10^{21}$ years [36]. This is the first measurement of $2\nu\beta\beta$ for this nucleus. The EXO 200 experiment also resulted in the EXO collaboration releasing, in a paper accepted for publication by Physical Review Letters, a limit on the neutrinoless double beta decay half-life of $T_{1/2}^{0\nu\beta\beta} \geq 1.6 \times 10^{25}$ years [37]. This limits the effective Majorana masses to less than 140 to 380 meV, depending on the matrix element calculation.

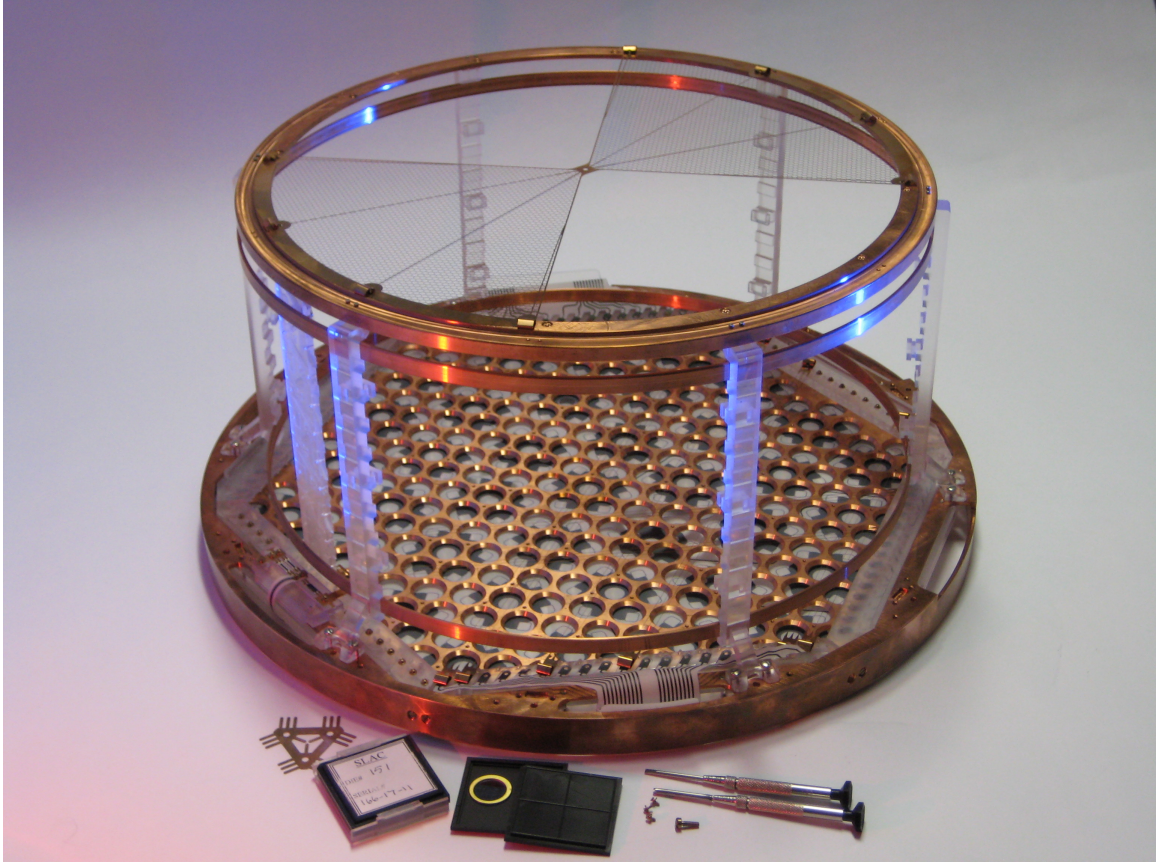
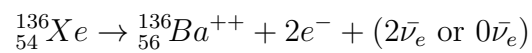


Figure 1.5: Picture of one half of the EXO-200 time projection chamber. Field shaping rings, wire grids, and avalanche photodiodes are not present in this picture.

1.4.2 EXO Full

EXO Full is expected to improve on EXO 200 in several key areas. The mass of enriched xenon will be increased from 175 kg to 1 to 10 tons, and it will run as long as 10 years.

A major improvement anticipated for EXO Full over EXO 200 is the addition of barium daughter tagging. In the double beta decay of ^{136}Xe ,



a $^{136}\text{Ba}^{++}$ daughter ion is produced, in addition to two electrons. The Ba^{++} is ex-

Table 1.2: Sensitivities and parameters for various EXO experiment setups. The rightmost two columns list the predicted neutrino mass using the Quasiparticle Random Phase Approximation (QRPA) and Nuclear Shell Model (NSM) nuclear matrix element calculation methods.

Experiment	Mass (ton)	Run Time (year)	Bkg. (events)	$T_{1/2}^{0\nu}$ (year)	Majorana mass (meV)	
					QRPA [38]	NSM [39]
EXO 200	0.2	2	40	6.4×10^{25}	133	186
Full (cons.)	1	5	0.5	2×10^{27}	24	33
Full (aggr.)	10	10	0.7	4.1×10^{28}	5.3	7.3

pected to quickly decay to Ba^+ in liquid xenon, as the ionization potential of Ba^+ , 10 eV, is higher than the band-gap of liquid xenon, 9.3 eV. As no other background decays except a fraction of an event (on average) from the tail of the $2\nu\beta\beta$ spectrum at the Q value produce a ^{136}Ba daughter, requiring such a signal could eliminate essentially all background. Such background counts could come from the radioactive decay chains of ^{238}U or ^{232}Th , which can be found in materials used for construction of the experiment, and ^{222}Rn in the air or the liquid xenon. Elimination of these false positive events at high certainty is of vital importance to the EXO Full experiment.

Parameters for EXO Full are summarized in Table 1.2 [40]. With one to ten tons of liquid xenon, running for a much longer period of time, and barium tagging removing nearly all background events around the energy region of interest, the neutrino mass sensitivity reaches 5 to 33 meV.

In all the barium tagging schemes proposed for EXO Full, appropriately tuned lasers induce fluorescence in the Ba^+ daughter or Ba daughter, if it further neutralizes in the xenon. Detection of a burst of fluorescence at the appropriate location then provides confirmation of the decay. Detecting the fluorescence in-situ in the TPC, or extracting the ion from the TPC for detection later both require groundbreaking new work in the field of atomic spectroscopy and single ion detection.

1.4.3 Tagging in SXe

This thesis focuses on tagging of the barium daughter in solid xenon. This process is shown schematically in Figure 1.6. After a decay event, photons are detected by the APD planes (Figure 1.6 A). Some time later, the ionization from the decay is detected by the wire planes (Figure 1.6 B). These two pieces of information give the x, y, and z coordinates of the decay, and the probe is inserted in the region of the decay (Figure 1.6 C). A voltage may be applied to the tip to draw the daughter ion to the probe, where it is then frozen in solid xenon as the tip is cooled just below the freezing point of xenon (Figure 1.6 D). A small volume of xenon is frozen around the barium ion, and the tip can then be removed from the TPC, or the barium could be detected on the tip in the TPC.

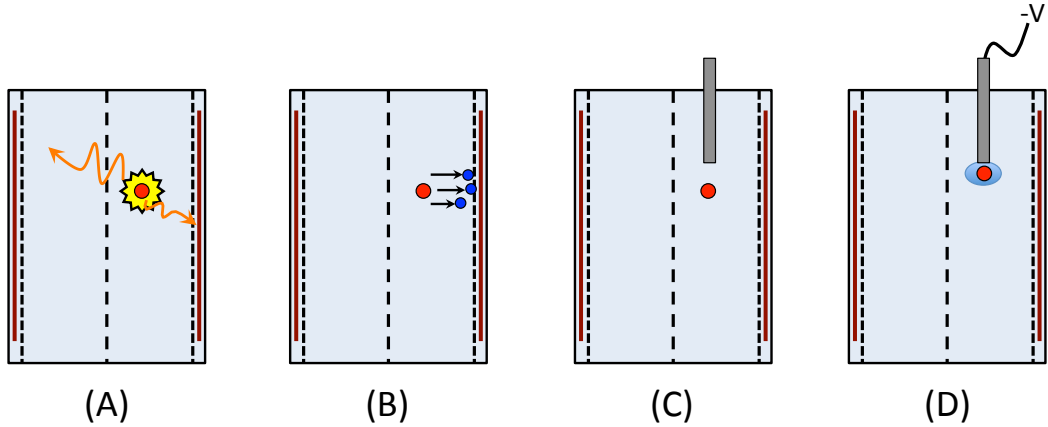


Figure 1.6: Schematic diagram for grabbing a barium daughter from the TPC. (A) A decay releases photons which are detected by the APD planes. (B) Ionization drifts to and is detected by the wire grids. (C) A probe is inserted to the region of the decay. (D) The probe draws an ion near and freezes it in a ball of xenon ice.

There are two possible optical schemes for solid xenon tagging that have been considered. As shown on the left in Figure 1.7, one would be to have an optical fiber carry the laser light to the atom through the cold probe. The fluorescence could be collected back through the fiber. The fluorescence is then decoupled from

the laser light through a dichroic filter and detected. A method of decoupling the fluorescence from the laser light is shown in Figure 1.8. A dichroic mirror passes the red-shifted fluorescence, while reflecting the laser light. A Raman filter further reduces any laser light scatter in the transmitted light. Finally, the fluorescence is passed through a spatial filter to discriminate signal from background scatter before going to the detector, which might be an APD or photomultiplier. The alternate possibility, shown on the right in Figure 1.7, is to use the cold probe merely as a cold tip, with the laser light entering the solid xenon from the front or from the side. In this tagging scheme a focused excitation laser could be scanned across the frozen xenon. The fluorescence could be collected through the same lens, and spectrally decoupled from the laser light. With a broader laser beam, it might be possible to image the fluorescence from barium atoms or ions in the whole xenon ice ball, thus reducing the complexity and duration of the barium detection process.

As it is not known if the Ba^+ ion will neutralize in the solid xenon, it is crucial to know the fluorescence and excitation characteristics of neutral barium atoms in solid xenon as well as those of barium ions in solid xenon. This new, interesting field of research under the EXO experiment is being pursued at Colorado State University. Tagging in solid xenon would have the benefit of needing only minimal manipulation of the barium daughter ion, with the drawback of requiring pioneering of a new technology.

1.4.4 Other Tagging Methods

Along with tagging in solid xenon, several other tagging methods are being pursued in the EXO collaboration, with the goal of finding at least one method that satisfies the tagging requirements. Barium ions might be tagged in-situ in a liquid phase TPC, shown schematically in Figure 1.9 A. When a decay occurs, and its position known from the TPC signal, an appropriately tuned laser could be positioned

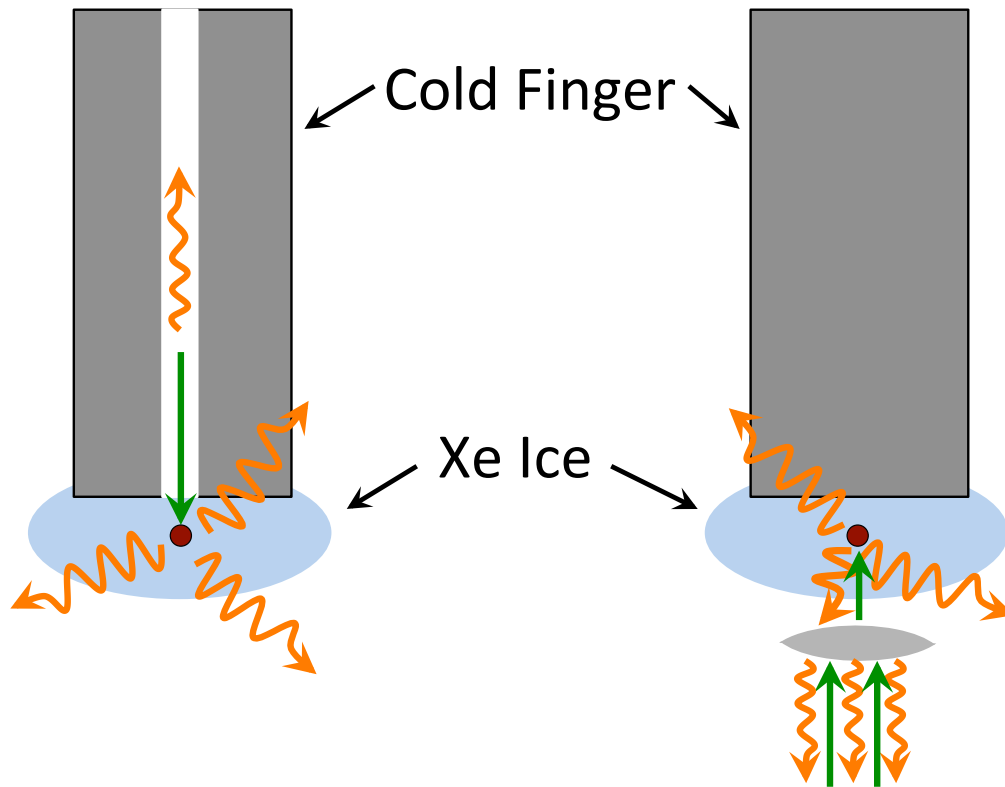


Figure 1.7: Two possible schematics for barium tagging in solid xenon. The method shown on the left collects light through an optical fiber located in the cold tip, while the right collects light through a lens located close to the sample.

to excite the barium ion, with fluorescence being detected by a photon counting detector. This approach has the benefit of not needing to transport the ion. The LXe tagging scheme is currently being pursued at CSU.

The grabber and trap method is shown in Figure 1.9 B. Using a cold probe, the barium ion may be drawn to and frozen on the tip in the chamber, with the position of the decay known from the x , y , and z spatial coordinates given by the TPC. If the grabber is then removed from the TPC, the barium may be released into a linear ion trap by carefully heating the cryo-tip. Once in the ion trap, the barium ion can be detected via laser induced fluorescence with wavelengths of vacuum barium ions. The Stanford group in the EXO experiment has pursued this method, and have

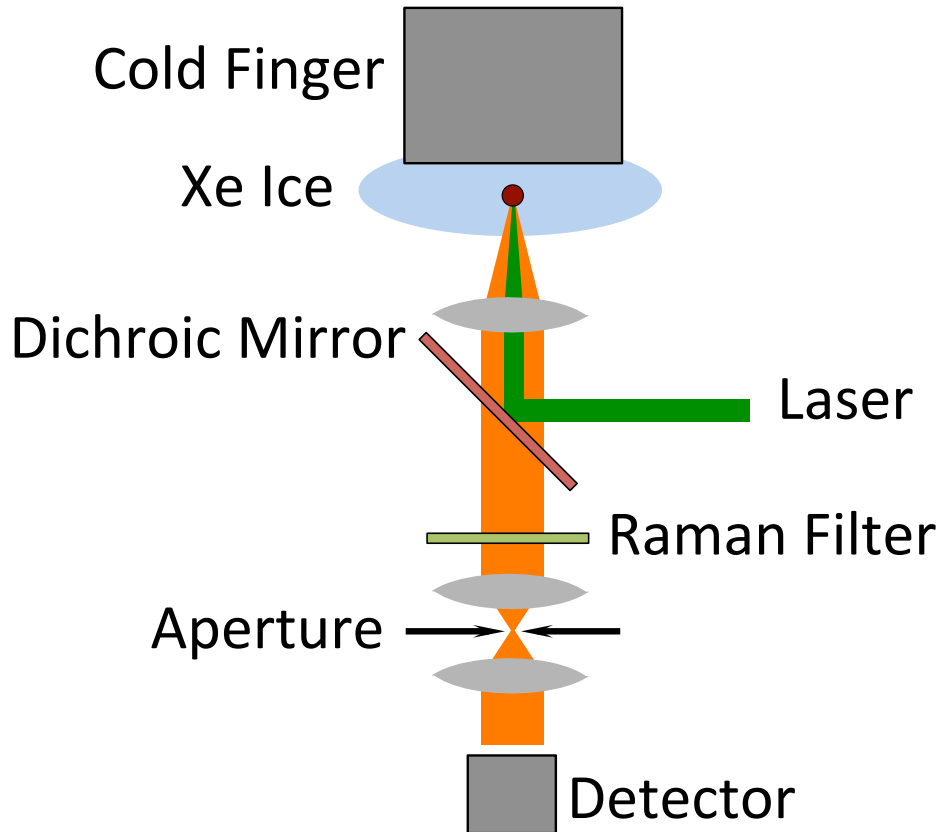


Figure 1.8: A method for separating laser light from fluorescence light for a barium daughter.

demonstrated the ability to trap and detect single Ba^+ ions. However, attempts to load Ba^+ into the trap from xenon ice were unsuccessful. The SLAC and Stanford groups are also investigating a tagging scheme for a gas-phase EXO experiment, shown in Figure 1.9 C. In this scheme, the barium ion is extracted from the 5 to 10 atmosphere TPC through a series of small nozzles to a section at vacuum, where it could be caught in the ion trap and detected with laser induced fluorescence. This approach is currently in the modeling and design phase, with some early proof-of-concept experiments underway.

A laser desorption and resonant ionization spectroscopy (RIS) method of tip release is also being pursued at Stanford, as shown in Figure 1.9 D. In this method,

the barium ion would be stuck on the probe with no xenon ice or gas. The Ba^+ ion would likely neutralize. A desorption laser would remove the barium atom from the probe. Immediately following desorption, the atom would be ionized by two lasers, one exciting it to the $6s6p\ ^1P_1$ state with a 553.5 nm laser, and another laser at 389.7 nm to ionize the atom. The ion is then caught in the ion trap as mentioned above, where it may be detected by laser induced fluorescence. A hot probe method of Ba release and ionization is also being explored at Stanford and SLAC.

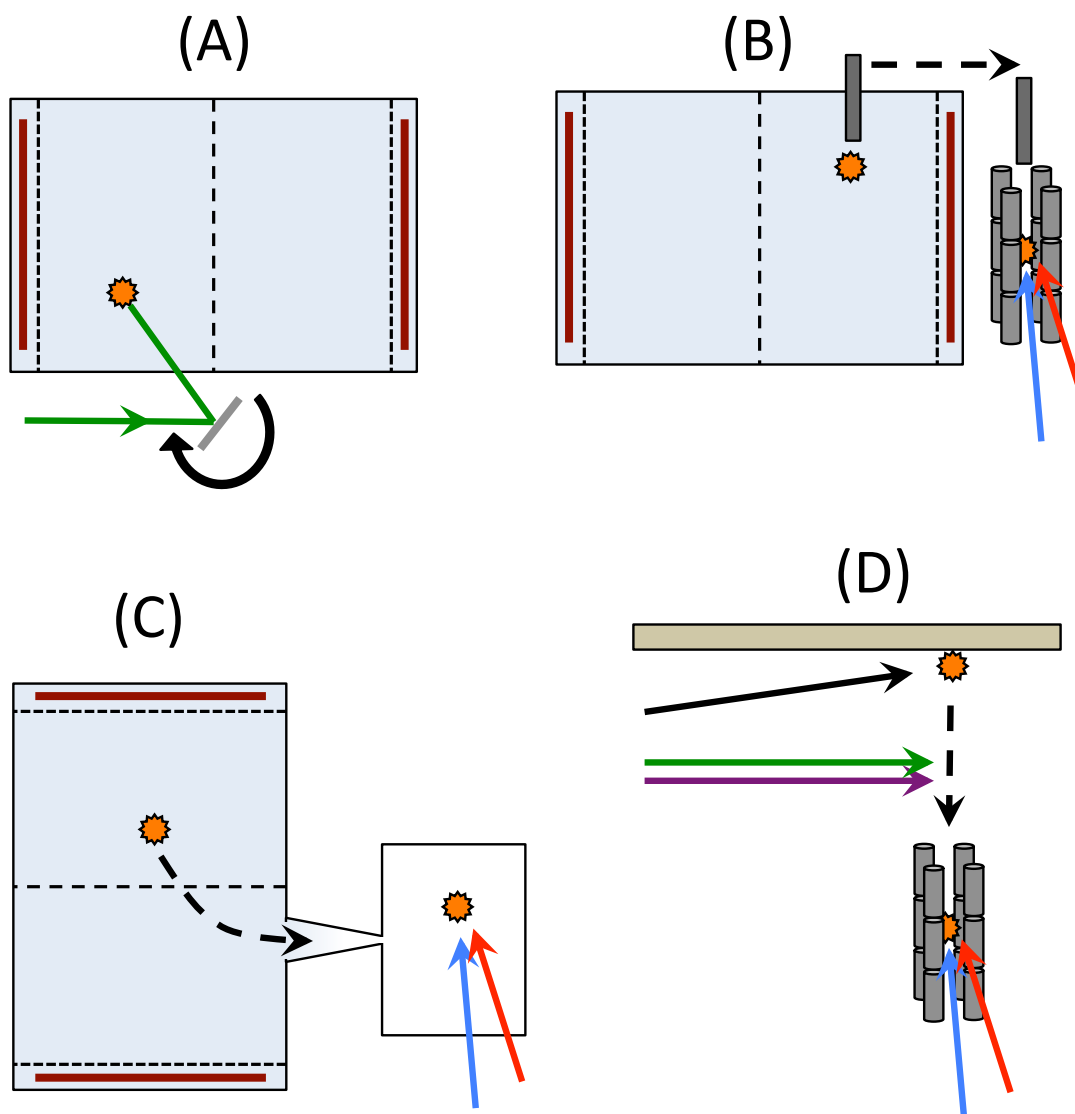


Figure 1.9: Schematics for other tagging methods for the EXO experiment. Schematic (A) shows an in-situ tagging method in the liquid xenon TPC, with the green arrow representing the laser. Diagram (B) shows the grabber and trap method, which utilizes a cold probe to trap the ion in solid xenon. The tip is then removed, and the SXe melted, placing the barium ion in a linear ion trap, where excitation lasers, represented by the blue and red arrows, are tuned to vacuum Ba^+ wavelengths. The high-pressure gas detector is shown in (C), with the blue and red arrows again representing excitation wavelengths. The RIS method, shown in (D), is a possible method for removing the barium atom from a surface with no xenon ice. The desorption laser is shown as a black arrow, while the two ionization lasers are represented by the green and purple arrows.

2 Theory

In order to detect single Ba daughter ions or atoms from double beta decay in a solid xenon matrix, it is necessary to understand the atomic physics of these species and the effects of the solid xenon matrix on these properties. In Section 2.1, the energy levels and transitions of barium ions and atoms in vacuum are presented. In Section 2.2 and Section 2.3, the effects of a solid noble gas matrix on atomic and ionic spectra are discussed. A three-level model is used to derive decay and saturation curves due to optical pumping in Section 2.4. Section 2.5 briefly discusses the difficulties encountered when implanting ions in noble gas matrices. Finally, Section 2.6 covers the calculation of fluorescence efficiencies, as well as absorption cross sections.

2.1 Ba^0 , Ba^+ and Ba^{++} Energy Levels

The energy levels in vacuum for Ba^0 , Ba^+ , and Ba^{++} are well known. Barium neutral atoms, as well as Ba^+ and Ba^{++} ions, feature full xenon-like electron shells with two, one, or zero valence electrons, respectively.

The lowest energy levels of the neutral barium atom and allowed transitions between them are shown in Figure 2.1. Transitions are tabulated in Table 2.1. The strongest excitation line from the ground state to the excited state ($6s^2 \ ^1S_0 \rightarrow 6s6p \ ^1P_1$) occurs at 553.5 nm. Decay of this excited state usually occurs via emission of a 553.5 nm photon, though the electron may also decay to a set of metastable D-states with the emission of a photon in the infrared (either 1.1 or 1.5 μm). These $6s5d \ ^1D_2$ and $6s5d \ ^3D_{1,2,3}$ states are metastable because the even parity of these states is the same as that of the ground state. Electric dipole selection rules for strong transitions dictate that there must be a change in parity; from even to odd, or odd to even, but not from one type to the same type. As such, transitions from the D-states to the

ground state are forbidden. Though the electrons do eventually decay to the ground state from these metastable states, the lifetime is very long compared to an allowed transition. The two step process of exciting atoms to the $6s5d$ states, where they are stuck for a long time, is known as optical pumping. It could be problematic for single barium atom detection. If the atom is pumped into a long-lived state for a high percentage of the time, the fluorescence signal is greatly reduced. One method of overcoming this is to use a re-pumping laser to excite the atom out of the metastable state.

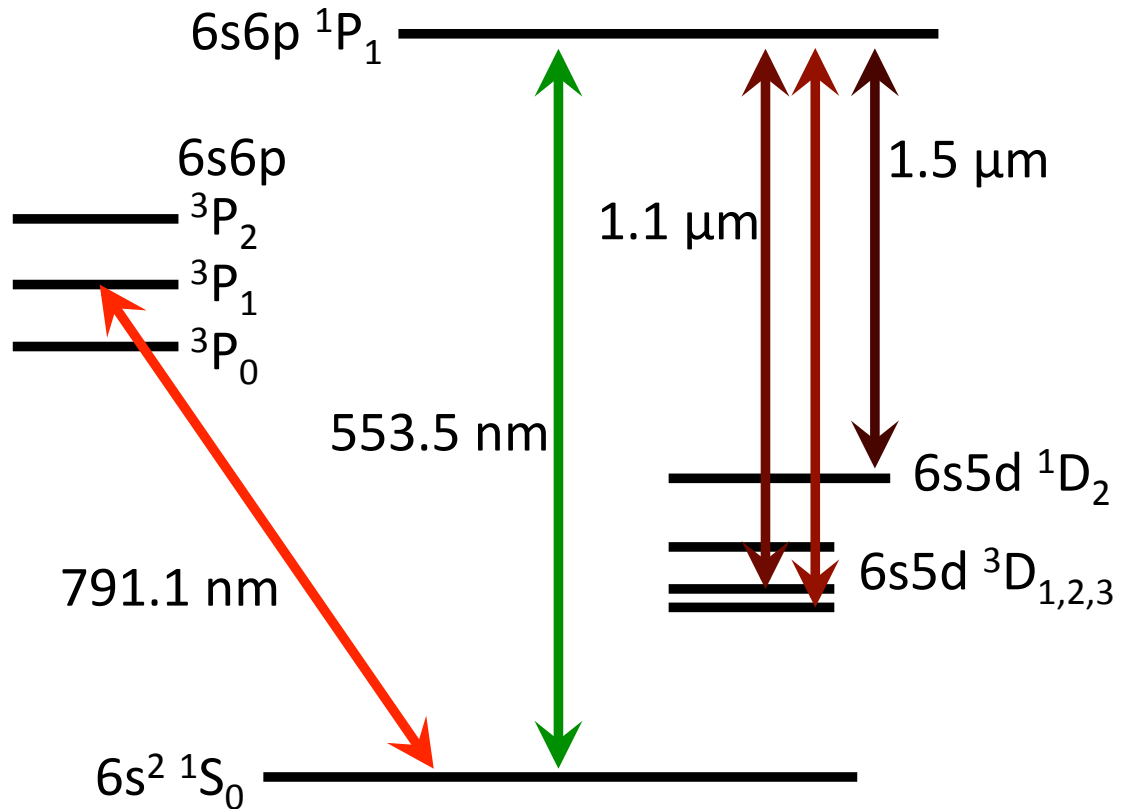


Figure 2.1: Energy levels of neutral barium in vacuum. Excitation from the ground state is primarily achieved at 553 nm. Transitions from the $^3P_{0,1,2}$ states to the $^3D_{1,2,3}$ states are omitted here, as they have wavelengths in the infrared, above 2000 nm.

From the D states in neutral barium, several higher P states exist with excitation wavelengths from 458 to 597 nm. These P states have allowed transitions to the

Table 2.1: Vacuum wavelengths and decay rates for neutral barium transitions [41].

Transition	Vacuum Wavelength (nm)	A (s^{-1})
$6s^2 \ ^1S_0 \leftrightarrow 6s6p \ ^1P_1$	553.5	1.19×10^8
$6s^2 \ ^1S_0 \leftrightarrow 6s6p \ ^3P_1$	791.1	-
$6s6p \ ^1P_1 \leftrightarrow 6s5d \ ^1D_2$	1500.0	2.5×10^5
$6s6p \ ^1P_1 \leftrightarrow 6s5d \ ^3D_2$	1130.3	1.1×10^5
$6s6p \ ^1P_1 \leftrightarrow 6s5d \ ^3D_1$	1107.6	3.1×10^3

Table 2.2: Branching fractions for neutral barium atom transitions.

Transition	Fraction [42]
$6s6p \ ^1P_1 \rightarrow 6s^2 \ ^1S_0$	0.9966
$6s6p \ ^1P_1 \rightarrow 6s5d \ ^1D_2$	0.0025
$6s6p \ ^1P_1 \rightarrow 6s5d \ ^3D_2$	0.0009
$6s6p \ ^1P_1 \rightarrow 6s5d \ ^3D_1$	<0.00008

ground state in the ultra-violet (307nm) [41].

The fraction of the time that an excited barium ion decays into a particular state is called the branching fraction for that transition. The branching fractions for neutral barium are listed in Table 2.2. The neutral barium atom could undergo approximately 300 excitations and decays before the atom is pumped into a metastable state.

In Ba^+ , the main transitions from the ground state to low-lying excited states ($6s \ ^2S_{1/2}$ to $6p \ ^2P_{1/2}$ and $6p \ ^2P_{3/2}$) are at 493 nm and 455 nm, respectively, as shown in Figure 2.2. In addition to decay back to the ground state, these two P states can decay via three paths to two D states, $5d \ ^2D_{5/2}$, and $5d \ ^2D_{3/2}$ at 585 nm, 614 nm, and 650 nm [41]. As with barium neutral atoms, the D states are metastable states, with

Table 2.3: Vacuum wavelengths and decay rates for ionic barium [41].

Transition	Vacuum Wavelength (nm)	A (s ⁻¹)
6p ² P _{1/2} ↔ 6s ² S _{1/2}	493.4077	9.53 × 10 ⁷
6p ² P _{3/2} ↔ 6d ² S _{1/2}	455.4033	1.11 × 10 ⁸
6p ² P _{1/2} ↔ 5d ² D _{3/2}	649.6898	3.10 × 10 ⁷
6p ² P _{3/2} ↔ 5d ² D _{5/2}	614.1713	4.12 × 10 ⁷
6p ² P _{3/2} ↔ 5d ² D _{3/2}	583.3675	6.00 × 10 ⁶
5d ² D _{5/2} ↔ 6s ² S _{1/2}	1762.1745	3.13 × 10 ⁻²
5d ² D _{3/2} ↔ 6s ² S _{1/2}	2051.7652	1.26 × 10 ⁻²

the D → S transitions being parity forbidden in vacuum. The experimental lifetimes of these states are 32 seconds for the 5d ²D_{5/2} state [43], and 79.8 seconds for the 5d ²D_{3/2} state [44]. The decay rates of ionic barium, along with the vacuum wavelengths of the transitions are summarized in Table 2.3.

Branching fractions for Ba⁺ from three papers are presented in Table 2.1. These branching fractions indicate that every fourth excitation from the ground state in vacuum will result in the atom being stuck in a metastable state. Being pumped into a metastable state on every fourth excitation severely limits the practicality of single ion detection in vacuum, as there would be a 32 second period where the ion would emit no photons after every fourth excitation, if no re-pump lasers were used.

Both Ba⁺⁺ and neutral xenon feature full outer electron shells (5p⁶ ¹S₀ ground state). As such, both doubly ionized barium [48] and xenon [49] have ground state to first excited state excitation wavelengths in the vacuum ultraviolet. This makes detection of Ba⁺⁺ in xenon not feasible, as suitable lasers for excitation do not exist. Xenon, being transparent and non-fluorescing in the visible, is ideal for matrix isolation spectroscopy for neutral barium atoms and Ba⁺ ions.

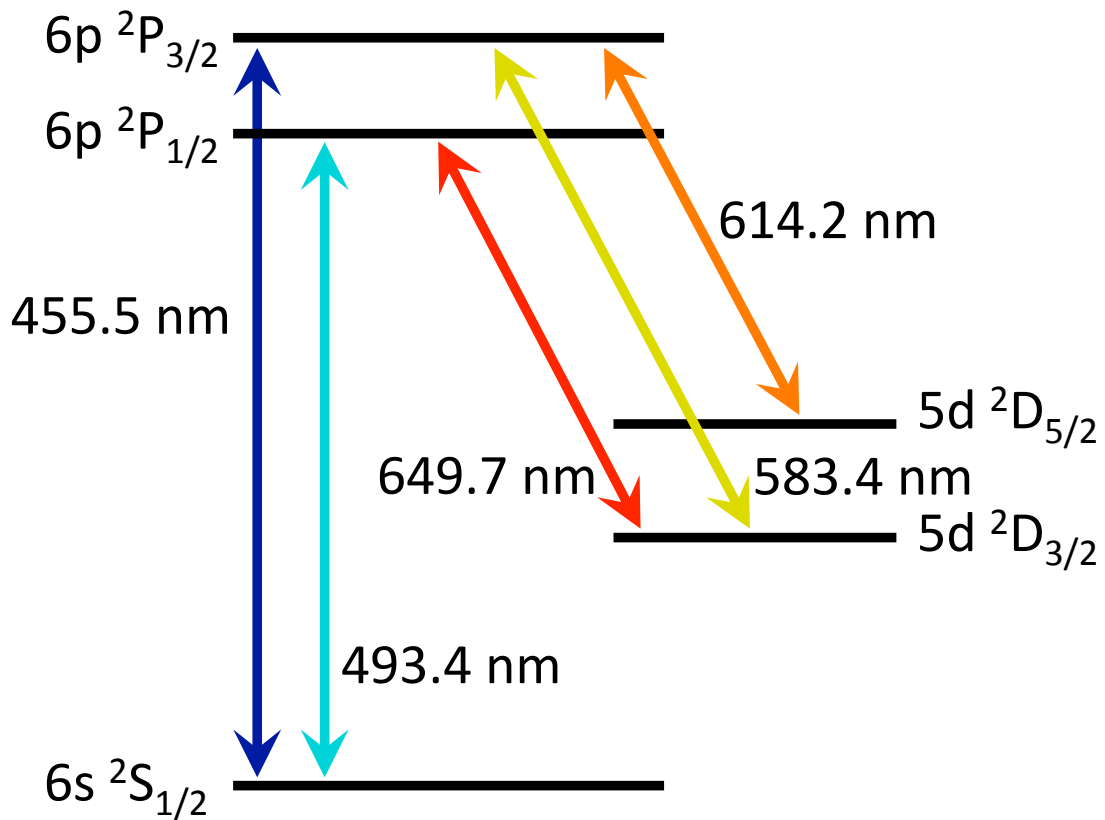


Figure 2.2: Energy levels of barium ions in vacuum. Transitions from the ground state to the first excited states are at 455 nm and 493 nm

2.2 Ba and Ba⁺ Interactions with Noble Gas Atoms

In a matrix, a Ba atom or Ba⁺ ion would be surrounded by six to twelve xenon atom neighbors, depending on whether the Ba⁺ site is interstitial or substitutional. The pairwise interaction of one neutral Ba atom or one Ba⁺ ion with one Xe atom serves as a simplified model to help understand the matrix situation.

In the case of a metal ion and a noble gas atom, the leading term in the interaction energy at large separation distance R is due to the metal ion charge inducing and

Table 2.4: Branching fractions for barium ion transitions.

Transition	Gallagher (1967) [45]	Davidson (1992) [46]	Kurz (2008) [47]
6p $^2P_{1/2} \rightarrow 6s \ ^2S_{1/2}$	0.73	0.756	
6p $^2P_{1/2} \rightarrow 5d \ ^2D_{3/2}$	0.27	0.244	
6p $^2P_{3/2} \rightarrow 6d \ ^2S_{1/2}$	0.74	0.70	0.756
6p $^2P_{3/2} \rightarrow 5d \ ^2D_{5/2}$	0.26	0.26	0.215
6p $^2P_{3/2} \rightarrow 5d \ ^2D_{3/2}$	(included in above)	0.038	0.029

interacting with a dipole moment in the gas atom:

$$V(R) = \frac{\alpha_G \epsilon_{M+}^2}{4\pi \epsilon_0 R_{M-G}^4}$$

where α_G is the polarizability of the noble gas atom, G, ϵ_{M+} is the effective charge of the metal ion, M, and R_{M-G} is the metal ion to gas distance [50]. The leading interaction term for a neutral metal atom and a gas atom is weaker. An approximate expression is

$$V(R) = \frac{I_M I_G}{I_M + I_G} \frac{\alpha_M \alpha_G}{R_{M-G}^6}$$

where α is the polarizability of each atom and I_M and I_G are the ionization potentials of the metal atom and gas ion, respectively, with R_{M-G} being the metal to gas distance [50]. These differences in interaction energies cause differences in fluorescence and excitation spectra between ions and neutrals.

In a diatomic molecule, the emission lines may be red shifted from their vacuum wavelengths, as described by the Frank-Condon Principle, and shown schematically in Figure 2.3. At low temperatures, excitations occur from the lowest vibrational state ($\nu'' = 0$) to various vibrational states of the excited electronic state ($\nu' \geq 0$).

There is then rapid non-radiative decay of the molecule to the lowest vibrational state of the excited electronic state ($\nu' = 0$). The emission then occurs from the lowest vibrational state of the excited electronic state to various vibrational states of the ground electronic state ($\nu'' > 0$). The molecule again undergoes rapid non-radiative decay to the lowest vibrational state of the ground electronic state. This results in a red shift of the emission from the excitation. The total red shift from the excitation is the summed energy of the two non-radiative decays. In Figure 2.3, the $\nu'' = 0 \rightarrow \nu' = 2$ excitation is favored, while the $\nu' = 0 \rightarrow \nu'' = 4$ transition is favored in emission.

Non-radiative transitions from one electronic state to another can occur if potential curves cross [50]. This sort of level crossing occurs in silver atoms in a solid argon matrix [51].

The potential energy curve for the ground state of the $\text{Ba}^+\text{-Xe}$ molecule has been calculated theoretically [52]. Ground state and excited state curves for $\text{Ba}^+\text{-Ar}$ have been determined from spectroscopic measurement [53]. $X^2\Sigma_{1/2}^+$ and $A^2\Pi$ state potential curves were determined experimentally for the Sr^+Ar molecule [54] as well. Panov, in a 1995 paper, predicts the $\text{Ba}^+\text{-Ar } ^2\Sigma^+$ ground state to $^2\Pi_{3/2}(i)$ excited state transitions to exist in the 478 nm to 483 nm range [53], distinctly red-shifted from the $\text{Ba}^+ 6s \ ^2S_{1/2}$ ground state to $6p \ ^2P_{3/2}$ excited state transition in vacuum of 455 nm. Though there is a significant difference in the physics of Ba^+Ar molecules and Ba^+ in solid xenon, it might be expected that a red shift of excitation for Ba^+ in solid xenon from the vacuum value should be expected.

2.3 Matrix Isolation Spectroscopy

The method of matrix isolation, demonstrated first in 1954 by Whittle, Dows, and Pimentel [55], involves imbedding atoms or ions in a solid matrix of an inert

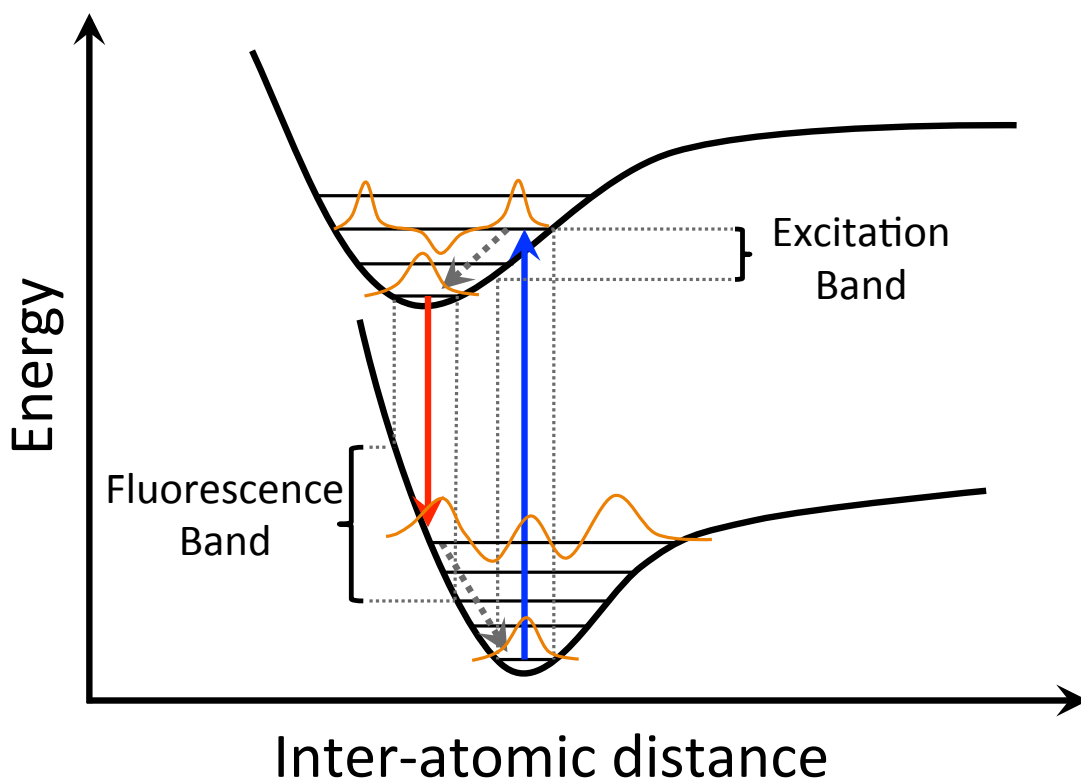


Figure 2.3: Schematic energy diagram of a metal-rare gas diatomic molecule showing a red-shifted fluorescence. Excitation and fluorescence bands are highlighted.

gas, thus allowing rare or metastable atoms, ions or molecules to be studied while immobile, without diffusing. Matrix isolation is a possible aid to barium tagging in a liquid xenon double beta decay experiment, as xenon is an inert noble gas, and barium ions can be frozen in the matrix where they are not mobile. As mentioned in Section 2.1, xenon has a further advantage of being transparent in the visible where barium excitations would exist. With a triple point of 161.4 K [56], xenon requires cryogenic cooling in order to reach solid matrices appropriate for matrix isolation spectroscopy. At equilibrium pressures and temperatures below 75 K, solid xenon forms a close-packed face-centered cubic lattice structure [57].

An early paper on matrix isolation spectroscopy [58] suggests that the ratio of

noble gas atoms to isolated species atoms is of critical importance for successful spectroscopy. This ratio must be high enough to completely isolate the trapped atom or ion, leaving no two ions or atoms neighboring one another. The 1954 paper by Whittle et al. [55] and the 1956 paper by Becker et al. [58] indicate that a gas to sample ratio of 100 to 1 or greater is preferred, as this ratio gives a random probability of 0.08 for two sample atoms or ions in substituted sites to be adjacent to one another. The Becker et al. paper also indicates that xenon, in particular, is not as effective at isolating sample atoms at 66 K, and care must be used with temperatures above this point.

To simulate the single barium tagging of EXO Full where there would be only one barium atom or ion in the whole xenon matrix, the barium ions or atoms in a matrix isolation experiment need to be surrounded by nothing but xenon as much as possible. Though a high gas to sample ratio can prevent isolated atoms or ions from being adjacent to one another, gas purity must also be maximized. Even a modest percentage of impurities in the matrix may increase the likelihood of neutralization of an isolated ion or reaction of the isolated species with an impurity atom. In the case of barium, care must be used to minimize the introduction of air as an impurity, as barium is highly reactive with oxygen and water, resulting in BaO and Ba(OH)₂, respectively, under conditions of standard temperature and pressure. A 1977 paper by Maillard provides evidence that the presence of nitrogen molecules, in a variety of ratios to the argon matrix gas, change the spectra of HCl molecules [59]. Nitrogen, and air in general, must also be minimized in any tagging demonstration experiment in order to accurately represent the ultra-pure xenon environment of the EXO experiment. Similar to the probability mentioned by Becker, a gas impurity ratio of 1 in 100 would give a probability of 0.08 for an impurity to be the neighbor of a sample ion or atom in a substitutional site.

Matrix isolation for barium ions has so far been a little explored field. Reyher

et al. reported that Ba^+ ions in liquid helium have excitation lines at 446 nm and 482 nm. The emission lines from these two excitations were at 493 nm, 525 nm, and 648 nm [60]. In 1968, Kasai reported that some metal ions (cadmium, chromium, manganese, and sodium) could be trapped in argon matrices at 4 K [61]. Furthermore, Kasai reported that migration of the ion is prevented by the matrix at this low temperature. These two facts give optimism that barium ions are able to be trapped and remain ionized in solid xenon, and that the ions, once deposited in the matrix, will be stationary in the observation area. Calcium ions have been isolated in solid argon [62]. The excitation and fluorescence of these calcium ions is 1000 cm^{-1} wide. The fluorescence is shifted from the excitation peak by several thousand cm^{-1} for the calcium ions in solid argon.

2.4 Three Level Model

In some situations, the neutral barium atom and the barium ion may be modeled as a simple three level system. In vacuum the $^2S_{1/2}$, $^2P_{1/2}$, and $^2D_{3/2}$ levels of Ba^+ constitute a closed three level system. In Ba^+Xe , non-radiative decay among fine structure 6p states and among fine structure 5d states may make it possible to group the 6p states together ($|2\rangle$ in Figure 2.4), and the 5d states together ($|3\rangle$ in Figure 2.4). In this simplified three-level interpretation, there are three decay rates, A_{21} , A_{23} , and A_{31} , where A_{21} would be the rate at which an ion decays from state $|2\rangle$ to $|1\rangle$, for example, and one excitation rate, w_{12} from the ground state $|1\rangle$ to state $|2\rangle$, as shown in Figure 2.4. In Ba^+ , this represents excitations from the ground state 6s $^2S_{1/2}$ to either the 6p $^2P_{1/2}$ or 6p $^2P_{3/2}$ state. The populations in states $|1\rangle$, $|2\rangle$, and $|3\rangle$ are denoted by N_1 , N_2 , and N_3 , respectively. The sum of these populations is the total number of ions, N_{total} , which could be set to 1. In this simplified model, the stimulated emission rate w_{21} may be assumed to be zero due to a red shift of

fluorescence wavelength from excitation wavelength, as discussed in Section 2.2, that makes the emission spectrum far out of resonance with the laser.

The neutral barium atom may be similarly simplified to a three state system. The $|1\rangle$ and $|2\rangle$ states are comprised of the $6s^2\ ^1S_0$ ground state and $6s6p\ ^1P_1$ excited state, respectively. The $6s5d\ ^1D_2$, $6s5d\ ^3D_2$, and $6s5d\ ^3D_1$ states can all be combined to form the $|3\rangle$ state.

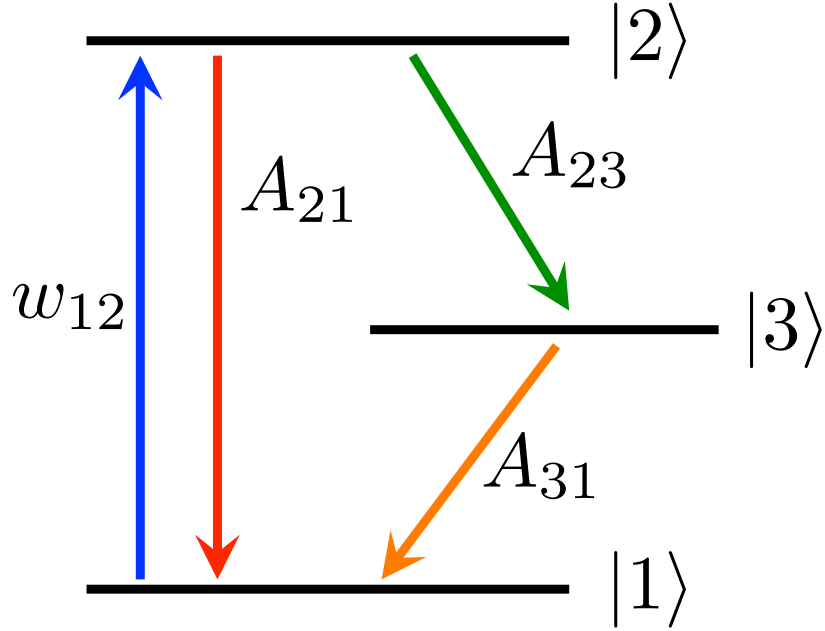


Figure 2.4: Three level model of the barium ion or neutral barium atom.

The rate equations for each of the three states are:

$$\frac{dN_1}{dt} = N_2 A_{21} + N_3 A_{31} - N_1 w_{12} \quad (2.1)$$

$$\frac{dN_2}{dt} = N_1 w_{12} - N_2 A_{21} - N_2 A_{23} \quad (2.2)$$

$$\frac{dN_3}{dt} = N_2 A_{23} - N_3 A_{31} \quad (2.3)$$

Table 2.5: Constants for the time-dependent rate equations.

$$\begin{aligned}
 C_1 &= K_1 R - K_2 / R' & C_2 &= K_1 R + K_2 \\
 C_3 &= K_1 R' - K_2 / R & C_4 &= -K_1 + K_2 / R \\
 K_1 &= \frac{Q_3}{B(\xi_2 - \xi_1)} (A_{31} - \xi_1) & K_2 &= \frac{Q_2}{B(\xi_2 - \xi_1)} (A_{31} - \xi_2) \\
 R' &= (A_{31} - \xi_2) / (A_{31} - \xi_1) & R &= (A_{31} - \xi_2) / A_{23} \\
 Q_3 &= A_{23} w_{12} & Q_2 &= w_{12} A_{31} \\
 B &= A_{31} (A_{21} + A_{23} + w_{12}) + w_{12} A_{23} \\
 \xi_{1,2} &= \frac{A_{21} + A_{23} + w_{12} + A_{31}}{2} \mp \sqrt{\frac{(A_{21} + A_{23} + w_{12} - A_{31})^2}{4} - B}
 \end{aligned}$$

Conservation of total population implies, for N atoms or ions,

$$N = N_1 + N_2 + N_3 = \text{constant}$$

or

$$\frac{dN_1}{dt} + \frac{dN_2}{dt} + \frac{dN_3}{dt} = 0$$

Solutions of these rate equations are of the form [63]:

$$N_2(t) = C_1 e^{-\xi_1 t} + C_2 e^{-\xi_2 t} + \frac{Q_2}{B}$$

$$N_3(t) = C_3 e^{-\xi_1 t} + C_4 e^{-\xi_2 t} + \frac{Q_3}{B}$$

The constants $C_{1,2,3,4}$ and $Q_{2,3}$ are listed in Table 2.5. These have two components. One determines the initial rise-time of N_2/N as atoms are pumped into $|2\rangle$. The other determines the decay of N_2/N as atoms are pumped into state $|3\rangle$.

The time dependence of N_2/N using different w_{12} and A_{31} is represented in Figure 2.5 using A_{21} and A_{23} values of the neutral barium atom in vacuum. Higher values of w_{12} result in a faster decrease in N_2/N . When A_{31} is increased, the steady state value

of N_2/N is raised. The decrease of N_2/N at pumping rates found in experimental conditions, $w_{12} = 1 \times 10^6$ to 1×10^7 , occurs on the hundred-microsecond time scale.

In the steady state, all $\frac{dN_i}{dt}$ are equal to zero. Then the ratios of the state populations to the total population may be calculated:

$$\frac{N_2}{N} = \left[1 + \frac{A_{23}}{A_{31}} + \frac{A_{21} + A_{23}}{w_{12}} \right]^{-1} \quad (2.4)$$

$$\frac{N_3}{N} = \frac{A_{23}}{A_{31}} \left[1 + \frac{A_{23}}{A_{31}} + \frac{A_{21} + A_{23}}{w_{12}} \right]^{-1} \quad (2.5)$$

The buildup in state $|3\rangle$ depends on the two factors A_{23}/A_{31} and $(A_{21} + A_{23})/w_{12}$. The population ratio N_3/N at small w_{12} is approximated as:

$$\frac{N_3}{N} \approx \frac{A_{23}}{A_{21} + A_{23}} \frac{w_{12}}{A_{31}}$$

At large w_{12} , the ratio is:

$$\frac{N_3}{N} \approx \frac{A_{23}}{A_{23} + A_{31}}$$

which is independent of w_{12} .

Several steady state N_2/N ratios (Equation 2.4) for different values of A_{31} are shown in Figure 2.6 for the Ba^+ ion. In solid xenon, the metastable decay rate can be determined by changing the pumping rate w_{12} and comparing the response of the fluorescence, which is effectively a measurement of N_2/N , to this plot.

2.5 Ion Implantation in Solid Noble Gases

In order to study Ba^+ ions in a noble gas matrix like xenon, Ba^+ could be created in the matrix either by mass-selected ion implantation or from in-situ ionization of neutral barium. With the former, the implantation energy must be carefully considered, as neutralization of the ion may occur, and damage of the xenon matrix is an

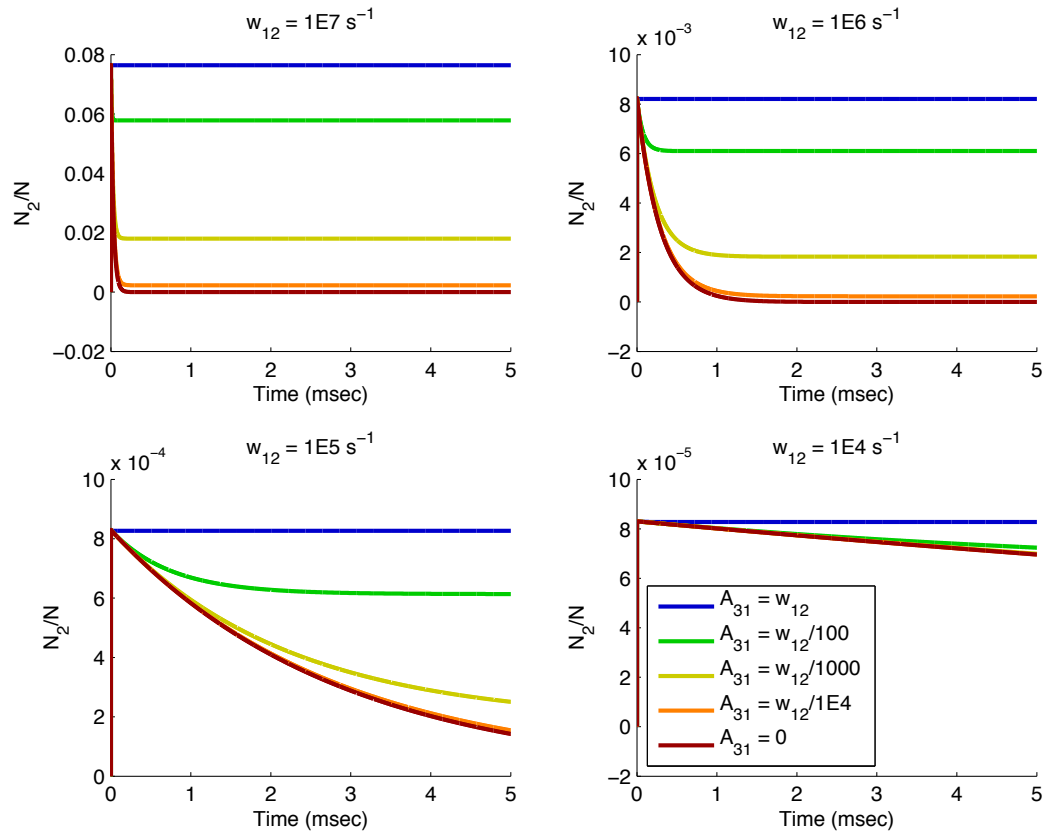


Figure 2.5: The ratio of N_2/N for four different w_{12} excitation rates in neutral barium. Each subplot shows the decrease of N_2/N over time due to five different A_{31} metastable decay rates. Values of A_{23} and A_{21} from Table 2.1.

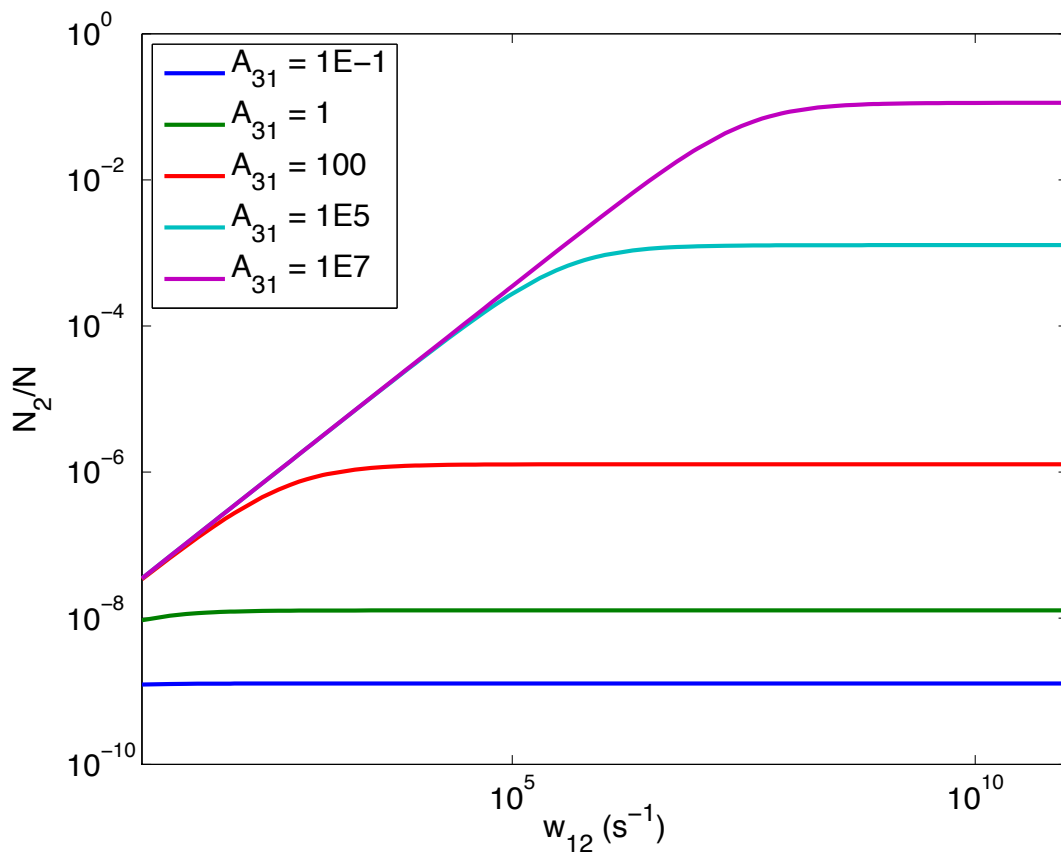


Figure 2.6: Several possible N_2/N ratios versus w_{12} excitation rate for the barium ion for a wide range of different A_{31} values. The A_{21} and A_{23} values of Ba^+ in vacuum are used.

additional concern [64].

In a 1994 paper, A. Kolmakov and V. Stankevich reported the threshold for the ionization of a xenon matrix due to impinging Cs^+ , K^+ , or Li^+ metal ions exceeds 100 eV for all of the alkali metals tested [65]. Molecular dynamics simulations of ions impinging on condensed rare gases have been performed for a variety of energies by Waldeer [66]. For 1 keV argon ions implanted in solid argon, the depth of the damage left by the impact is on the order of 50 angstroms, whereas for a 100 eV beam the deformation is only 10 angstroms deep. These simulations end after only 14 to 40 ps, and therefore do not take into account any healing of the matrix. Though the molec-

ular dynamics simulation did not take into account ionization or electronic excitation, Waldeer estimated that 25% of the landing energy is used for these processes.

2.6 Fluorescence Efficiency

The fluorescence efficiency is the ratio of the total number of fluorescence photons emitted to the number of photons absorbed. It can be calculated as:

$$\epsilon_{fluor} = \frac{F/\epsilon_{det}}{w_{12}N}$$

Here F is the number of counts per second of fluorescence signal, ϵ_{det} is the photon detection efficiency, and N is the number of ions or atoms being detected. Here w_{12} is the excitation rate:

$$w_{12} = \frac{\sigma P}{A h\nu}$$

where σ is the absorption cross section of the atom or ion, $h\nu$ is the energy of the excitation photon, and P and A are the power and area of the laser, respectively.

The fluorescence efficiency may therefore be written as:

$$\epsilon_{fluor} = \frac{Fh\nu A}{\sigma\epsilon_{det}PN}$$

From the shape of an excitation spectrum, it is possible to estimate the absorption cross section. Under the assumption that the integrated absorption cross section of the atom or ion is unchanged in the matrix compared to vacuum the cross section σ is given by

$$\sigma(\nu) = A_{21} \frac{g_2}{g_1} \frac{c^2}{8\pi\nu^2} g(\nu)$$

Here A_{21} is the atomic transition rate and g_2 and g_1 are the degeneracies of the ground

and excited states, respectively. The normalized lineshape function $g(\nu)$ satisfies

$$\int_0^\infty g(\nu) d\nu = 1$$

The cross section equation may then be rewritten as

$$\int_0^\infty \sigma(\nu) \nu^2 d\nu = A_{21} \frac{g_2}{g_1} \frac{c^2}{8\pi} \quad (2.6)$$

The excitation spectrum E_ν is proportional to the excitation rate and to the cross section by the relation:

$$E(\nu) \propto w_{12}(\nu) = \frac{I(\nu)}{h\nu} \sigma_{12}(\nu)$$

This allows the cross section and excitation spectrum to be related via a proportionality constant, C :

$$C \int_0^\infty E(\nu) \nu^2 d\nu = A_{21} \frac{g_2}{g_1} \frac{c^2}{8\pi} \quad (2.7)$$

or

$$\sigma(\nu_0) = \frac{A_{21} E_\nu(\nu_0) \frac{g_2}{g_1} \frac{c^2}{8\pi}}{\int_0^\infty E(\nu) \nu^2 d\nu} \quad (2.8)$$

This equation allows for calculation of the peak cross section using only physical constants and the excitation spectrum shape.

3 Experimental

3.1 Ion Beam

Our method for barium tagging in the EXO-Full experiment requires significant pioneering work to discover processes that happen when Ba^+ ions are trapped in solid xenon (SXe) matrices. Additionally, information about the fraction of barium ions neutralizing in SXe and the temperature dependence of the atomic and ionic fluorescence is also beneficial. Ultimately, it is necessary to increase the sensitivity of the detection to the single atom or ion level. In order to study these things, a method of producing solid xenon and a method of implanting singly and doubly charged barium ions in solid xenon and the optics to properly observe the fluorescence produced are needed

A mass selected ion beam is used to implant barium ions in solid xenon at a variety of landing energies. A complete schematic diagram of the ion beam, along with the corresponding power supplies, is shown in Figures 3.1 and 3.2. This ion beam accelerates, separates by mass, focuses, and deflects ions at high velocities, while still allowing deceleration of the ions to low implantation energies. Figure 3.1 shows the first half of the ion beam, from the ion source and ion source power supplies, the three einzel lenses, first two sets of deflection plates, and the $E \times B$ filter. Figure 3.2 starts at the deceleration section. The deceleration section is followed by deflection plates, the pulsing plates. The rest of the schematic Figure 3.2 shows the detection mechanisms, which are a vane scanner, induction plates, and a Faraday cup, as well as the sapphire sample window. These features will be discussed in the following sections.

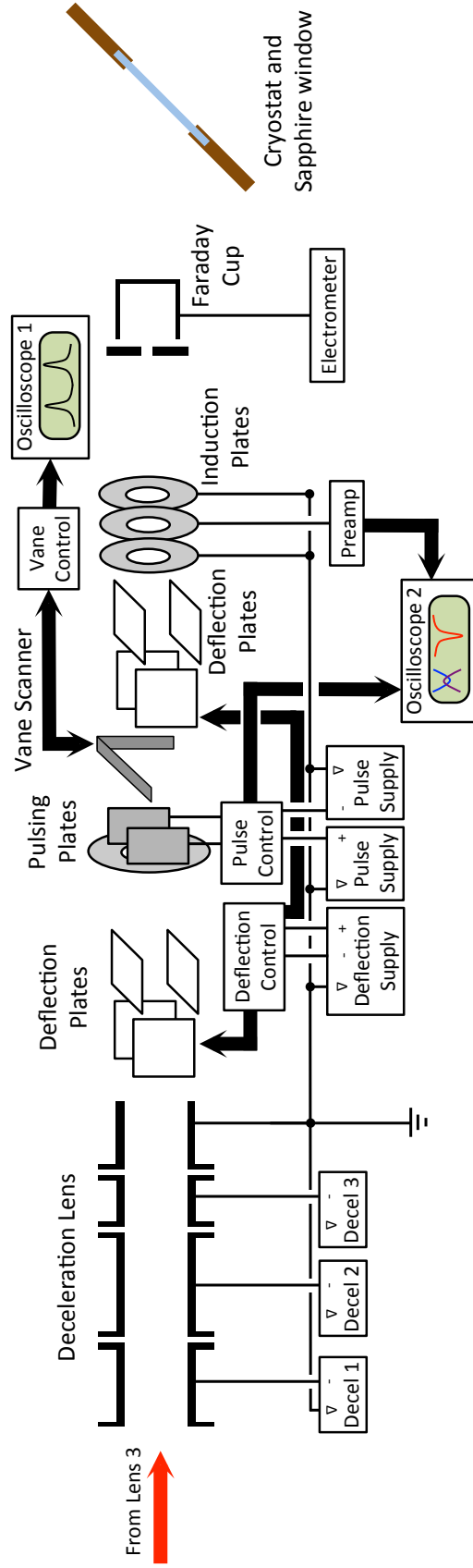


Figure 3.2: A schematic of the second half of the ion beam system, from the deceleration lenses to the cryostat and sapphire window, with corresponding power supplies.

3.1.1 Ion Source

Ions are created using a commercial ion source from the Colutron Research Corporation. The Model 100 ion source can create ions with an energy spread of less than 1 eV [67]. This attribute is critical to good ion beam focussing at low energies and successful mass filtering, and will be discussed in section 3.1.2. This model is capable of providing ions from both solid and gas samples. The ion source can also have 1-10% ionization efficiency [67].

A schematic diagram of the ion source is shown in Figure 3.3. The ion source uses a 0.020 inch diameter tungsten filament inside the boron nitride source cup to vaporize the solid sample. The filament also serves as the cathode for the discharge, which strips electrons from the atoms in the vapor. The anode is a thin sheet of tungsten at the face of the source, attached by a boron nitride cap. It features a 0.5 millimeter diameter hole in the center, through which ions are extracted by an extractor plate at -2000 V potential relative to the anode. Molybdenum leads, which run to vacuum feedthroughs in the ConFlat vacuum mount of the source, serve as the electrical connections for the anode and filament. Typically the filament was operated around 10 V at 14 A, and the discharge at 100 V at 400 mA.

Solid samples are held in place by a stainless steel charge holder that is 1/8" in diameter. The charge holder is able to move in and out of the source by way of a compression O-ring seal, so that the vapor pressure of solid samples in the source may be varied. Through adjustment of the filament current (sample temperature), discharge current, and charge holder position, it was possible to control the ion current coming out of the source. It was found that it was necessary to replace the barium sample after nearly every or every other run of the ion system. Unfortunately, this required roughly a day of down-time, as it would take time to out-gas any water absorbed by the boron-nitride cup when at atmospheric pressure. Because of this,

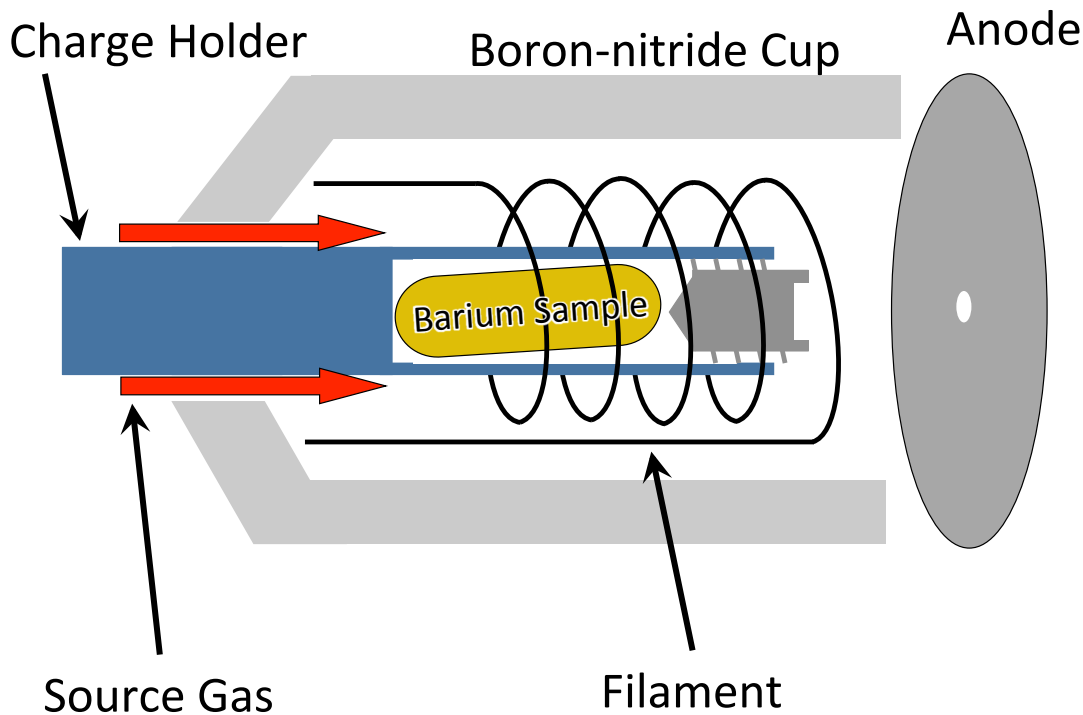


Figure 3.3: Cross sectional schematic diagram of the Colutron ion source.

the system was always back-filled with argon when any maintenance was performed.

Ions from a gas source are created by leaking the desired gas into the source through a leak valve, which is fed by a high-pressure gas bottle, regulated down to roughly 1 psi. Typical source pressures are in the 10^{-3} torr range [67]. By carefully adjusting the leak rate, a gas discharge could be struck, producing ions of the source gas. To isolate the source section from ground, a glass tube was installed (using O-ring compression fittings) between the leak valve and gas bottle regulator. The rest of the connections for the gas inlet system are all Swagelok VCR type fittings, with the exception of the gas inlet, charge holder, and ion source tee. It is possible to run a gas discharge while inserting the solid sample holder, if a discharge of the solid material cannot be initiated on its own. This was never necessary with our Barium

sample, however.

The ion beam is set up such that the final ion deposition energy is set by a beam energy voltage that is applied to the anode. All ion source power supplies float on this voltage. Beam energies can be varied from above 2000 eV to below 100 eV. An isolation transformer was used to power these supplies. This transformer, as well as the one used for the mass filter section, was rated for 1500 VA, and guaranteed to isolate up to 2500 Volts. For safety reasons, the power supplies and ion beam sections that were at high voltages were enclosed in plexiglass. To electrically isolate the source from the rest of the vacuum housing of the beam, a glass vacuum break was used. Mounted to this is the Colutron Heatsink Model 103, which cools the ion source. A stand-alone refrigerator is used to cool both the heatsink and the mass filter, using non-conductive R-134a coolant.

3.1.2 Mass Filter

In order to insure that only the desired ion is deposited on the sample window, a velocity filter (also called a Wein Filter) is used in the beam path. In this case, a Colutron 6" E×B filter, Model 600-B is used. The Model 600-B is a bakeable filter with a maximum electric field of 16,800 V/m and a 3,000 Gauss maximum magnetic field [68].

All ions coming out of the source are accelerated to the same energy, 2000 eV, via the acceleration potential. Since different ion species or isotopes have different masses, they will be accelerated to different velocities. Velocities may be calculated by using conservation of energy:

$$\begin{aligned} \frac{1}{2}mv^2 &= qV \\ v &= \sqrt{\frac{2qV}{m}} \end{aligned} \tag{3.1}$$

where m is the mass of the ion, v is the velocity, q is the charge of the ion, and V is the acceleration voltage. In all of the cases for this experiment, the acceleration potential was kept at 2000 Volts.

The forces on ions of charge q passing through the E×B filter due to fields \vec{E} and \vec{B} are:

$$\vec{F}_E = q\vec{E}$$

$$\vec{F}_B = q\vec{v} \times \vec{B}$$

If these two forces are set to be equal in magnitude but opposite in direction, \vec{v} , which is perpendicular to both \vec{E} and \vec{B} , is the velocity of ions which will be passed undeflected through the E×B filter [69].

$$v = \left| \frac{E}{B} \right| \tag{3.2}$$

By substituting (3.1) into (3.2) and solving for $\frac{m}{q}$:

$$\frac{m}{q} = 2V \left(\frac{B}{E} \right)^2 \tag{3.3}$$

For parallel plates, $E = -\Delta V/d$, where d is the known distance between the two electrodes. Thus E can be found from the measured potential difference, ΔV . The relationship between the strength of the B-field and the current I applied to the electromagnet is also known [68], so that a measurement of I determines B . Then the m/q ratio being selected is found by substituting ΔV and the I with appropriate proportionality constants into Equation 3.3.

Because the E-field plates of the E×B filter can cause astigmatism of the ion beam, E-field guard rings are added to the filter to control the fringing fields [70]. Controls allow for adjustment of the potential of each symmetrical set of shims individually. To monitor the shape of the beam, a vane scanner is used down-stream of the velocity

filter. The vanes sweep through the beam, giving an X and Y profile. Samples profiles for a variety of beam energies are shown in Figure 3.4. By watching this profile on an oscilloscope, the guard rings may be tuned to remove almost all astigmatism. In addition to adjusting individual sets of E-field shims, the Colutron mass filter also allows for biasing of the E-field, from one side to the other. In all of these experiments the E-field was kept balanced between left and right. Power supplies for the E-field and B-field float at 2000 V below the source voltage V_S .

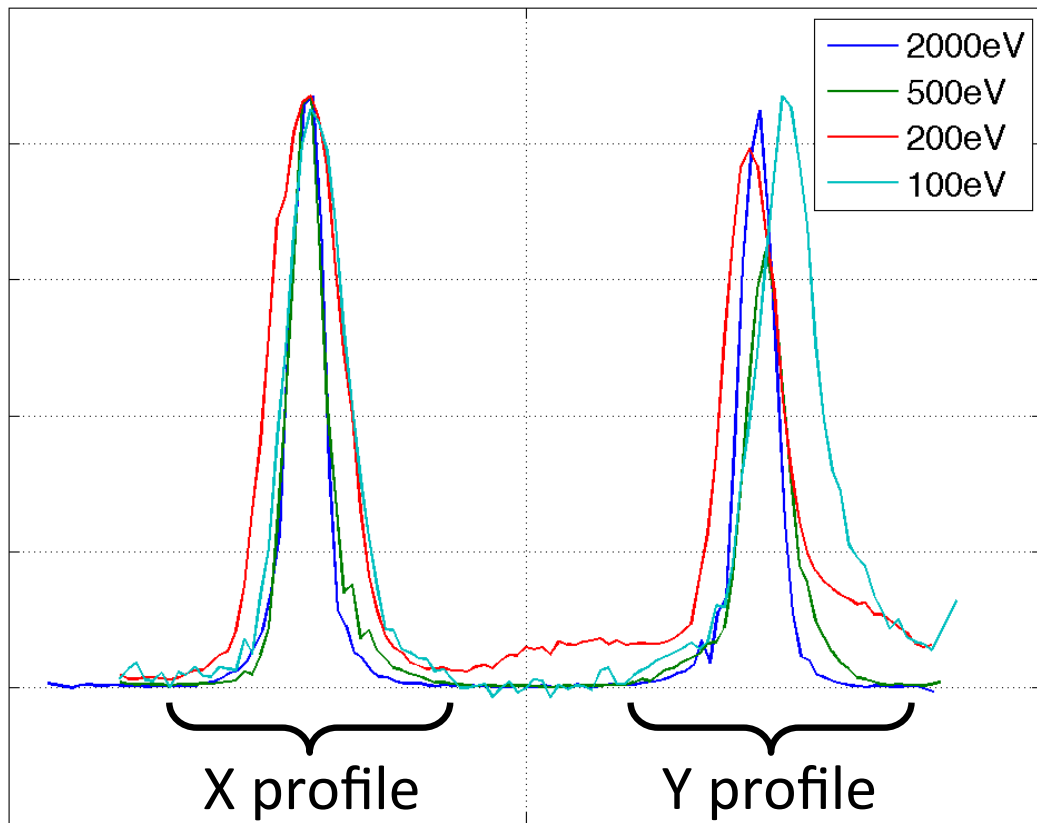


Figure 3.4: Plot of vane scanner profile. Each peak is a profile of the X or Y axis of the ion beam. Peak heights are scaled to be similar in this figure.

Though Colutron quotes a mass resolution of $\frac{M}{\Delta M} = 400$ [68], this could never be verified by the CSU ion beam setup. Figure 3.5 shows a mass scan of a beam of 2000 eV Ba^+ with a mass resolution of 18.

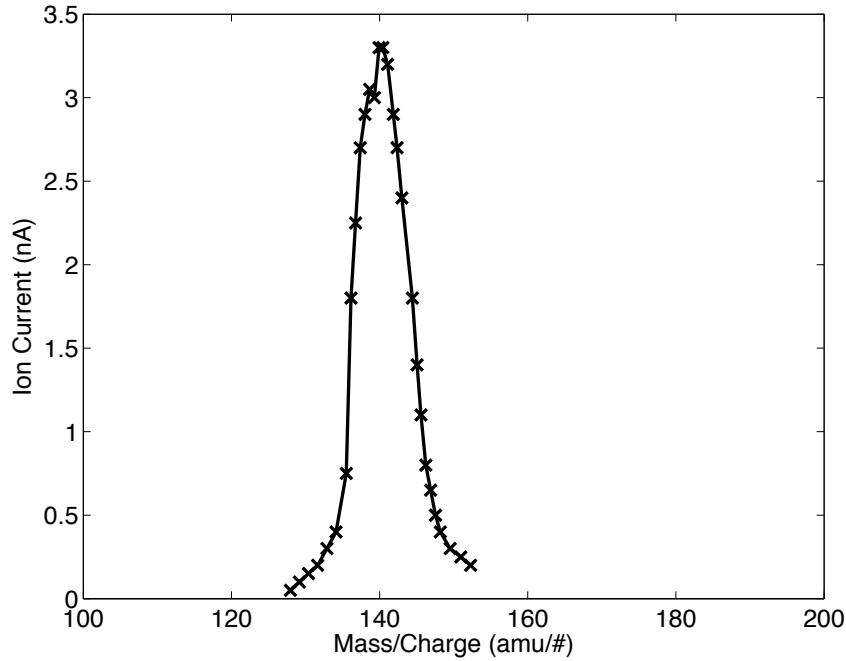


Figure 3.5: Plot of ion current versus mass for a 2000 eV beam of Ba^+ , with a mass resolution $\frac{M}{\Delta M} \approx 18$.

3.1.3 Ion Focusing and Deflection

Focusing of the ion beam is done by three einzel lenses along the beam. The einzel lenses are each composed of three cylindrical tubes of stainless steel. The first and third tubes are set at a fixed voltage ($V_S - 2000$ V), while the middle section voltage is adjustable. By adjusting the voltage of the middle section, the electric field formed in the spaces between each tube is varied. This provides the focusing action of the lens [71].

The first einzel lens is located immediately after the ion source. The first einzel lens is located in a section of vacuum housing that holds the vacuum pump. To avoid floating the entire high-vacuum pump and fore-pump, this section of vacuum housing was kept at ground. This necessitated the einzel lens be insulated from the housing.

This was accomplished by using Mullite insulating tubes between the lens parts and the supporting rods. To prevent the grounded vacuum manifold from interfering with the electric fields of the lens, a stainless steel tube, kept at $V_S - 2000$ V, surrounds the lens. The grounded section of vacuum housing is electrically isolated from the at-potential vacuum housings by a Lexan flange.

Initially, the first einzel lens had a 1-2 mm diameter aperture just before the lens entrance. During a visit from Colutron founder Dr. Lars Wåhlin, it was recommended this aperture be removed, and the original 9.5 mm diameter entrance hole restored, as there was visible pitting on the aperture, evidence that it was blocking a significant amount of ion current. This improved ion beam current, though it increased angular spread of the beam [72].

The second and third lenses are located just after the $E \times B$ filter and just before the deceleration section, respectively, as seen on the right side of Figure 3.1. When the ion beam was moved to a platform-on-rail system, it was necessary to remove the 10° bend and corresponding electronics that had been previously installed [72]. The lack of bend placed the second lens out of the beam path. To relocate the lens, the ConFlat flange on which the lens was mounted was tapped to put the lens in the straight beam path.

Each einzel lens was powered by a modular power supply from Bertan. The output of the power supplies is 0 to -5 kV, with a specified AC ripple of less than 50 mV [73]. Measured AC ripple was ≤ 5 mV. Each lens is biased by a power supply, and each power supply output voltage is controlled individually.

In order to direct the ions, sets of horizontal and vertical deflection plates are used throughout the beam, as shown in Figures 3.1 and 3.2. Plates are constructed of stainless steel, attached to support structures via a mix of vacuum appropriate insulating material such as Macor.

The first two pairs of deflection plates are positioned between

the first einzel lens and the E×B filter. These are used to make the ion path parallel to and on the axis of the filter. The third pair is positioned directly before the third einzel lens, and keeps the beam on axis when it enters the deceleration region. The first, second and third pairs of deflection plates are in the floating region of ion beam, and receive voltage from power supplies floated at $V_S - 2000$ V.

The the fourth pair of deflection plates lie before the vane scanner and pulsing plates. The fifth pair lies just after the vane scanner and pulsing plates, just before the Faraday cup used for ion current measurement at the output of the ion beam. The pulsing plates and corresponding electronics are discussed in further detail in Section 3.1.5.

Using a laser, the ion optics were carefully aligned to be parallel through the entire length of the apparatus, from the source to the sample window. Though the deflection plates were operated at zero deflection, it was never verified that the ion beam was perfectly on axis with the ion optics.

3.1.4 Deceleration

The source, acceleration, and deceleration section potentials are shown schematically in Figure 3.6. Ions produced in the ion source are extracted by an acceleration potential of -2000 V below the ion source potential (V_S). From the acceleration region, the ions enter a deceleration section at ground potential, which slows down positively charged ions. In this manner, ions undergo focusing and mass filtering at 2000 eV, and then are landed on the sample at the ion source potential with energy $E_{\text{landing}} = qV_S$.

As the ions are decelerated, the phase space of the beam increases [74]. This results in an increase in the product of the beam radius and angular divergence at a focus. Deceleration and refocusing are provided by four tubes in the deceleration section. The potentials of the first three tubes can be adjusted, while the fourth is

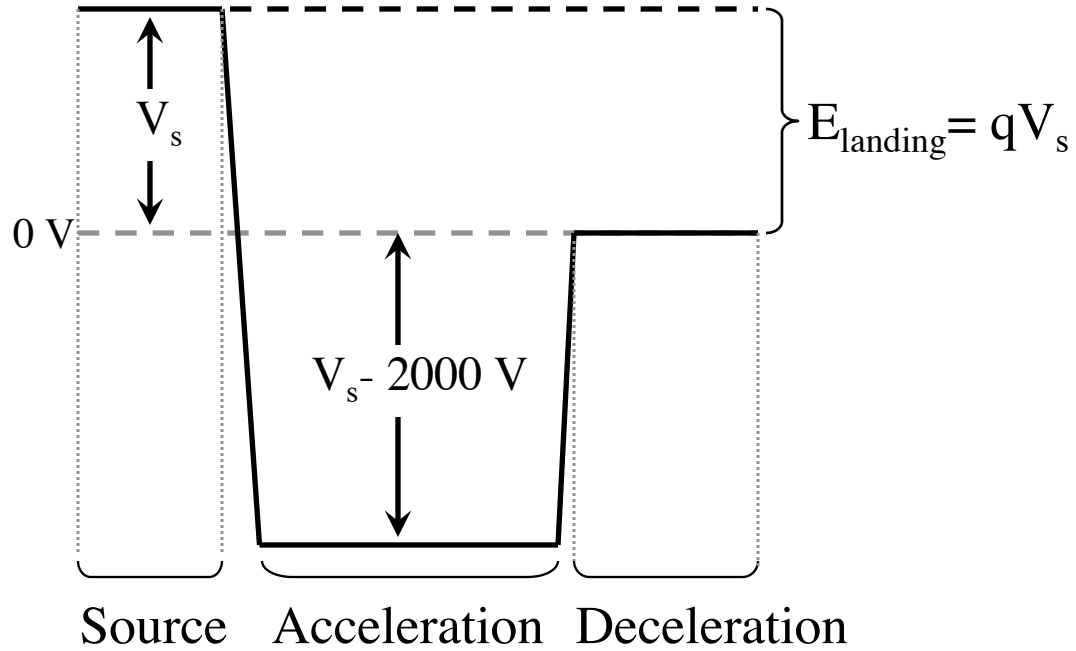


Figure 3.6: A schematic diagram of the ion beam energies. The initial ion source potential V_s determines the final landing energy E_{landing} of the ions. Ions are accelerated from the source by a -2000 V potential

fixed at ground potential. With optimal adjustment of the voltages on the tubes, the decelerator section produces a nearly parallel beam on the output.

Since the decelerator section housing is at ground potential, no electrical isolation is needed when connecting to other system parts, such as the cryostat vacuum housing. A double-sided Lexan flange, identical to that between the grounded vacuum pump section and the rest of the acceleration section, is used to isolate this section from the acceleration section.

3.1.5 Ion Pulsing and Detection

In order to finely control the number of ions deposited, along with having the ions be on-demand, a system for quickly sweeping the ions from a deflected path to on-target was developed. This system is comprised of a set of deflection plates, a

positive and negative power supply set, a pulsing circuit, and a trigger system. A circuit diagram of the pulsing unit is shown in Figure 3.7.

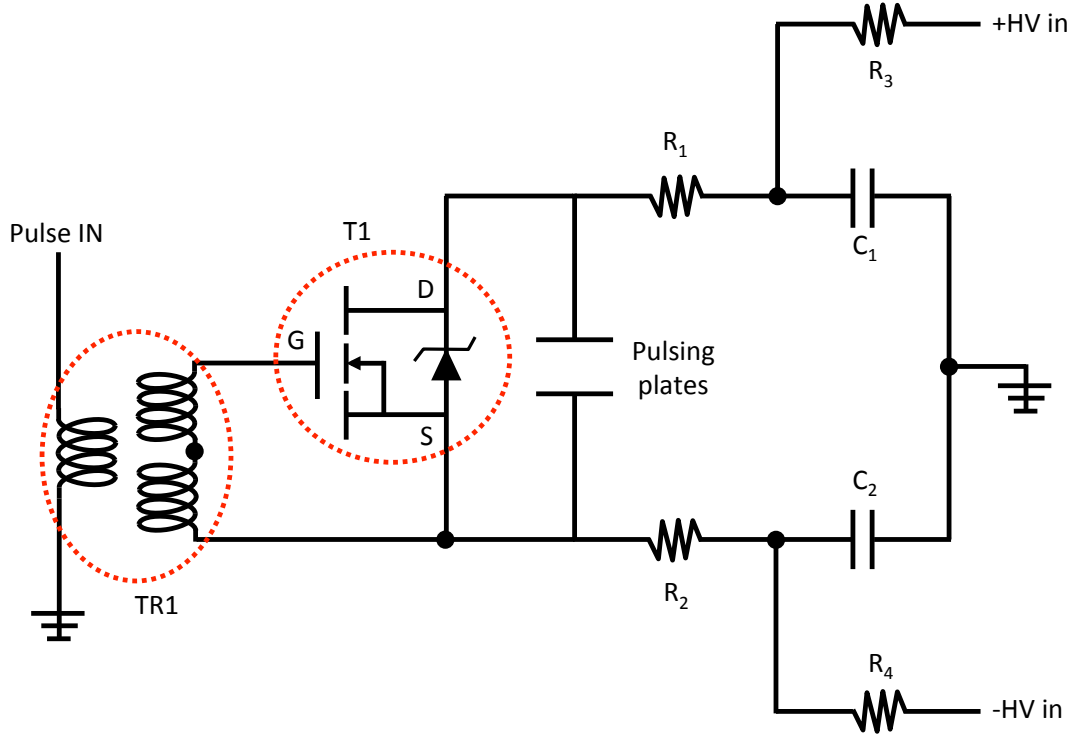


Figure 3.7: Circuit diagram of the pulsing circuit. \pm HV inputs are ± 200 V power supplies. R_1 and $R_2 = 470 \Omega$, R_3 and $R_4 = 20 \text{ k}\Omega$, and C_1 and $C_2 = 680 \text{ nF}$. $TR1$ is a pulse transformer, and $T1$ is a power MOSFET.

The pulsing plates were designed to allow the slowest ion used in the experiments, Ba^+ at 100 eV, through with a pulse length of $1 \mu\text{s}$. Using these parameters the deflection plates were designed with 1.27 cm spacing and plate lengths of 1.1 cm. The plates are set to ± 200 Volts to deflect the beam. Both plates are set at ground potential in undeflected mode. The pulsing plates are mounted to a plate via Macor, and sit in the beam line in the middle of the third set of deflection plates.

The circuit required a $1 \mu\text{s}$ trigger pulse width. The Labview control box was not able to produce pulses at that width, so a microsecond pulse generator was used as

the trigger for the pulsing plates. To allow for computer control of ion pulses, the microsecond pulse generator was triggered by the Labview control box. Voltages for the pulsing plates were provided by Bertan power supplies.

The ion pulses were detected in two ways: through the Faraday cup, and through an induction plate system. To detect small, fast pulses, the cup was attached to a $0.2 \text{ mV}/fC$ preamp, with the output fed to an oscilloscope. With the cup in the beam path, ion current pulse measurement and ion deposition at the same time was not possible. Thus, an in-situ measurement device using induction signals was developed and built.

According to Ramo's Theorem, current is induced in a conductor by moving ions or electrons. The induced current I is given by the equation

$$I = E_v q v$$

where q is the charge, v is the velocity, and E_v is the field at the charge position when unit potential is applied to the detection electrode with the others at ground potential [75].

The induced current detector is comprised of a series of three stainless steel discs, each with a 0.5" hole through which the ions pass. The discs are held together by three bolts. The center detector disc is held in place with ceramic beads, so as to electrically isolate it. The outer two plates shield the middle one from any induced current until the ions are near the detector. The induction detector was designed to insure that there would be adequate current induced for typical values of ion velocity and ion current. The plates are spaced 0.25" apart, and the total plate diameter is 1.25". This diameter is nearly that of a standard 2.75" ConFlat nipple's inner diameter of 1.37". To hold the detector in place, three thin stainless steel fingers on the first and last plate press against the side of the nipple. These also serve to ground

the plates.

The induced current from the detector plate is amplified by a $1.0 \text{ mV}/fC$ preamp, with output to the same oscilloscope as the Faraday cup. Figure 3.8 shows a typical signal of the two pulsing plate voltages, along with the two preamp signals for the Faraday cup and the induction plate detector. Because the induction plates are in front of the Faraday cup, the plate signal is seen just before the cup signal. The voltages of the pulsing plates are also monitored on the oscilloscope. The difference in time from the pulsing plates both going to ground potential to the arrival of ions on the Faraday cup gives a time of flight of the ions. The distance from the pulsing plates to the Faraday cup divided by this time of flight gives an ion velocity. This velocity was compared and agreed with the velocity allowed to pass undeflected through the $E \times B$ filter for confirmation.

Figure 3.9 shows the converted preamp signals. Conversion from the preamp signal voltage V_{out} to current is given by:

$$I = - \left(V_{out} + R_1 C \frac{dV_{out}}{dt} \right) / R_1 M$$

where $R_1 C$ and $R_1 M$ are constants determined for each preamplifier.

Unfortunately, because the length of the group of ions passed by the pulsing plates is longer than the set of induction plates, some overlap is seen between the cup signal and the plate signal in Figure 3.9. This occurs because some part of the pulse produces induction current while passing through the induction detector while the front of the pulse is arriving at the Faraday cup. Additionally, the induction may extend beyond the 3rd plate because of the hole through which ions pass. Both factors explain the overlap of signal. The induction plate signal shows both an arrival and departure of ions, denoted by first positive, then negative signal. The Faraday cup signal, however, only shows an arrival of ions.

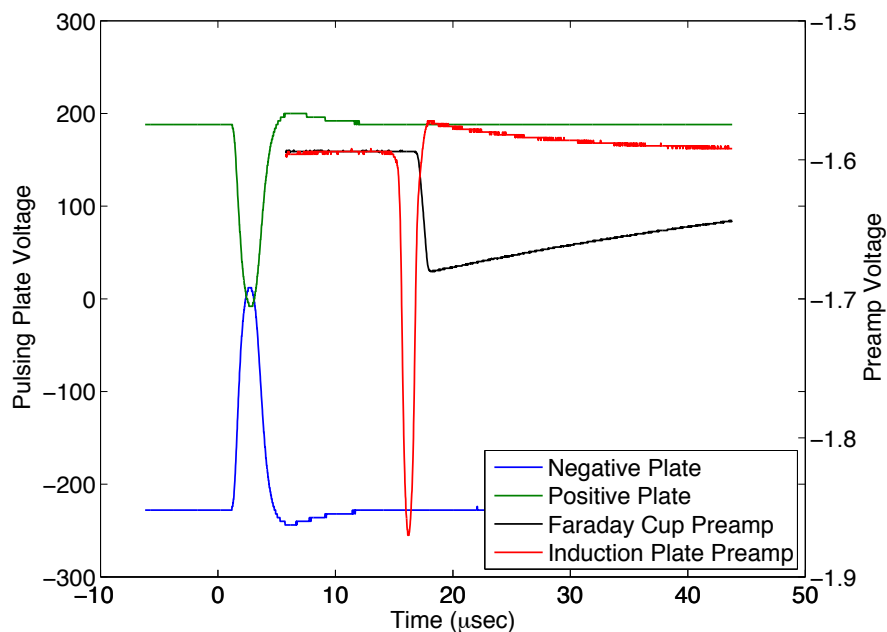


Figure 3.8: Plot of pulsing plate voltages and the corresponding preamp signals for the Faraday cup and the induction plates. This signal is from 2×10^6 Ba^+ ions at 2000 eV.

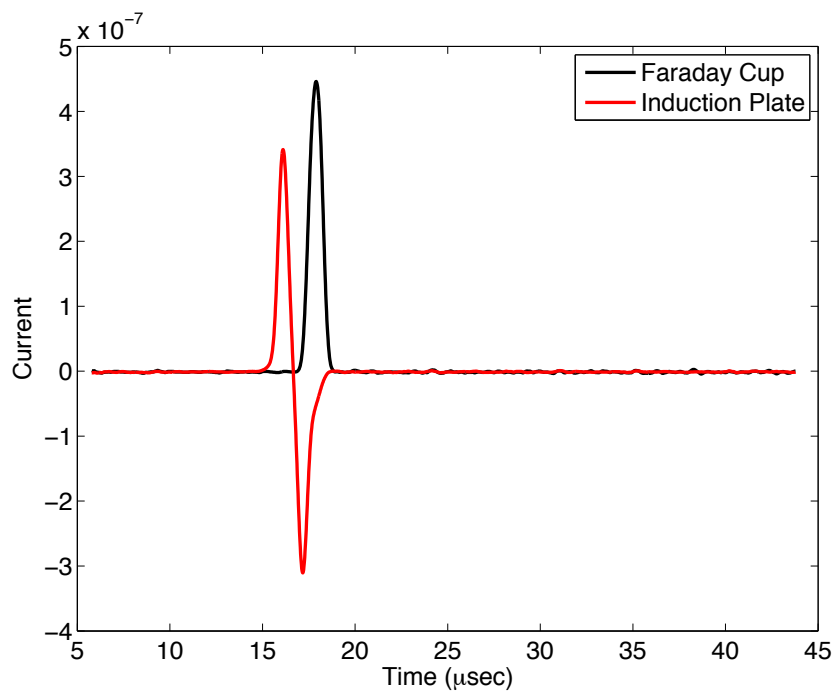


Figure 3.9: Faraday cup and induction plate preamp signals, converted to current versus time.

3.1.6 Ion Beam Vacuum Generation

Initially, vacuum for the ion beam was generated by two 4" inlet diameter diffusion pumps, each backed by a roughing pump. In order to prevent diffusion pump oil from back-streaming into the system and contaminating any spectra, each diffusion pump was used with cooled baffles. The baffles near the source were water cooled, while the baffles on the pump on the decelerator section were liquid nitrogen cooled. There was a gate valve between each baffle and the ion beam. In order to improve system purity, the diffusion pumps have been replaced by two identical 8" turbomolecular pumps, each backed by a scroll pump.

Pressures were monitored by an ion gauge, located near the end of the ion beam system, just before the cryostat vacuum chamber. System pressures for the ion beam during experiments were usually in the 1×10^{-7} Torr range, with pressures dipping into the 7×10^{-8} range. When the source was run on a gas discharge, the system pressure was somewhat higher.

To ensure a clean system, parts designed for ultra high vacuum were used. Vacuum appropriate wire and insulating material was always chosen over other options, and vacuum grease was used on Viton gaskets. Wherever possible, ConFlat fittings with copper gaskets were used. Viton gaskets were necessary at particular locations, such as at the Lexan electrical breaks, the solid charge holder, and at the glass electrical break on the ion source gas inlet.

3.1.7 Neutral Barium Deposition

In order to confirm that fluorescent peaks observed when ions were deposited were due to Ba^+ and not neutral barium, separate depositions of only neutral Ba atoms was necessary. This was achieved by running current through a SAES getter. As the getter is heated, neutral barium is emitted in all directions from the face of the

getter. The barium getter sits inside a stainless housing that could be inserted and retracted, capable of depositing neutrals on the same path as the ion beam. Currents through the getter were in the 10 to 14 amp range, and the getter was replaced after every or every other use.

3.2 Cryostat

3.2.1 Cryogenic System

In order to achieve the low temperatures necessary for formation of solid Xenon, a helium cryostat is used. The cryostat used for these experiments is an Advanced Research Systems model DE-202. This model is a small, closed-cycle helium cryostat, capable of temperatures as low as 10 K, at which temperature the experiments were performed. The cryostat cold head has a copper cold finger, to which a copper window chuck was attached. Between any copper contact points, flexible Indium foil or wire was used for efficient heat transfer.

A Viton gasket-sealed vacuum shroud surrounds the cold finger. It has five ports on all sides of the finger that provide optical access through a window in three directions, ion beam access, and gas access via a custom gas inlet. A cut-away schematic drawing of the sample region is shown in Figure 3.10. The windows through which the lasers pass have an anti-reflective coating to minimize scatter. Immediately inside of the vacuum shroud, but surrounding the cold finger, is a radiation shield, cooled by the first stage of the cryostat, which is at approximately 77 K. This shield insulates the cold finger from room temperature radiation from the vacuum shroud and the outside environment. Several holes allow ions, light, and gas to pass through this radiation shield.

Solid gas matrices and ions are deposited on a sapphire window, held in place by the copper chuck, which is attached to the cold finger. Indium film is used between

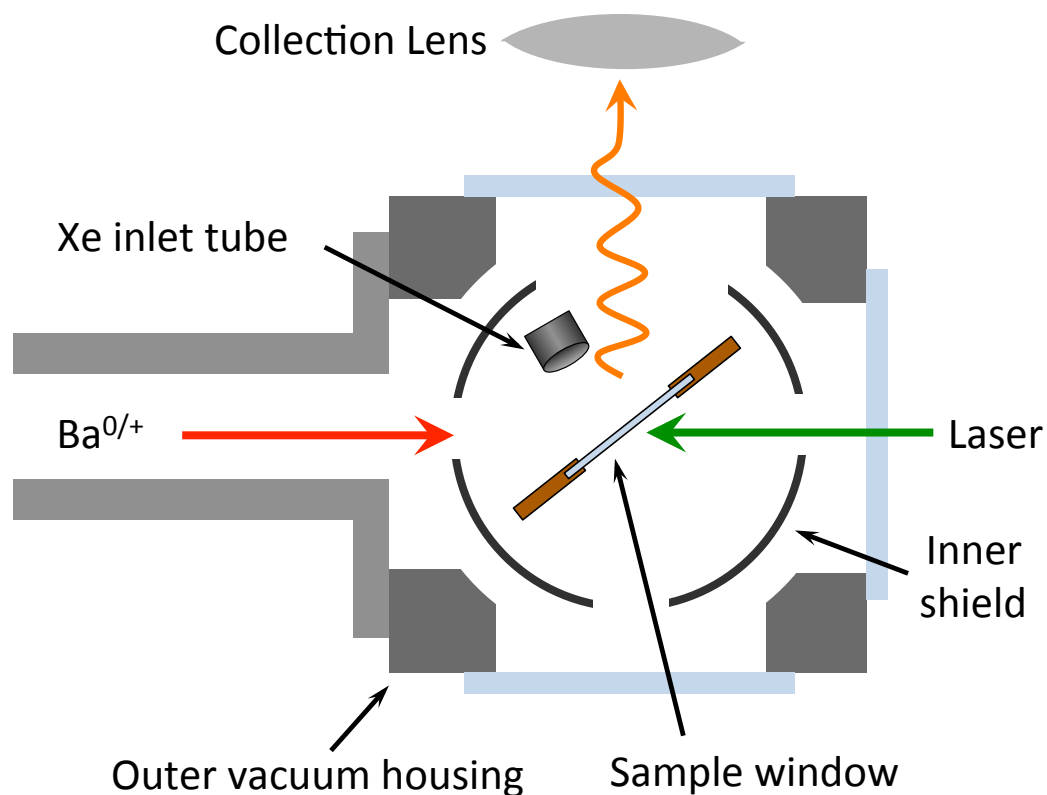


Figure 3.10: Cut-away schematic of the sample region of the cryostat. The red arrow indicates the paths of the Ba^{+} ion beam or neutral barium from the getter. The green and orange arrows represent the paths of the laser and the fluorescence, respectively.

the window and the copper chuck to maximize heat transfer. The window is held at a 45° angle relative to the ion beam path, so as to allow both deposition of ions and optical access.

A heater, with settings ranging from 0.1 W to 15 W, is attached to the cold finger. With a set-point adjustment on the cryostat controller, the cryostat can be set at and held at any desired temperature. Heating from 10 K to xenon sample sublimation temperatures above 75 K took approximately 15 minutes at the 15 W heater setting. Re-cooling took another 15 to 30 minutes.

In addition to the thermocouple, a Lakeshore brand calibrated silicon diode, connected to a corresponding controller, also monitors the cold finger temperature. The

two measurements nearly always read within 1 K of one another.

3.2.2 Gas Deposition

Gas used for the creation of the solid gas sample comes from high-pressure bottles of ultra-pure gas, regulated to approximately 20 psi. Though argon gas was initially used for preliminary runs, xenon was used in the bulk of this work. A leak valve separates the 20 psi gas from the high-vacuum section of the cryostat. By adjusting the rate of the leak, the deposition rate of the solid matrix can be adjusted. The low-pressure gas enters the cryostat housing through a special feedthrough mentioned previously. A hole in the radiation shield allows for a $1/8$ " OD stainless steel tube to pass through without touching the shield. This tube sprays the low pressure gas on the cold window used as a substrate for the matrix. All connections of tubing for the cryostat gas deposit system were made using Swagelok VCR fittings.

By monitoring the reflection of a 532 nm laser focused on the xenon sample, the matrix growth rate was found by measuring the period of the interference fringes caused by growth of the matrix. A plot of the matrix growth rate for leak valve settings is, shown in Figure 3.11. A power law curve with an offset was fit to the data. The offset represents what would be the growth rate of a matrix comprised of only residual gases. This residual gas growth rate was found to be $\approx 7.5 \times 10^{-2}$ nm/s. Figure 3.12 shows the interference fringes for leak valve settings of 46, 48, and 50, and the corresponding sinusoidal fits. The leak valve settings of 46, 48, and 50 corresponded to matrix growth rates of 3.8 nm/s, 15.7 nm/s and 44 nm/s, respectively. Comparing the calculated growth rate of the residual gas matrix to the observed growth rate for leak valve settings used during experiments gives an estimated purity of the solid xenon sample. For a leak valve setting of 46, which was used in most experiments, an impurity level of 2% was calculated. A leak valve setting of 55 was used for some small number detection experiments. This leak valve

setting resulted in an impurity level of 7.5×10^{-5} .

At some point in the course of the experiments, the xenon matrix growth rates resulting from the leak valve settings changed. All growth rate experiments and impurity calculations, as well as the small number neutral atom detection presented in this thesis, were performed after this change. It is unknown when or why this change in the leak valve occurred.

A Stanford Research Systems Residual Gas Analyzer (RGA) was purchased and installed in the short section of tubing between the cryostat and the ion beam. The purity of the deposited gas can be estimated from the measured partial pressures of xenon and residual gases in the RGA spectrum. RGA spectra were taken at modest leak rates before experiments, and, when possible, were monitored during experiments.

The partial pressures of xenon and impurity gases at different leak valve settings were monitored during experiments. Since the xenon partial pressure at the RGA is greatly reduced when the window is cold due to condensation, these measurements were done with the cold finger and window at room temperature. However, in order to not saturate the RGA, this method cannot be used at the high xenon leak rate. Figure 3.13 shows the partial pressures of the three largest xenon isotopes and several other trace gasses versus the total xenon partial pressure as the leak valve was slowly opened. As expected, the xenon isotopes respond linearly with the total xenon partial pressure. Below total xenon pressures of 10^{-7} Torr, all of the other trace gas partial pressures except krypton are constant. According to specifications, krypton is the largest impurity in the xenon gas. Overall, however, Figure 3.13 shows that the xenon source gas is quite pure, and that the impurities in the matrix are primarily due to residual gases.

At xenon pressures above 10^{-7} , all trace gases except krypton increase slightly with increased xenon pressure. This may be due to the xenon pushing more of the

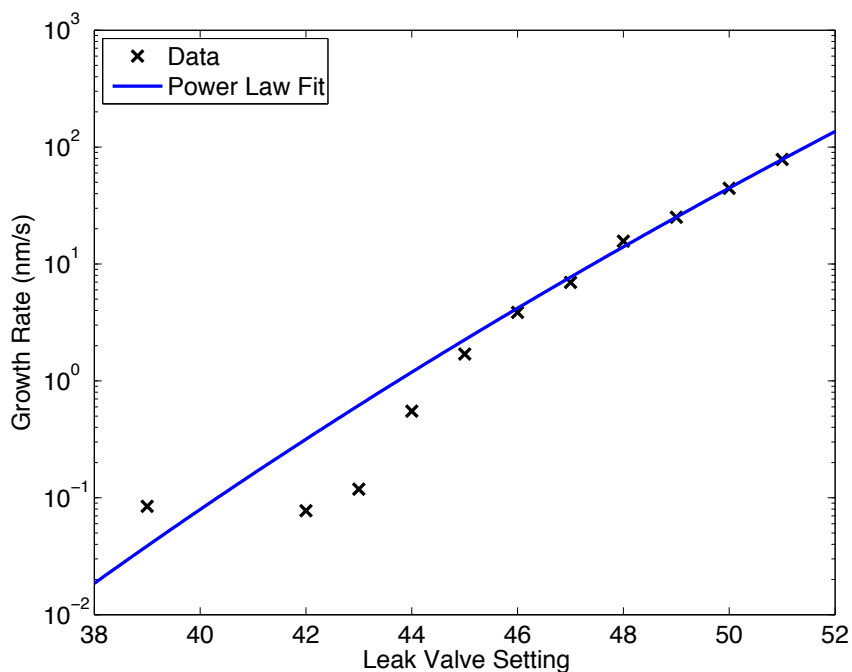


Figure 3.11: Matrix growth rate versus leak valve setting, with the corresponding power law fit.

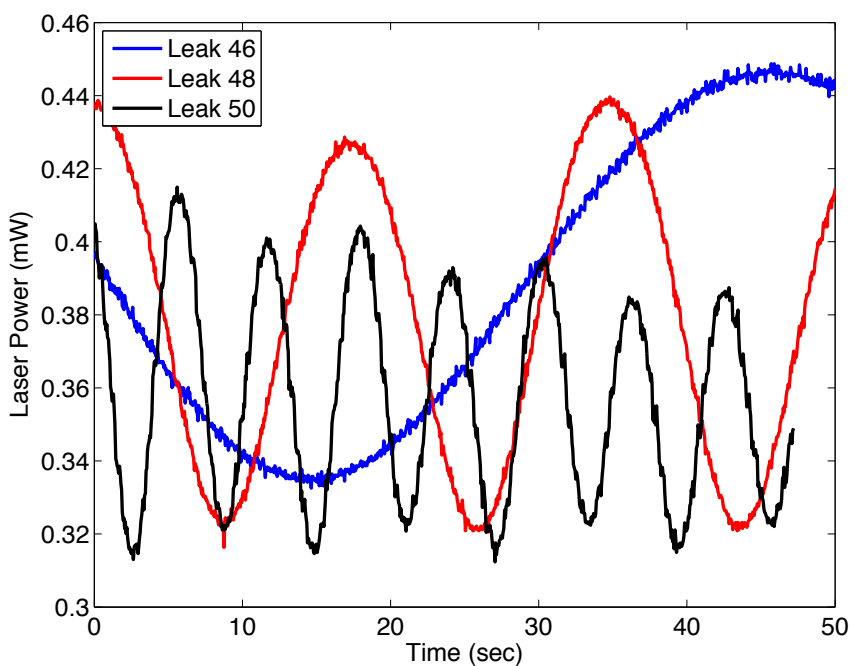


Figure 3.12: Interference fringes due to xenon frozen on the sapphire sample window for leak valve settings of 46, 48, and 50.

residual gases towards the RGA from the cryostat region. If the rise were due to impurities in the xenon gas, the curves would have not rise in unison. At the absolute highest xenon pressures, all trace gasses curves dip downward, which is an anomalous effect caused by saturation of the RGA, and is not a real effect.

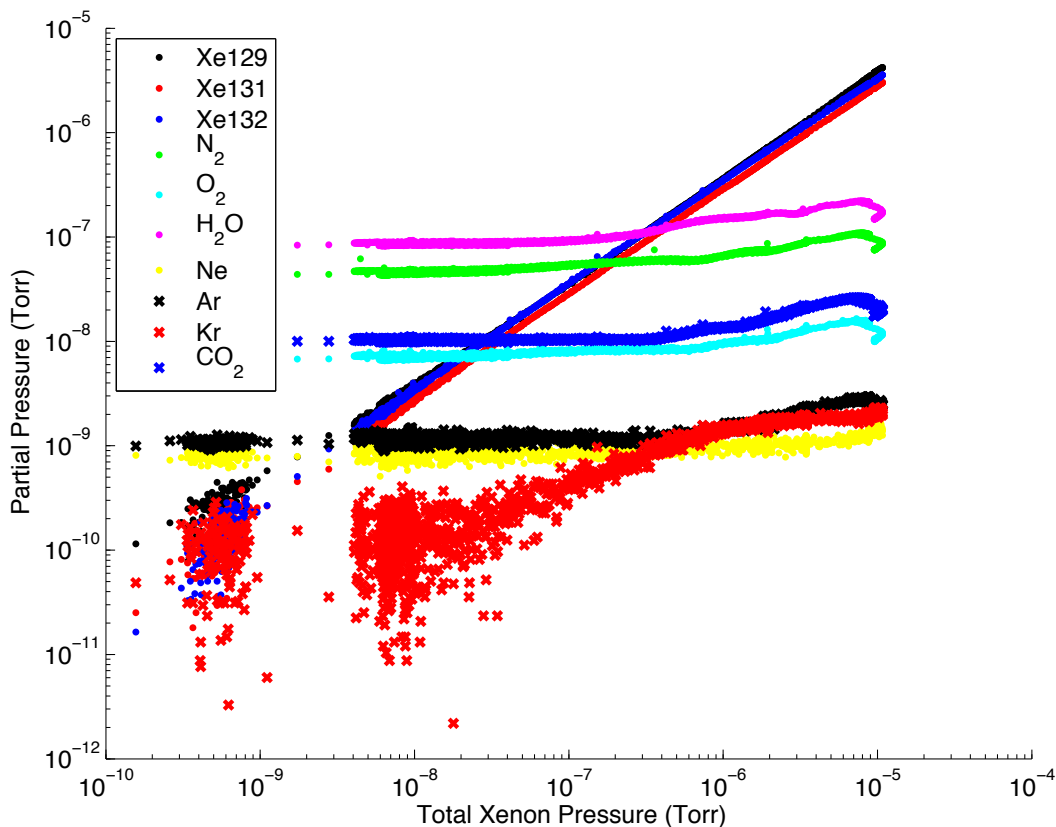


Figure 3.13: Plot of trace gas partial pressure versus total xenon partial pressure at leak valve settings from the xenon bottle completely valved off to 44, and sample window temperature of 293 K.

3.2.3 Cryostat Vacuum Generation

For some of the experiments, the cryostat system was pumped through a vacuum port by a small turbomolecular pump, backed by a roughing pump. This small turbo

failed irreparably at one point, and was not repaired or replaced. Subsequently, vacuum generation was left entirely to the cryostat system, with the port being capped off. This did not significantly affect the vacuum quality as measured with both the RGA and the ion gauge.

Due to the construction of the sample chamber of the cryostat, some vacuum leak problems were encountered. The windows of the sample chamber, gas input feed-through plate, and ion beam connector are all sealed by Viton gaskets. Though these Viton gaskets are always used with vacuum grease, occasional sporadic leaks were found due to poorly sealed o-rings. Additionally, the entire vacuum shroud sealing via a Viton gasket is not ideal for leak prevention. Though the RGA is used to monitor the system purity during experiments, an external ion gauge can not be used when spectra are being taken, due to the excessive amount of light given off by the filament.

For the ion beam, cryostat, and gas delivery systems, the RGA was used as a helium leak detector, so that any leaks could be found and fixed in a timely manner. The tubing of the xenon delivery system was baked out, but this seemed to have little effect on purity levels.

3.3 Optical Setup

3.3.1 Lasers and Dye Lasers

A variety of lasers were used for excitation of barium ions and neutral atoms. Initially, an inexpensive green diode pumped, frequency doubled Nd:YAG laser at 532 nm was used for inducing fluorescence in the neutral barium atoms. Though this wavelength was off of peak excitation of neutral barium atoms in solid xenon [76].

Initial ion identification experiments were done with a Loxel Laser Model 95 Argon-Ion laser. During these experiments, the laser was not run in an all-lines mode,

but rather by selecting the individual wavelengths through the use of an inter-cavity prism. The nine output lines of the laser ranged from 454 nm to 514 nm.

The later optical setup was designed to allow two laser beams from two different dye lasers to shine on the sample at the same time, as shown schematically in Figure 3.14. The primary laser system for resonant barium ion experiments was a Coherent CR599 dye laser, pumped by a Coherent Innova 200 Krypton laser. The krypton laser was run in an all-lines mode, with violet laser mirrors. Although capable of producing more than 4 W, 1.0 W to 3 W was more commonly used to pump the dye laser. This produced dye laser powers in the range of 1 mW to 50 mW, depending on how much usage the dye had seen and the frequency produced. With Coumarin 480 dye, wavelengths from 465 nm to 515 nm could be produced. The dye, mixed with ethylene glycol and benzyl alcohol, was replaced on occasion when the dye laser power dipped far below expected values after many hours of use.

Additionally, the Lexel Argon-Ion laser was used to pump a second Coherent CR599 Dye Laser operating with Rhodamine 110 dye. Using the 514 nm line of the Argon-Ion laser, the dye laser wavelength ranged from 540 nm to 570 nm. This laser was used for resonant excitation of barium atoms in the solid xenon matrix. Powers of this dye laser are comparable to that of the blue dye laser.

The dye lasers were not run with spectral narrowing etalons in place. The output wavelength was controlled by manually adjusting a micrometer connected to the birefringent filter in the cavity. From the width of the absorption spectrum of both barium ions and neutral barium atoms, it was determined that using the dye lasers without etalons provided sufficiently narrow excitation wavelengths. Initially, color filters were placed at the output of the dye lasers in order to block the significant spontaneous emission from the lasers. In order to reduce the background emission further, the color filters were replaced by a 488 nm laser line filter, tilted to let the on-resonance laser light through exclusively for the blue laser and a 568 nm laser line

filter for yellow dye laser (Figure 3.14). Laser light was guided to the cryostat window from the laser table via a set of mirrors, and focused on the sample by a 20 cm focal length lens. This lens, mounted on a two dimension translation stage, focused the beam to a waist radius of $13 \mu\text{m}$. To further reduce the number of ions in the laser interaction region, while increasing the rate of inducing fluorescence, a 7 cm focal length lens was used in later experiments, which produced a beam waist radius of $4.5 \mu\text{m}$.

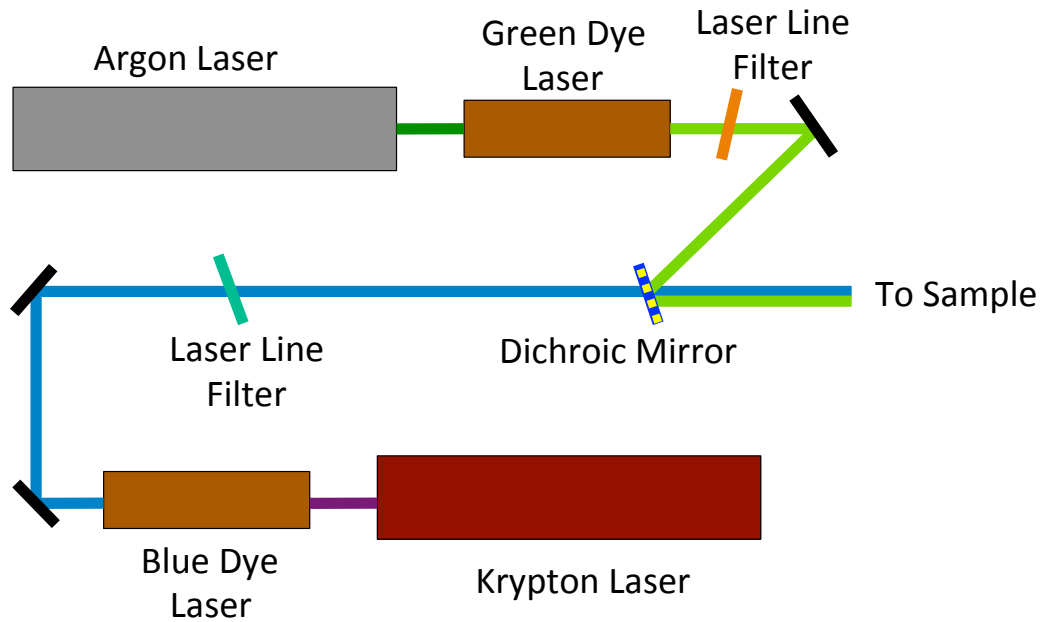


Figure 3.14: Schematic diagram of the laser system.

Some astigmatism of the focused laser beam occurs due to the tilt of the sapphire window. The astigmatism due to a tilted plate is calculated by:

$$l'_s - l'_t = \frac{t}{\sqrt{n^2 - \sin^2 U_p}} \left(\frac{n^2 \cos^2 U_p}{n^2 - \sin^2 U_p} - 1 \right)$$

where $l'_s - l'_t$ is the difference of the effective path length through the tilted plate, t is the thickness of the medium of index n , and U_p is the tilt angle of the window

[77]. The minimum area of the laser spot on the occurs between the two foci. This astigmatism results in an increase in the effective laser interaction region, from a beam waist radius of $4.5 \mu\text{m}$ to an effective waist radius of $5.0 \mu\text{m}$.

The krypton and argon lasers are both water cooled. Initially, the two lasers were alternately cooled by a Laser Innovations chiller unit, until a second identical chiller was acquired. This second chiller allows both lasers to be run simultaneously. The dye in the dye lasers was also water cooled, with recirculating building water.

3.3.2 Collection Optics and Spectrometer

Fluorescence spectra were acquired with an Acton SpectraPro 2150i spectrometer and a Spec-10 liquid nitrogen cooled CCD camera from Princeton Instruments. The grating of the spectrometer may be changed between a 300 line per mm grating and a 600 line per mm grating. A schematic diagram of the spectrometer and CCD is shown in Figure 3.15. Using the 600 line grating resulted in a wavelength resolution of approximately 0.2 nm, with a total wavelength range around 240 nm. Comparatively, the 300 line grating results in a 0.4 nm resolution, with a total viewable wavelength range of around 510 nm. The center wavelength of the wavelength range may be set in the computer program that controls the spectrometer and takes the spectra. The input of the spectrometer is limited to an f-number of 4 ($f/4$). The CCD features a high quantum efficiency of 90% in the visible wavelengths. In slow mode, two photoelectrons produce a single ADC count. Cooling the CCD with liquid nitrogen reduced the dark counts per pixel to a negligible level for all but the longest exposures.

The CCD is comprised of an array of 1340 horizontal pixels by 400 vertical pixels, each $20 \mu\text{m}$ by $20 \mu\text{m}$ for a total imaging area of 26.8 mm by 8 mm. When the camera is operated in imaging mode, each pixel can be read out individually, so that a complete image may be formed. If the spectrograph grating is used in zero order, the spectrometer and CCD act as an imaging camera, useful for setup of the experiment

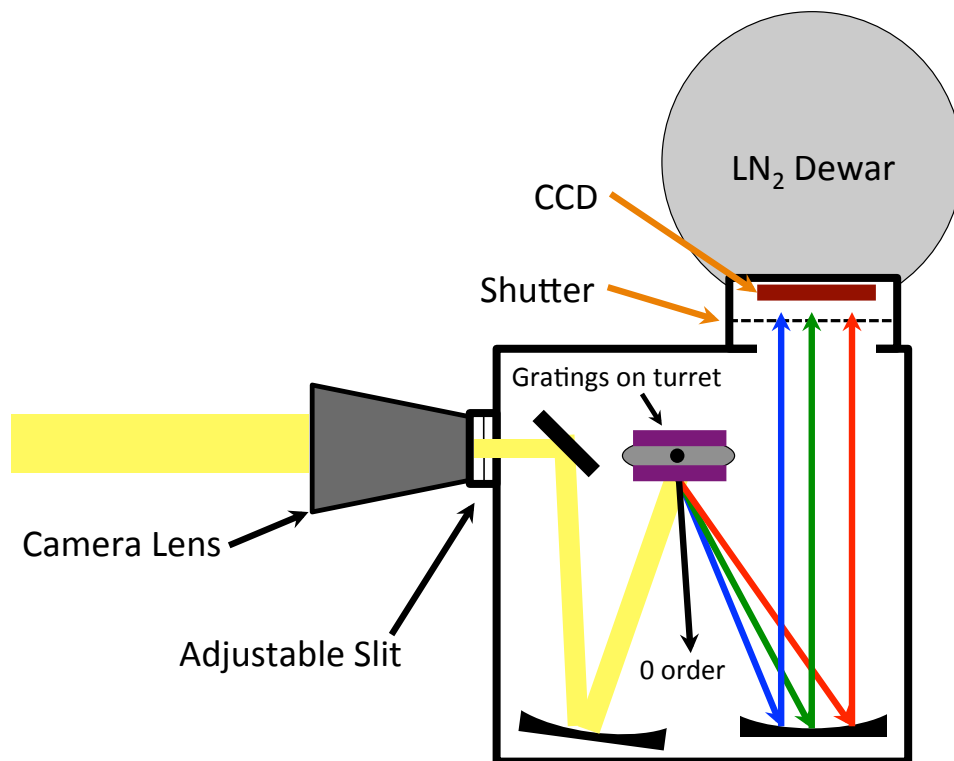


Figure 3.15: Schematic drawing of the spectrometer and CCD.

and imaging of fluorescence. In spectroscopy mode, signals from pixels in the same column in an assigned region of interest, each receiving the same wavelength from the spectrometer, are grouped and added, giving a total count for that wavelength. Each pixel has a saturation point of 65535 counts.

Neighboring pixels of the CCD may also be summed together by binning an assigned number of horizontal pixels together. Though spectral resolution is lost in the process, binning increases the signal-to-noise of the spectrum, and is useful for detection of small signals in broad spectral lines.

In early experiments, fluorescence light was carried to the spectrometer by a multi-mode fiber bundle, shown by Figure 3.16 A. The end of the fiber at the spectrometer input consisted of a linear array of fibers. This vertical arrangement of fibers on

the spectrometer side of the fiber acts as an input slit for the spectrometer. It was held in place and aligned by a custom-made aluminum chuck and plate that could be removed from the spectrometer, while still keeping proper alignment of the fiber. The collection side of the fiber had a circular bundle of fibers. It was attached to a collimator, which collected fluorescence emitted by the ions and atoms in the matrix on the cryostat window. The collimator, a 1 cm diameter, 2 cm focal length lens, focused light onto the face of the optical fiber. The collimator and filter set was positioned off-axis from the laser beam. Because the fluorescence was emitted in all directions, this did not affect the collection efficiency, but did drastically reduce the amount of laser light scattered into the camera.

A Raman filter, which blocked laser light at $OD \geq 5$, but allowed any light to the red of the cut-off wavelength to be passed with nearly 100% transmission was placed in front of the collimator. Several Raman filters were used. By positioning these filters at an angle relative to the direction of the light, the cut-off wavelength can be shifted to the blue by tens of nanometers, allowing for light more to the blue of the original cut-off wavelength to be transmitted. The transmission curves at normal incidence of two Raman filters with cut-off wavelengths of 526 nm (red curve) and 581 nm (blue curve) are shown in Figure 3.17.

The optical fiber collection optics were easy to set up and use, but the collection efficiency was 2.6×10^{-5} [76]. In order to improve the collection efficiency, and thereby improve the minimum number of ions able to be detected, the collection optics were changed. Instead of an optical fiber bundle, a 5 cm focal length lens was used to collect the fluorescence and make a parallel beam, which was then directed to the spectrometer by mirrors. This is shown in Figure 3.16 B. The spectrometer was fitted with a 50 mm camera lens focused to infinity, which imaged the sample on the input slit of the spectrometer. The lens was set to $f/4$ to match the acceptance of the spectrometer. The adjustable slit of the spectrometer allowed only the imaged

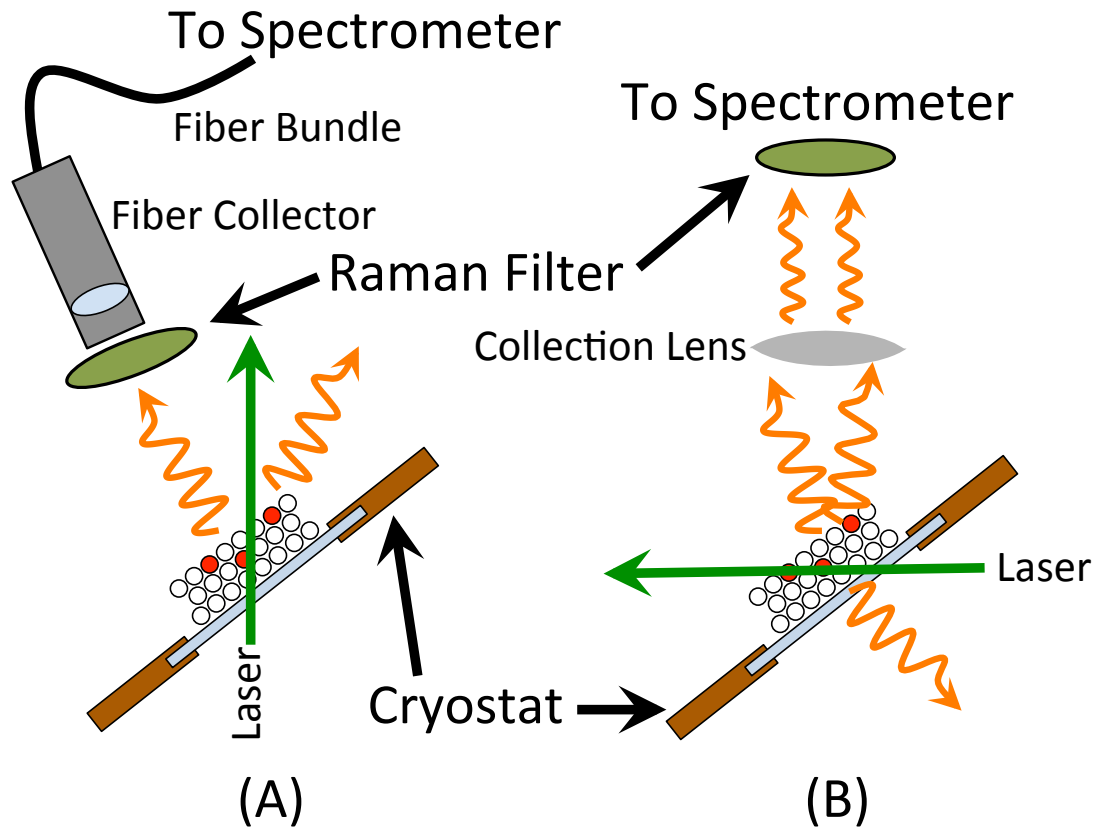


Figure 3.16: Schematic diagrams of the two collection optics. (A) is the optical fiber method. (B) is the 5 cm focal length lens method is on the right. Both utilize a Raman filter to block the laser scatter. Black outlined white circles on the sapphire window represent xenon atoms, while red circles indicate barium ions or neutral atoms.

laser excitation region to enter the spectrometer.

Table 3.1 lists the factors that result in the detection efficiency from the new collection optics. The combination of the 5 cm focal length lens and the 50 mm, $f/4$ camera lens of the spectrometer results in a collection efficiency of 3.9×10^{-3} . The 5cm collection lens has a calculated transmission of 0.92. The two mirrors that direct the fluorescence to the spectrometer have reflectivities of 0.95. The cryostat window is also taken into account with a 0.99 transmission, due to it having anti-reflection coatings. The spectrometer has a specified transmission of 50%. The CCD has a quantum efficiency of 90%, and requires two photons to register as one count.

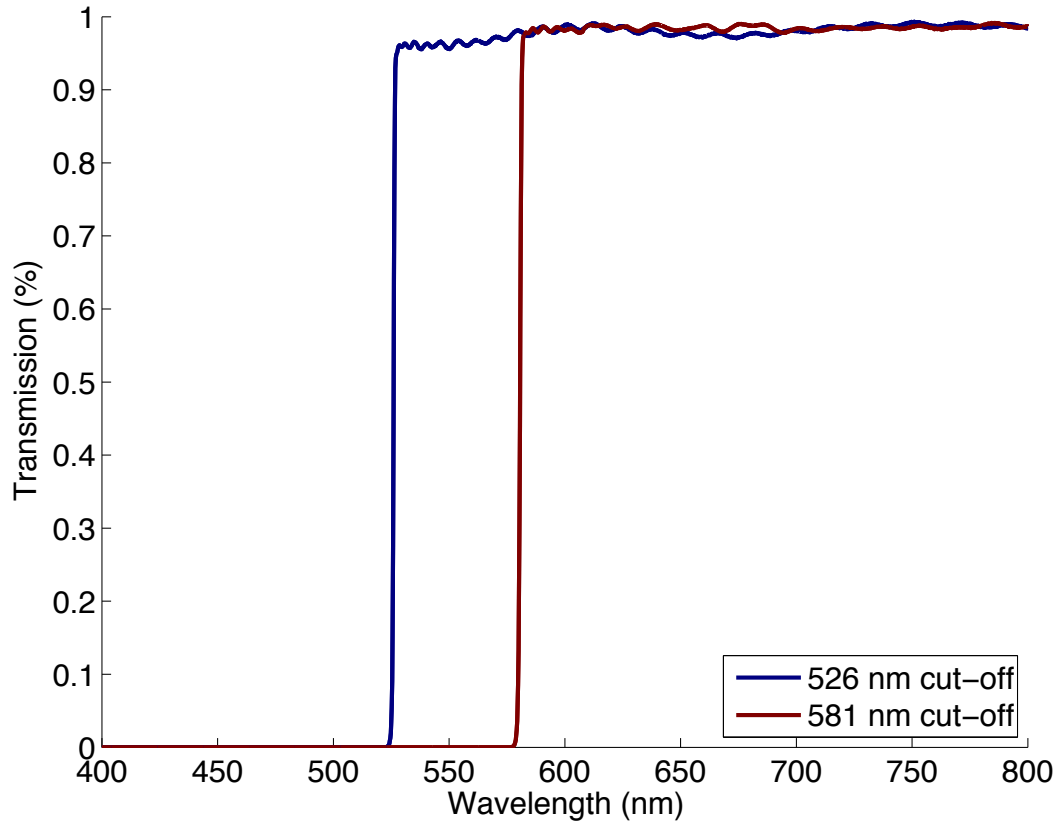


Figure 3.17: Transmission of two Raman filters used in fluorescence collection.

These factors result in a total detection efficiency of 7.2×10^{-4} . This value assumes a perfectly aligned and parallel beam

3.4 White Light Absorption

To obtain neutral Ba absorption spectra, white light from a halogen lamp was roughly collimated and directed through the sample. The transmitted light was collected by the camera lens and coupled directly into the spectrometer. The Beer-

Table 3.1: Table showing the efficiencies of the collection optics shown in Figure 3.16 B, along with the total collection efficiency for the detector.

Item	Efficiency
Collection Efficiency	3.9×10^{-3}
Collection Lens Transmission	0.92
Collection Mirrors (2)	0.95
Cryostat Window	0.99
Spectrometer transmission	0.5
Photon to Count	0.5
CCD Quantum Efficiency	0.9
Total	7.2×10^{-4}

Lambert Law for absorption is defined as:

$$I(\lambda) = I_0(\lambda)e^{-a(\lambda)} \quad (3.4)$$

I_0 and I are the light intensities entering and leaving the sample, respectively, and $a(\lambda)$ is the absorbance. The absorbance can be related to the absorption cross section $\sigma(\lambda)$:

$$a(\lambda) = \sigma(\lambda)Nl$$

where N is the density of atoms and l is the path length through the particles. The absorption cross section can be calculated via

$$\sigma(\nu) = A_{21} \frac{g_2}{g_1} \frac{c^2}{8\pi\nu^2} g(\nu)$$

as discussed in Section 2.6. Therefore the number of atoms per unit area, Nl is calculated by taking the negative log of the ratio of the white light spectra before atomic deposition (I_0) to the spectra after (I) divided by the absorption cross section.

3.5 Data Collection

A National Instruments BNC-2090 interface was used for computer control of experimental parameters and for recording of diagonal and analog data. A LabView program recorded the temperature of the cryostat cold finger and laser power for each frame of the camera. A microscope slide acted as a laser pick-off. As the percent of transmission of the microscope slide was well known, the on-sample laser power could be calculated.

The National Instruments interface also controlled the microsecond pulsing unit for the pulsing plates through a separate LabView program. A constant series of pulses, or a set number of pulses between a set number of camera frames could be programmed.

Pre-amp signals were recorded by a Tektronix digital oscilloscope along with the pulsing plate voltages. The scope signals were saved on a USB memory stick.

3.6 Ion Number Calculation and Background Considerations

The ion current I in the $D = 2$ mm diameter area of the Faraday cup was measured during experiments using an electrometer. Thus the ion current density at the sample is $CI/\pi D^2$, where C accounts for the change in density at the cryostat window. To find the ion current density at the sample window, a Faraday cup was installed in place of the sample window. While doing so, the ion beam tuning parameters for a

variety of source energies were found. For energies from 100 eV to 2000 eV, the ion current density decreased by a factor of 2 from the normal measurement Faraday cup to the Faraday cup in place of the sample window when first tested in April of 2011. A repeat of this test in May of 2012 produced a C value of 2 for energies of 500 eV to 2000 eV, similar to the April 2011 test. The check of C in May of 2012 was performed days before the critical experiments of this thesis.

The excitation laser only interacts with a portion of the ion beam deposit area. A measure of the effective area of the laser beam is the power divided by the intensity I_0 , in the center of the laser beam, or $A_{laser} = \pi w^2/2$, where w is the radius of intensity I_0/e^2 . The number of ions deposited in the laser region is then calculated by

$$N_{Laser} = \frac{I_{ion}t_{dep}}{q} \frac{C}{\pi D^2} \frac{\pi w^2}{2} = \frac{I_{ion}t_{dep}C}{2q} \frac{w^2}{D^2}$$

where t_{dep} is the length of time of the ion deposit, q is the electron charge, and I_{ion} is the ion current of the beam. The number of ions deposited in the laser region for the pulsed ion beam is found by replacing t_{dep} with $t_{pulse}N_{pulse}$:

$$N_{Laser} = \frac{I_{ion}t_{pulse}N_{pulse}C}{2q} \frac{w^2}{D^2}$$

where t_{pulse} is the length of ion pulse, which is 1 μs , and N_{pulse} is the number of pulses triggered. When observing the fluorescence of neutral barium atoms from an ion beam deposit, N_{Laser} serves as only an upper limit on the number of Ba atoms in the laser beam because the percentage of ions neutralized upon landing is not yet known. Due to the 45° angle between the laser direction and the window angle, the effective laser area is increased by a factor of $\sqrt{2}$. The ion beam area is also increased by this same factor for the same reason. These two factors cancel, and do not increase the atoms or ions in the focused laser beam.

The pulsing plates deflect the ions from the beam path except when pulses are

triggered. Nevertheless, when the ion beam is deflected, a small number of neutral barium atoms arrive at the sample per each second the ion beam is exposed to the cryostat. To account for the contribution to the spectrum of these atoms (S_{drift}), each spectrum for pulsed ion beam deposits has two background spectra. One background signal, S_{window} , is just the sapphire window background. A second spectrum, S_{defl} , is taken after the sample window has been open to the ion beam for a set amount of time after the sample window has been open to the ion beam for a set amount of time with the beam deflected. This amount of time is the same as the amount of time to deposit the pulses. The signals from the pulsed ion beam and the deflected ion beam are then:

$$S_{pulsed} = S_{neut} + S_{drift} + S_{window}$$

$$S_{defl} = S_{drift} + S_{window}$$

where S_{neut} is the signal from only the pulsed ion deposit. This can be calculated as

$$S_{neut} = S_{pulsed} - S_{defl}$$

The window only background S_{window} spectrum is not strictly needed, as both S_{pulsed} and S_{defl} both contain that signal. It is needed, however, if a spectrum of S_{drift} is desired.

4 Results

In this chapter, results from laser induced fluorescence experiments of neutral barium atoms and barium ions in solid xenon are presented. The fluorescence and absorption spectra of neutral barium atoms in solid xenon are presented in Section 4.1. This section also discusses the new data on a new fluorescence peak, the temperature dependence of the fluorescence peaks, and the bleaching of the fluorescence signal. Section 4.2 discusses the improvement of the fluorescence efficiency of neutral barium. Fluorescence spectra for small numbers of neutral barium are shown in Section 4.3. Some preliminary experiments of imaging the neutral barium atom fluorescence is discussed in Section 4.4. The remaining sections of this chapter are dedicated to the results from experiments of Ba^+ implanted into solid xenon matrices. Five emission lines come from one excitation line, all with nearly equal line spacing. Two possible assignments for these lines are presented. It is possible that these lines may be due to fluorescence of Ba^+ in solid xenon, though they may also come from molecular transitions.

4.1 Neutral Barium Fluorescence and Absorption in Solid Xenon

Absorption and emission spectra of neutral barium atoms in solid xenon were first presented in Brian Mong's Ph.D. thesis [76]. A typical white light absorption spectrum of neutral barium atoms in solid xenon is shown in Figure 4.1. This absorption has a full-width at half-maximum of 30 nm. It also has several distinct features, shown by the multiple gaussian fit shown in Figure 4.2. Peak absorption occurs at 558.5 nm, which is only slightly red-shifted from the vacuum $6s^2 \ ^1S_0 \rightarrow 6s6p \ ^1P_1$ transition wavelength of 553.5 nm.

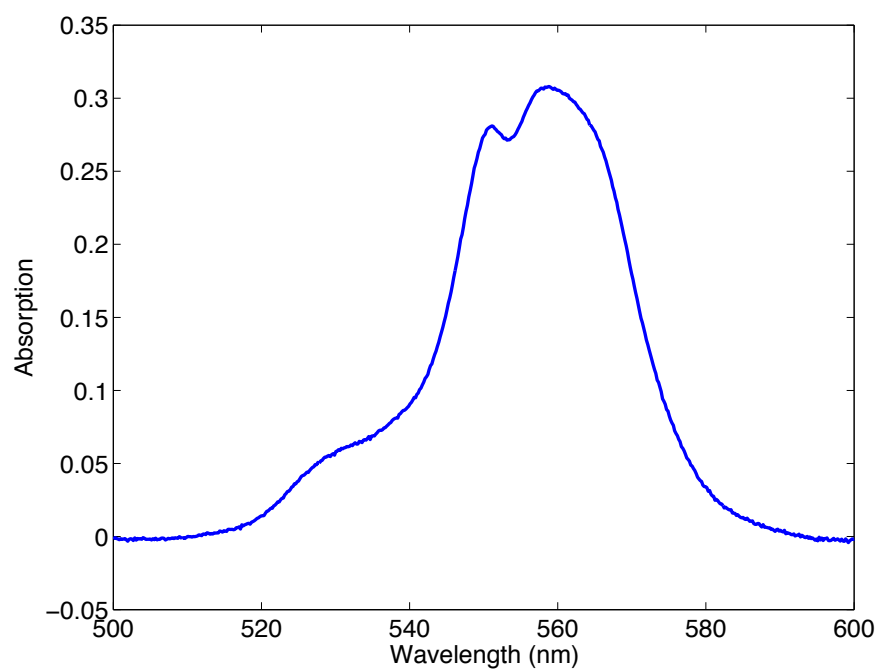


Figure 4.1: Absorption spectra of neutral barium in solid xenon, obtained from white-light absorption methods.

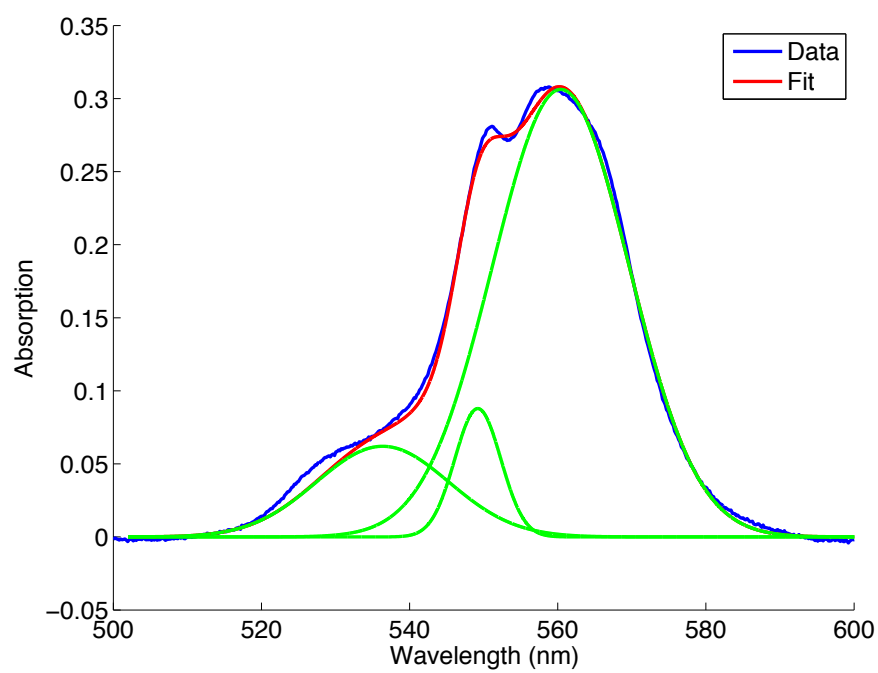


Figure 4.2: Multiple gaussian fit of the absorption spectra.

The primary fluorescence line for neutral barium in solid xenon was determined to be at 590 nm [76], as shown in Figure 4.3. This fluorescence peak was used for all efficiency, bleaching, and small number experiments. One additional fluorescence line at 580 nm was discovered for the first time in this work and attributed to neutral barium. This additional line may be due to neutral barium atoms being in a different site in the matrix. This 580 nm peak is not present in Figure 4.3 due to different on-resonance excitation wavelengths of the two fluorescence peaks. Multiple peak emission of neutral barium atoms has been seen in solid argon [76].

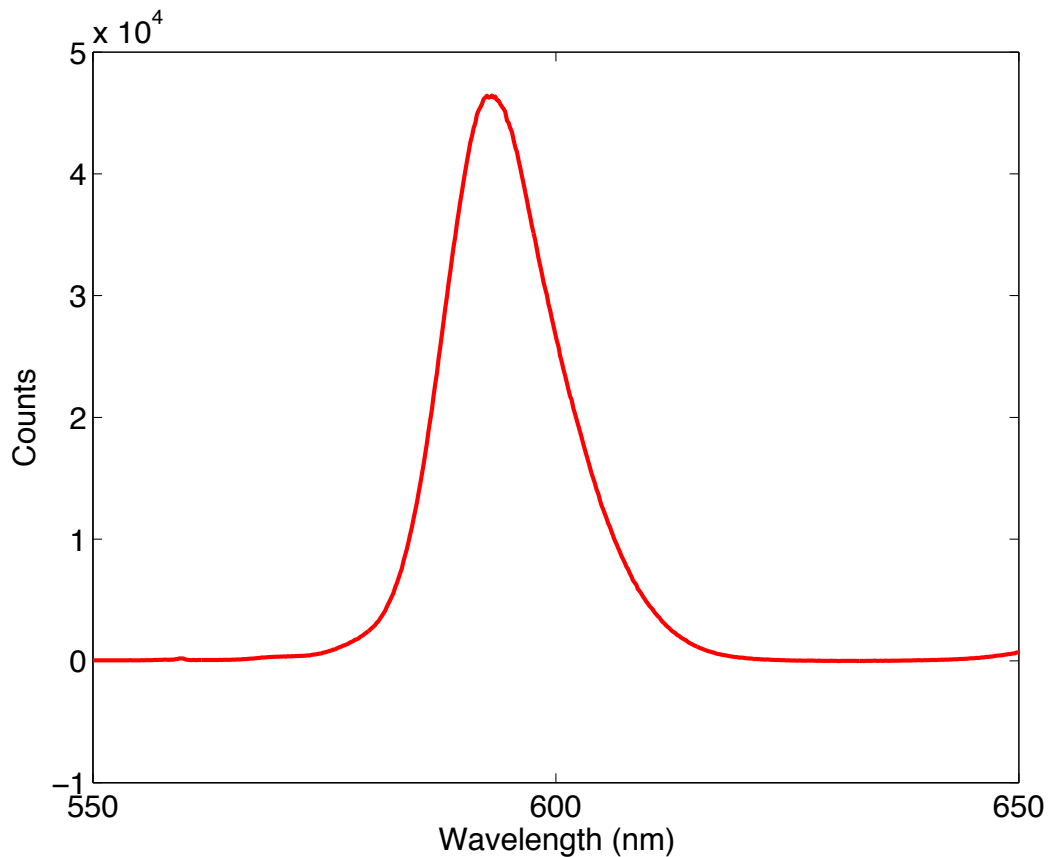


Figure 4.3: Neutral barium fluorescence spectrum in solid xenon when excited with 558.5 nm laser light. The primary peak lies at 590 nm.

An excitation spectrum of the 580 nm and 590 nm fluorescence peaks is shown in

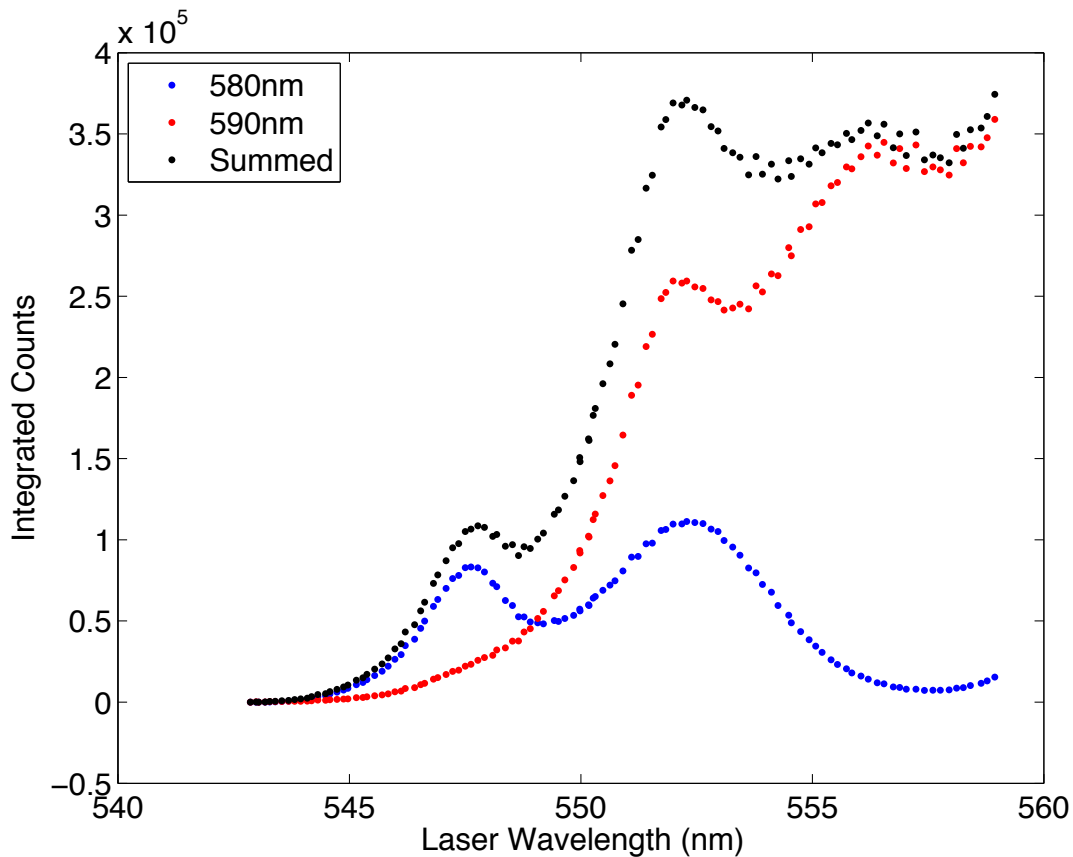


Figure 4.4: Excitation spectra of the 580 nm and 590 nm neutral fluorescence peaks. The vertical axis is the integral of the fit for each peak.

Figure 4.4. Excitation spectra such as these are produced by varying the dye laser wavelength, and measuring the total integrated fluorescence peak counts. The 580 nm peak has two lower wavelength excitation peaks, whereas the 590 nm excitation spectrum has peaks at higher wavelengths. Though these do not match the absorption spectra exactly, some similar features can be seen.

A cold probe used in the EXO Full TPC may grab a barium atom or ion in solid xenon at just below the triple point. The tagging process may occur at a lower temperature in vacuum or gaseous xenon just outside of the detector. To test the effect of such temperature changes, the sample temperature was changed using the

cryostat heater. The two 580 nm and 590 nm fluorescence peaks responded differently to annealing of the sample, as shown in Figure 4.5. Upon deposition at 10 K, with 552 nm excitation, the 590 nm peak is usually much larger than the 580 nm peak, as shown by the dark blue line in Figure 4.5. Upon warming of the sample, the 580 nm peak increased, while the 590 nm peak decreased, as shown at 16 K, 25 K, and 32 K with the light blue, teal, and green lines, respectively. Re-cooling the sample resulted in a decrease in the 580 nm peak, while the 590 nm peak grew (yellow, red, and dark red dashed lines).

The areas of each peak, calculated by a double gaussian peak fit, are shown in Figure 4.6 as a function of temperature. As the sample temperature rose from 10 K to 30 K (point 1 to point 2 in Figure 4.6), the 590 nm peak decreased. In this same temperature increase, the 580 nm peak increased. When cooled back to 10 K (point 3), the 590 nm rose, but suffered some permanent loss. The 580 nm peak decreased and also suffered permanent loss. This occurred when the sample was annealed to 40 K as well (point 4 and 5). A sharp drop in signal occurs at temperatures above 45 K (point 6). This is not attributed to sublimation of the solid xenon matrix, which occurs at 75 K. It might be interesting to know how mobile the barium atoms and impurity molecules are in the matrix at these temperatures.

Neutral barium atoms also suffer a decrease in fluorescence signal over time due to some kind of bleaching or optical pumping. Optical pumping is a temporary loss of fluorescence due to a population buildup in an atomic state that does not interact with the excitation laser. This population buildup, once excitation is stopped, eventually decreases, allowing for further excitations. Bleaching, however, is a permanent loss of fluorescence signal due to some other mechanism, such as chemical reactions or changes in the matrix. For neutral barium atoms in solid xenon, the fluorescence signal never goes to zero, but rather approaches a steady-state value. Such bleaching is shown in Figure 4.7. Fluorescence signal drops by a factor of 3 or more in a few

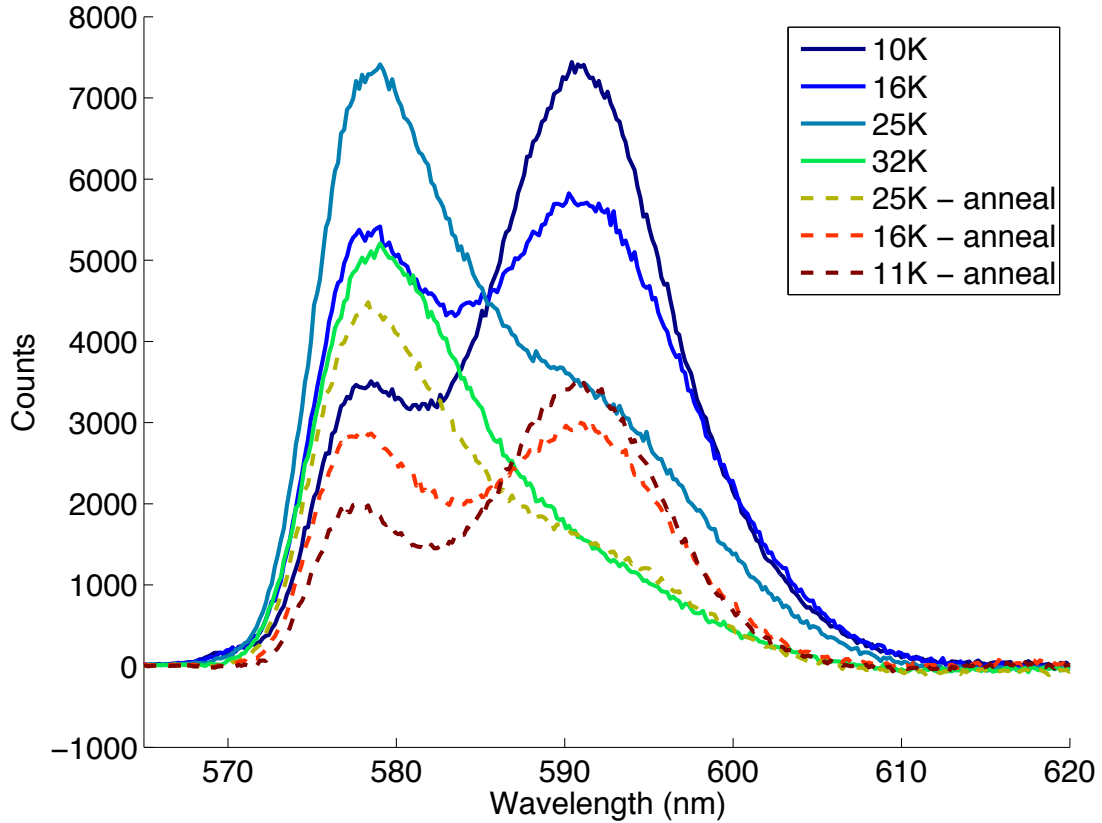


Figure 4.5: Selected spectra of the annealing process of neutral barium, excited with 552 nm laser light. During the warming process, the 590 nm peak decreases, while the 580 nm peak increases. Cooling the sample after warming to 32 K shows a return of some of the 590 nm peak.

seconds, then decreases slowly after that. The blue curve is a fit of a single exponential decay of the form $Ae^{-Bt} + F$ to the data. The red fit is a double exponential decay fit of the form $Ae^{-Bt} + Ce^{-Dt} + F$. The values of these the fitting parameters are tabulated in Table 4.1. The single exponential decay does not fit the data, though the double exponential decay fits the data very well. This particular bleaching of fluorescence signal was present with a focussed laser with a low laser power of only $22 \mu\text{W}$. This decrease of fluorescence occurred at a variety of excitation laser wavelengths and powers. Further evidence for bleaching of neutral barium is exhibited by a decrease

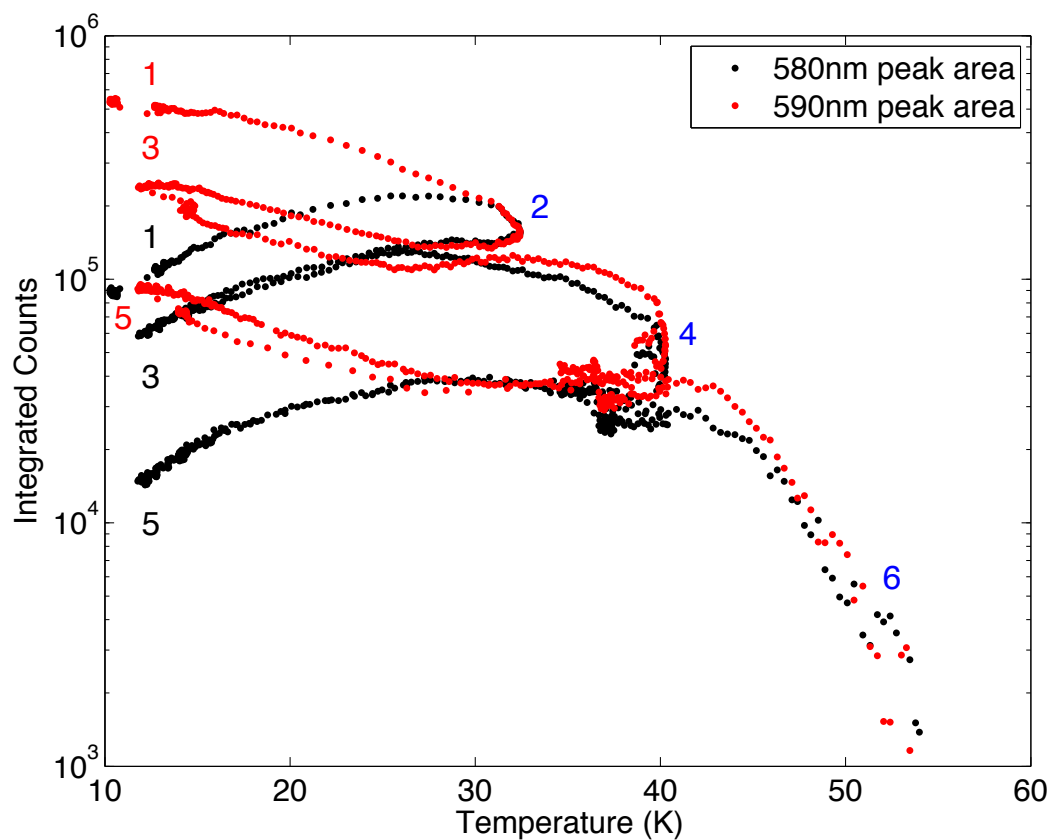


Figure 4.6: Integrated counts of the 580 nm and 590 nm neutral barium fluorescence peaks as a function of temperature, excited with 552 nm laser light. The numbers indicate the order of the annealing process.

in white light absorption after a laser excitation, as shown in Figure 4.8. Though the neutral barium fluorescence peak does suffer a decrease on the 10 second time scale, the fact that it reaches a non-zero steady state value at long time scales is a positive result. Because of this, the neutral barium fluorescence light may be collected for long periods of time. The fluorescence does not return to its original value if the excitation is stopped and then restarted after some time. These factors indicate that the decrease of neutral barium fluorescence in solid xenon is not due to optical pumping, but rather due to bleaching.

When Ba^+ ions are deposited onto solid xenon matrices, significant neutral barium

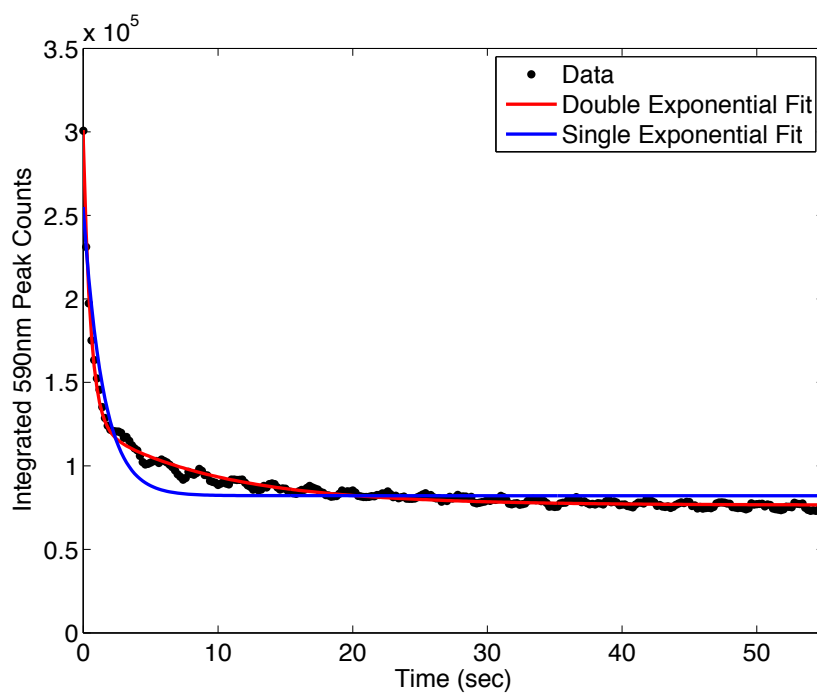


Figure 4.7: Decrease of neutral barium fluorescence signal over time due to bleaching.

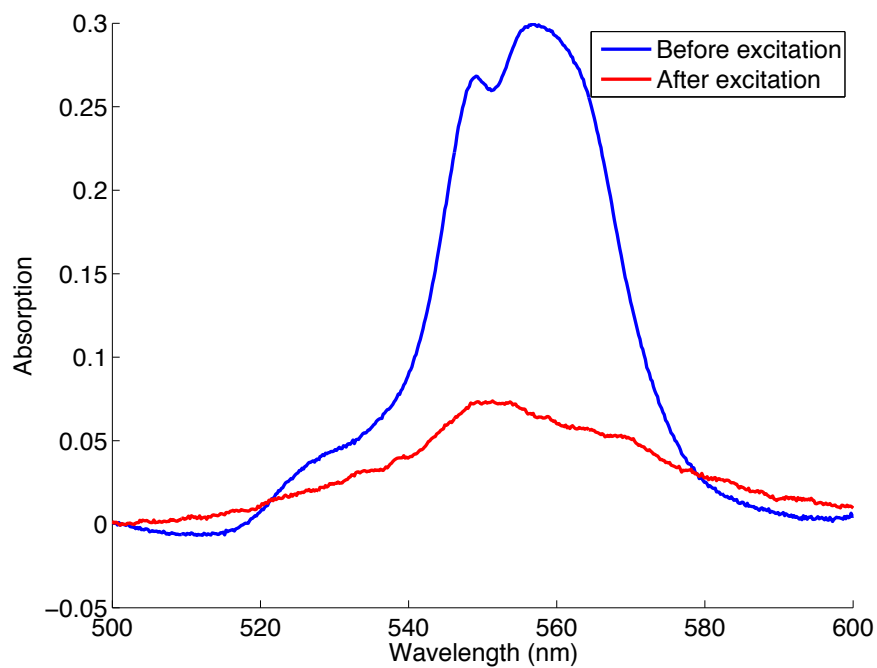


Figure 4.8: White light absorption of neutral barium before and after laser excitation.

Table 4.1: Details of the single and double exponential fits of the decay of fluorescence signal in neutral barium

Constant	Single Exponential Value	Double Exponential Value
A	1.49×10^5	7.95×10^5
B	0.673	1.856
C	-	4.72×10^4
D	-	0.107
F	82158	76527
$\frac{A+C}{F}$	1.80	1.66

fluorescence is observed. Thus a substantial fraction of the deposited ions must have been neutralized on impact with the matrix. Figure 4.9 shows the 590 nm neutral fluorescence peak after deposition of barium ions at a variety of beam energies. The 580 nm peak is present as well, due to 552 nm excitation in this experiment. The fluorescence in Figure 4.9 has been normalized to the ion current for each landing energy. The deposit times are equal for all deposit energies. The lowest landing energies gave the largest neutral fluorescence signals. Although this indicates a larger percentage of the ions entering the matrix neutralize at lower energies, this experiment needs to be repeated. Possible systematic effects such as bleaching and deflection of ions due to charge buildup need to be considered before such a conclusion can be made.

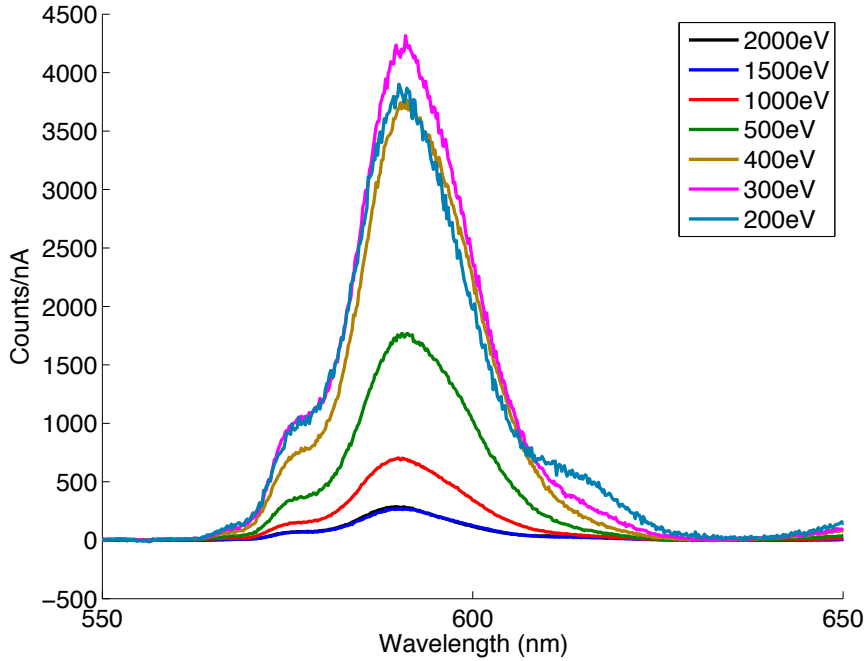


Figure 4.9: Neutral barium fluorescence from 555 nm excitation light, normalized to ion current after deposition of barium ions from the ion beam at a variety of landing energies. A five minute deposit time was used for all energies.

4.2 Fluorescence Efficiency of Neutral Barium in Solid Xenon

The typical neutral barium fluorescence efficiency was in the 0.1% range in previous work [76] and for most of this work. An important discovery of this work is that fluorescence efficiency is highly dependent on the xenon leak rate used. The measured fluorescence efficiency as a function of xenon gas leak valve setting is shown Figure 4.10. Higher leak valve settings, which result in cleaner xenon matrices, result in a higher fluorescence efficiency. This could be due to a higher probability at low leak rates of impurities in the matrix, which quench the Ba fluorescence. Because of this finding, the highest practical leak rate was used to maximize fluorescence sig-

nal at low numbers of ions or neutrals. This method led to a maximum short-term fluorescence efficiency of 22%. The fluorescence efficiency values of Figure 4.10 were calculated for the signal immediately following exposure to excitation laser light, and therefore to not include a factor of 3 decrease due to bleaching over time. Though 22% fluorescence efficiency occurred with a leak valve setting of 45, a leak valve setting of 55 might be required to reproduce this result after the change in the leak valve mentioned in Section 3.2.2.

In general, experiments done later in the day resulted in a higher fluorescence efficiency. This may be due to an overall purging effect of repeated experiments freezing and melting xenon samples, resulting in a lower residual gas pressure at the sample. Also, running the barium getter for extended amounts of time results in barium being deposited on the vacuum chamber walls. Barium on the walls of the vacuum chamber could act as a getter for residual gas, resulting in higher fluorescence efficiencies.

The matrix impurity level for this experiment was, at best, 7.5×10^{-5} . For the EXO experiment, impurities are in the parts per billion or sub parts per billion range [78]. Thus, a reduction fluorescence efficiency due to impurities should not occur with a barium atom frozen in a solid xenon ice from the EXO TPC.

4.3 Spectra of Small Numbers of Ba from Ba⁺ Deposits

The goal of the tagging effort for the EXO experiment is a demonstration and then implementation of single Ba atom or ion detection with high efficiency. As a major step toward this goal, small numbers of atoms or ions were deposited and detected in solid xenon with the CSU apparatus.

White light absorption measurements can give a calibrated count of the barium

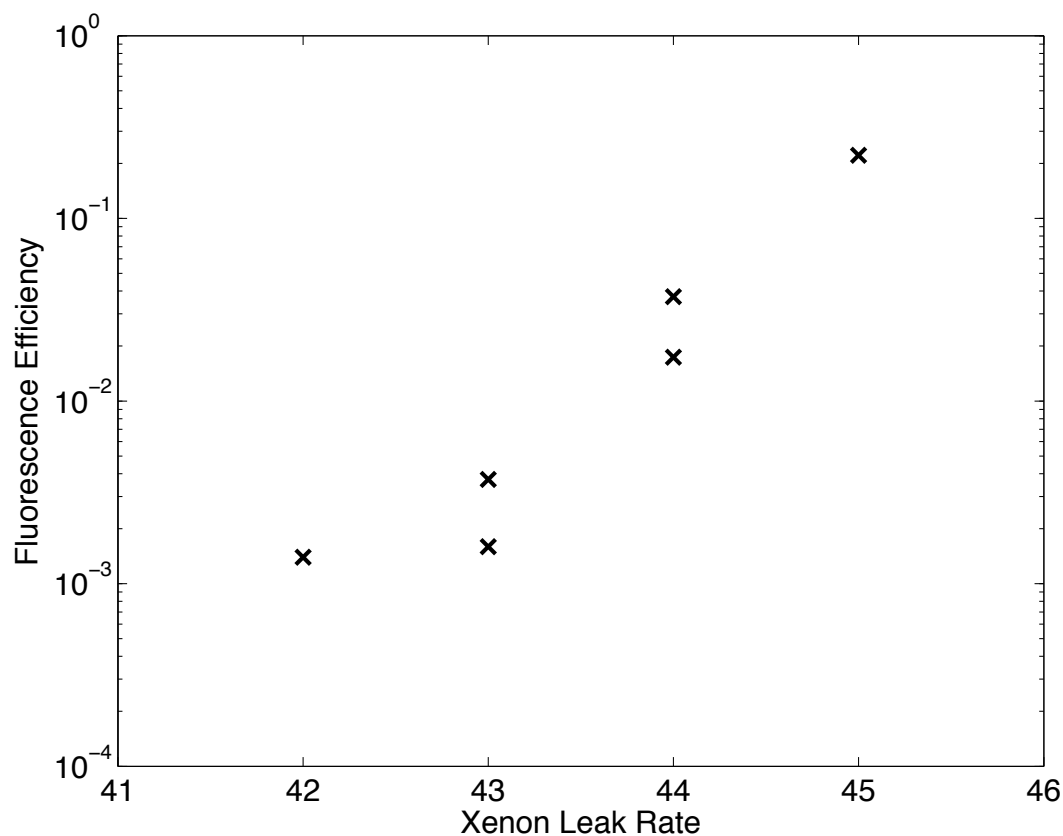


Figure 4.10: Fluorescence efficiency versus leak valve setting for the xenon source gas. The highest efficiency achieved was 22%.

atom density in the matrix in the 1×10^{11} atoms/mm² range. This density of atoms is too large for small number detection. The getter used to deposit neutral barium is hard to turn on and off quickly in order to control the number of deposited atoms. Since deposition of barium ions by the ion beam results in a neutral barium fluorescence signal, some fraction of the deposited ions must neutralize on landing on the xenon matrix. A measurement of the number of implanted ions gives an upper limit on the number of neutral barium atoms in the laser region. As an example, 1 second of ion beam deposit at a typical ion current of 10 nA would give 1×10^{10} ions/mm² deposited in a 6 mm² area on the sample. In order to deposit small numbers of Ba⁺

ions, the pulsing plates of the ion beam were employed to transmit short ion pulses with a known number of particles.

A small number of neutral Ba atoms from the source or from sputtering by the deflected ion beam drift to the sapphire window when the Faraday cup that normally blocks the ion beam is retracted, as discussed in Section 3.5. It is necessary to subtract this signal of unknown number of neutrals from the neutral fluorescence signal due to the pulsed ion beam deposit. For example, if sending 1000 pulses to the sample takes a total of 5 seconds, the fluorescence signal due to having the ion beam open to the sample for 5 seconds but with no pulses going must be subtracted from the signal from 1000 pulses. This leaves only the signal due to the 1000 pulses. Because of bleaching of the fluorescence signal, this needs to be done in exactly the same way with a separate deposit. For 100 pulses of $1 \mu\text{s}$ each, the ion density would be 1×10^6 ions/ mm^2 , or 37 ions in the minimum laser beam area used, $32 \mu\text{m}^2$.

To further reduce the number of barium ions or neutrals observed, the laser interaction region was reduced. Originally the laser was unfocused on the sample with a beam radius of 1mm. This was first reduced to a $13 \mu\text{m}$ beam waist radius, then to a $4.5 \mu\text{m}$ waist radius by using two different lenses to focus the laser. By doing so, the number of ions or atoms in the laser spot size is reduced, and the higher intensity light increases the number of excitations per second for each atom or ion.

The neutral fluorescence spectrum of $\leq 460 \text{ Ba}^+$ ions deposited in the laser detection region from 1000 pulses at 2000 eV is shown in Figure 4.11. The laser power was 5 mW, and a camera exposure of 100 seconds was used. Figure 4.11 shows a clear neutral barium fluorescence peak at 590 nm with a shape that matches Figure 4.3 and a good signal to noise ratio. The fluorescence efficiency of this spectrum was 0.1%, assuming 100% neutralization of the ions.

A spectrum of a smaller number of neutral barium atoms detected is shown in Figure 4.12. This spectrum is of ≤ 64 barium atoms in the laser region from a deposit

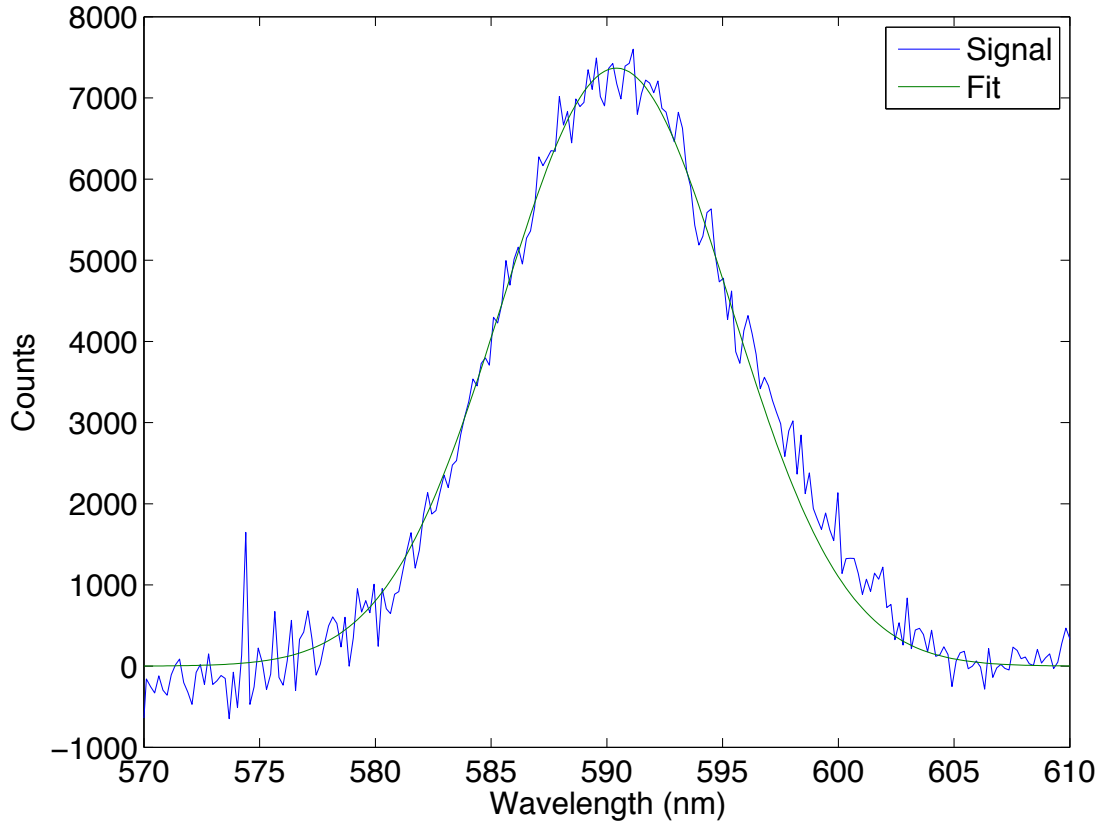


Figure 4.11: Spectrum of ≤ 460 neutral barium atoms in the laser detection region, along with a gaussian fit of the data.

of 50 pulses at 33 nA at 2000 eV deposit energy. The camera exposure time for this spectrum was 100 seconds. It shows a clear fluorescence signal. This low number of neutral atoms gave almost 100,000 total counts in the fluorescence peak. These two low number experiments were done before the leak valve underwent a change.

The above experiments were repeated when using a leak valve setting of 55, equivalent to $0.7 \mu\text{m/s}$ xenon matrix growth rate, as extrapolated from data in Figure 3.11. This large growth rate increases the matrix purity, and increases the fluorescence efficiency, as shown in Figure 4.10. A bandpass filter was used that allowed only 575 nm to 610 nm light to pass to the spectrometer.

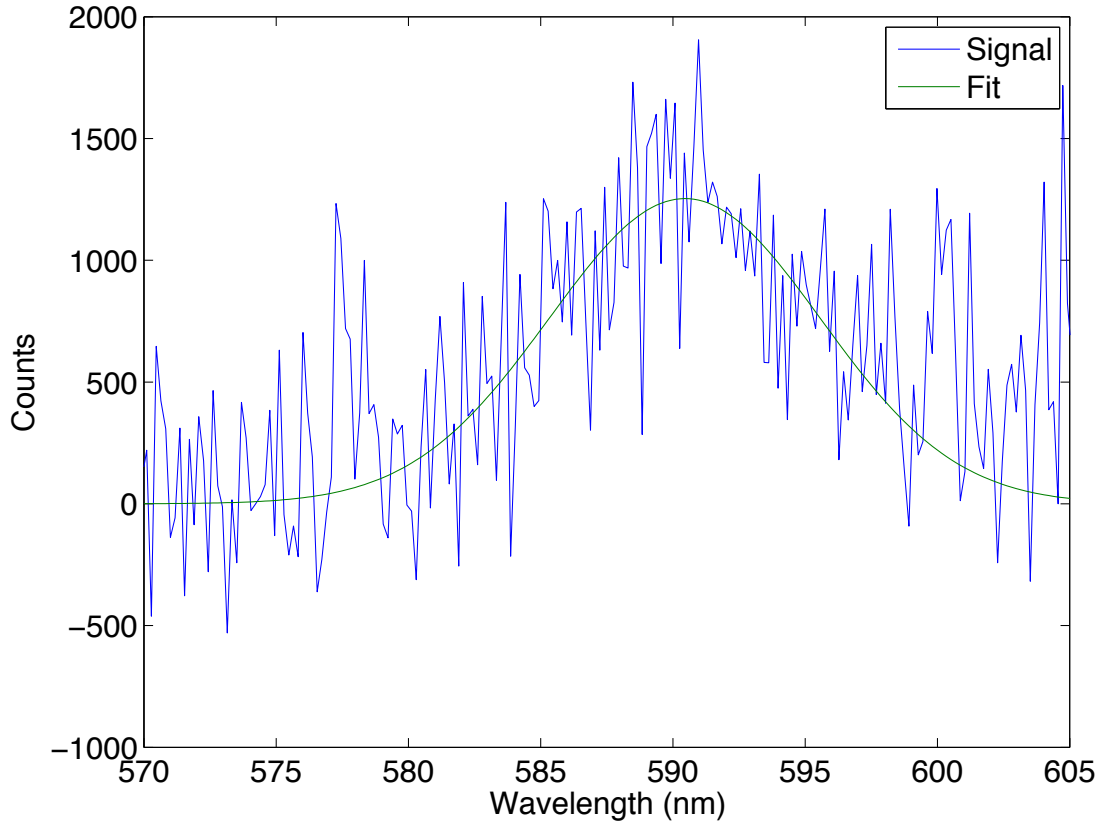


Figure 4.12: Small number spectrum of barium neutral atoms. This spectrum corresponds to ≤ 64 atoms in the detection region.

The spectra of a 100 pulse ion deposit, a 10 pulse deposit, two zero pulse deposits (ion beam deflected, but exposed to the sample for the same amount of time as the 100 and 10 pulse deposits), and two background spectra are shown in Figure 4.13. The background spectra change throughout the experiment. The zero pulse spectra change throughout the experiment as well, showing a small number of neutrals arrive at the sample when the beam is deflected but the ion beam is exposed to the sample. Both the 100 pulse and the 10 pulse deposits gave more signal than the 0 pulse deposits. The two background spectra were actually 10 pulse deposits, though they both had no fluorescence signal for some unknown reason. Fluorescence efficiency

for these to deposits is effectively zero. The variation in background spectra allows the background to be scaled to properly to subtract from the 100, 10, and zero pulse deposits.

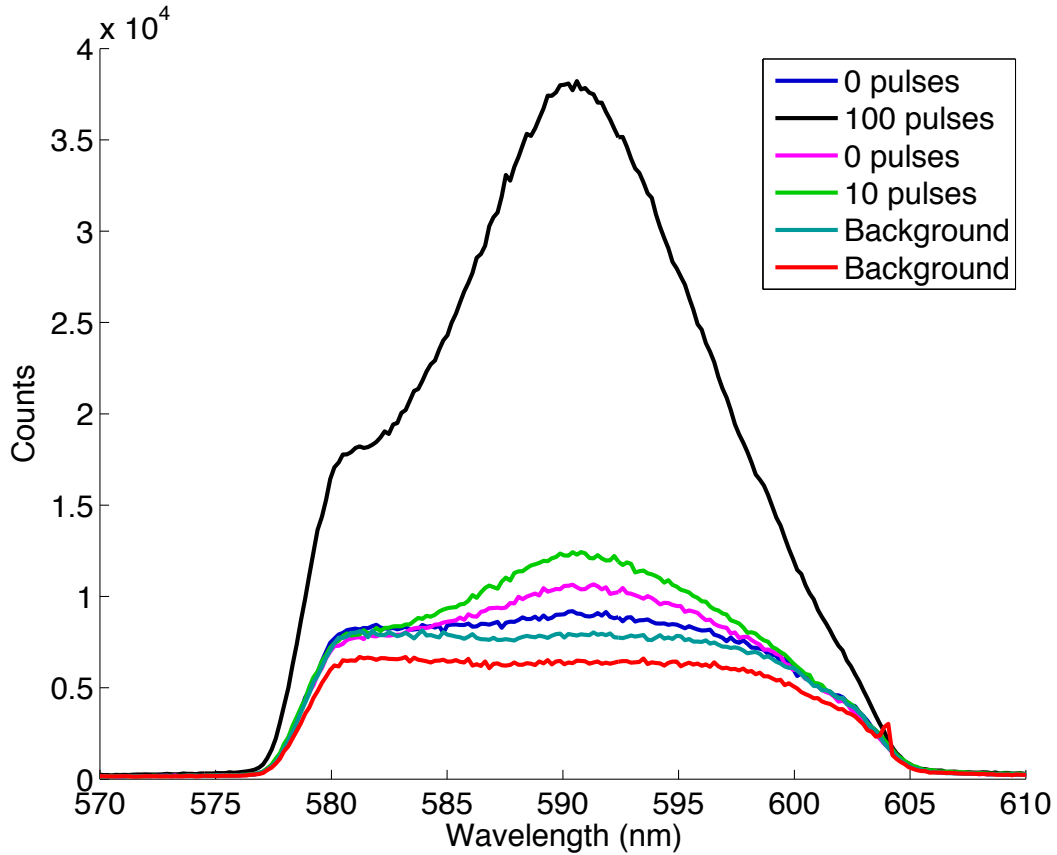


Figure 4.13: 100, 10, and 0 pulse ion beam deposits.

A neutral barium fluorescence signal of ≤ 58 atoms from 100 pulses of a 15 nA ion beam at 2000 eV without any background subtraction is shown in Figure 4.14 (blue curve), as well as zero-pulse (ion beam deflected) spectra before the ion deposit (green curve) and after the deposit (red curve). The xenon sample was melted between each one of these spectra. The two zero-pulse spectra were averaged and subtracted from the 58 atom spectrum in Figure 4.15. There is a shoulder evident at 580 nm that is not due to background. This is caused by the excitation laser being shifted off

resonance, as shown in Figure 4.5. The fluorescence efficiency for the 58 atom run was 2%.

The same procedure was followed for a run of 10 pulses at 19 nA at 2000 eV, equivalent to 7 ions landing in the laser interaction region. The 58 atom spectra from Figure 4.15 is scaled to the 10 pulse and zero pulse spectra in Figure 4.16. The average zero pulse atom number is 6 atoms through this experiment, so the scaled spectrum from Figure 4.15 is counted as 64 atoms when comparing to the spectra from Figure 4.16. This gives a number of atoms in each spectra independent of the number of pulses. Using this method, the 7 atom spectrum equates to 14 atoms. The two zero pulse deposits give 9 atoms and 3 atoms by this method. The detection of 3 neutral barium atoms is orders of magnitude better than the previous low number limit of $\approx 20,000$ atoms [76].

4.4 Imaging of Barium Atoms

Some preliminary experiments of imaging neutral barium atoms have been performed. In these experiments, two 600 nm low-pass filters were used to block the deep red fluorescence of the sapphire window, and a 561.4 nm Raman filter was used to block scattered laser light. This allowed only light in the neutral barium fluorescence wavelength region to pass to the camera. The spectrometer is an imaging spectrometer, which means the optics of the spectrometer form an image at the exit plane of the distribution of the entrance plane. In this experimental setup, the exit plane is defined by the CCD chip. The spectrometer was used with the grating in the zero order mode, acting as a flat mirror, though with reduced efficiency from first order.

Initially the laser was un-focussed, exciting with a 2 mm diameter laser spot. Figure 4.17 is a background subtracted 1000 second exposure of a deposit of 5×10^{10} Ba⁺ ions in the laser region. Each pixel is a 20 μm by 20 μm square. Because the

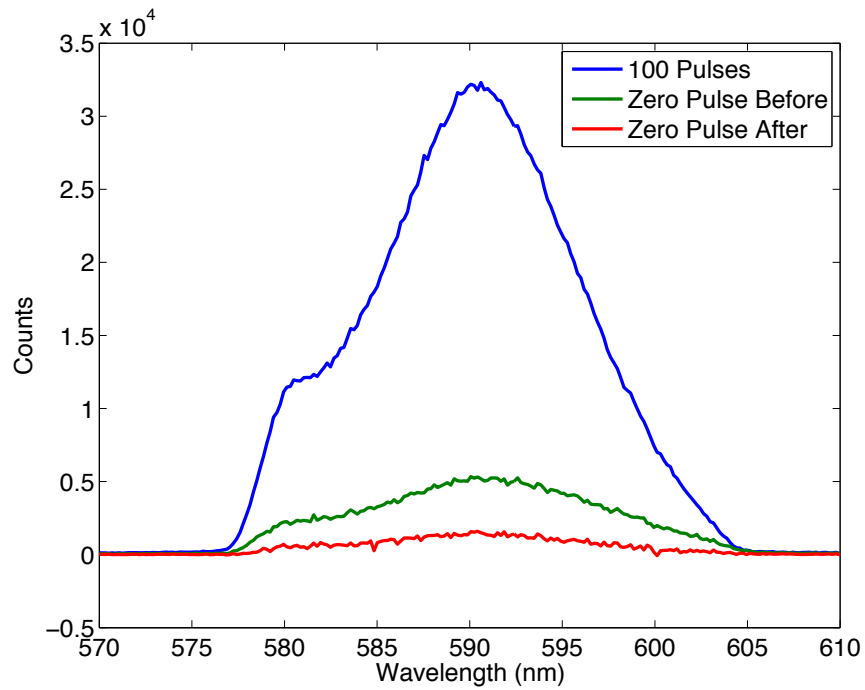


Figure 4.14: Spectrum of ≤ 58 neutral barium atoms in the laser detection region (blue curve). Zero pulse spectra before and after the deposit are shown in green and red.

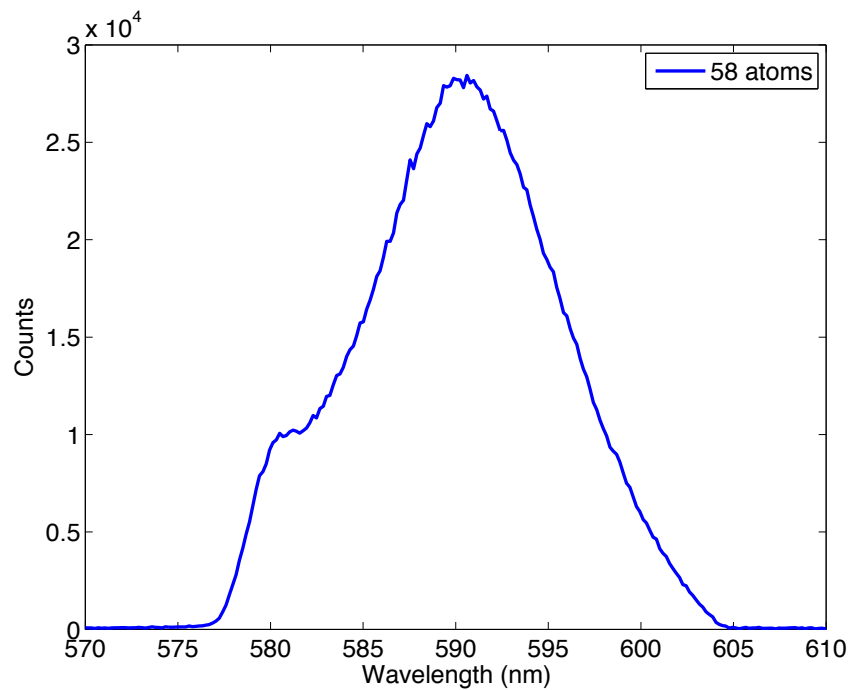


Figure 4.15: Spectrum of ≤ 58 neutral barium atoms in the laser detection region, with the average of two zero pulse spectra subtracted.

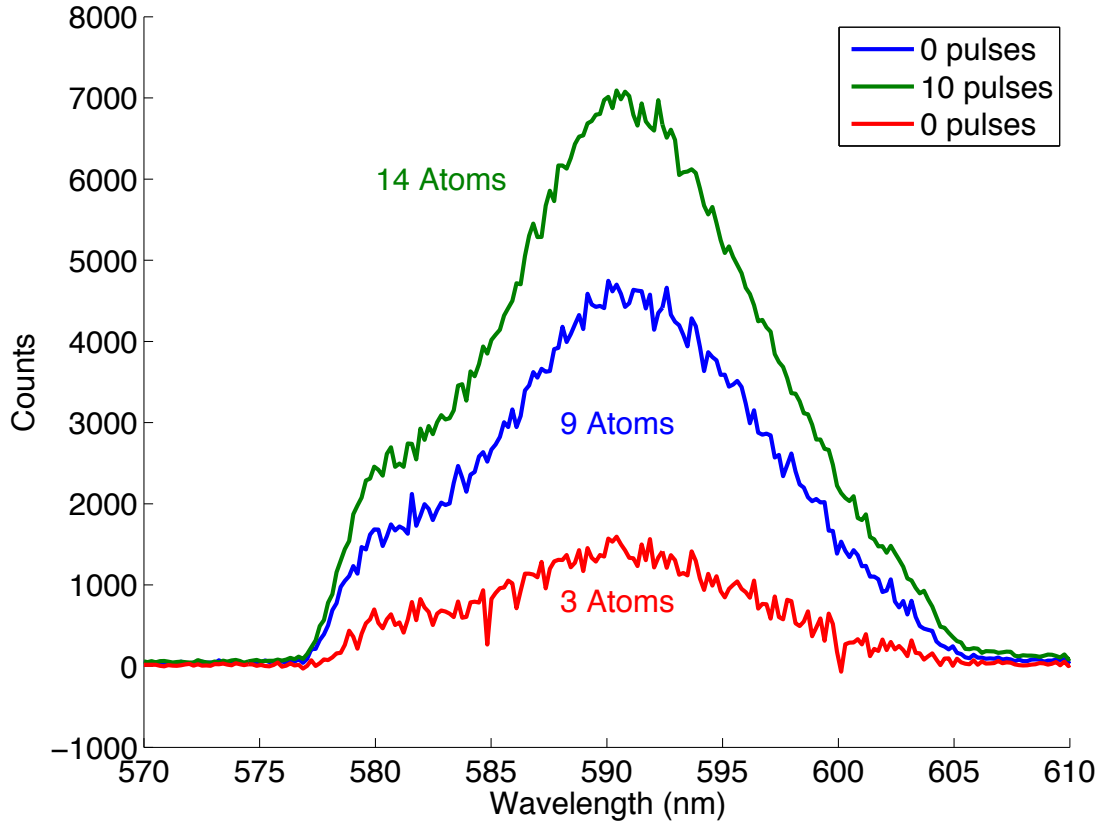


Figure 4.16: Spectra of two zero pulse deposits and one 10 pulse deposit. The numbers of atoms from scaling the 64 atom spectrum are next to each corresponding spectrum.

collection optics and spectrometer make a unit magnification on the CCD, the image is the actual size of the detection area.

A series of images of neutral barium fluorescence from a deposit of 2×10^{13} ions is shown in Figure 4.18. From the top left image to the bottom right, each plot shows an image of the fluorescence, separated by one second. There is a total decrease in signal over time of about a factor of 3 due to bleaching of the neutral barium fluorescence, in agreement with the short term bleaching factor seen in spectra.

The method of imaging fluorescence of neutral barium atoms was used for deposits of pulsed ion beams. Figure 4.19 shows a first-order image of a background-subtracted

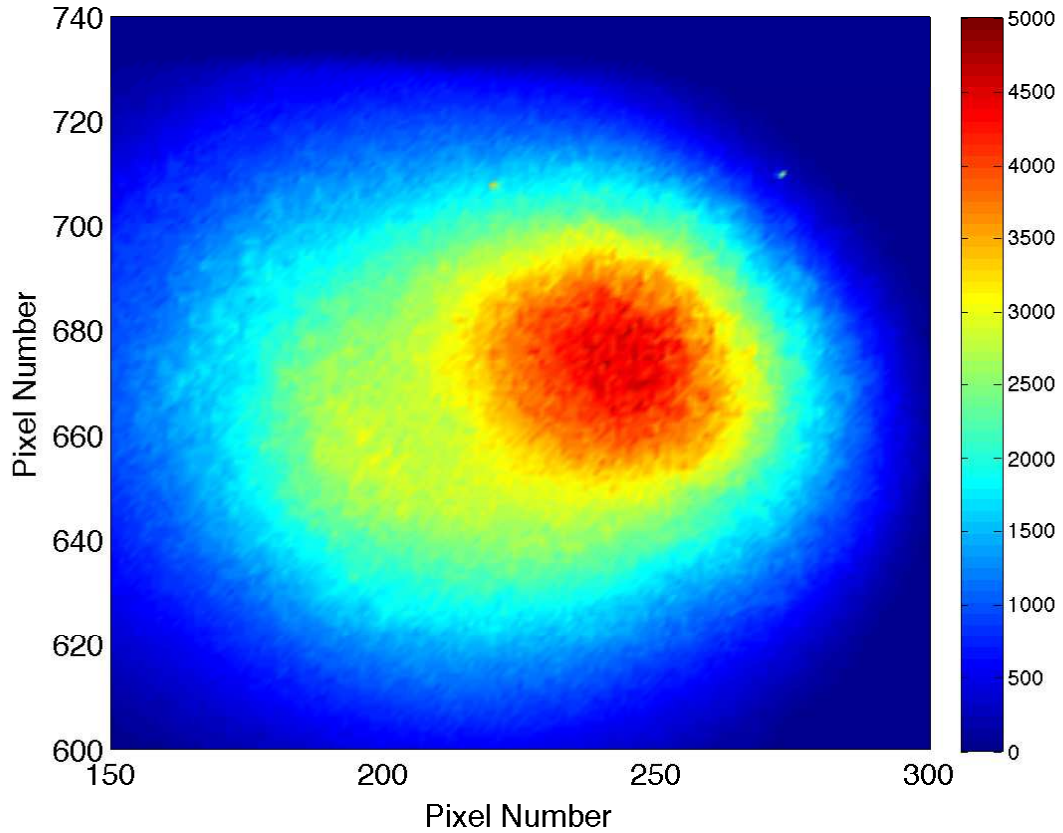


Figure 4.17: Image of the 590 nm fluorescence of neutral barium atoms after a deposit of 5×10^{10} ions.

pulsed deposit, from a deposit of 5000 ions. The image is doubled and blurry, indicating there is not a good focus of the collection optics. Some of the blurring is due to the dispersion of the grating, due to first-order imaging. With proper focusing of the optics and laser, imaging of single barium atoms should be possible in the near future.

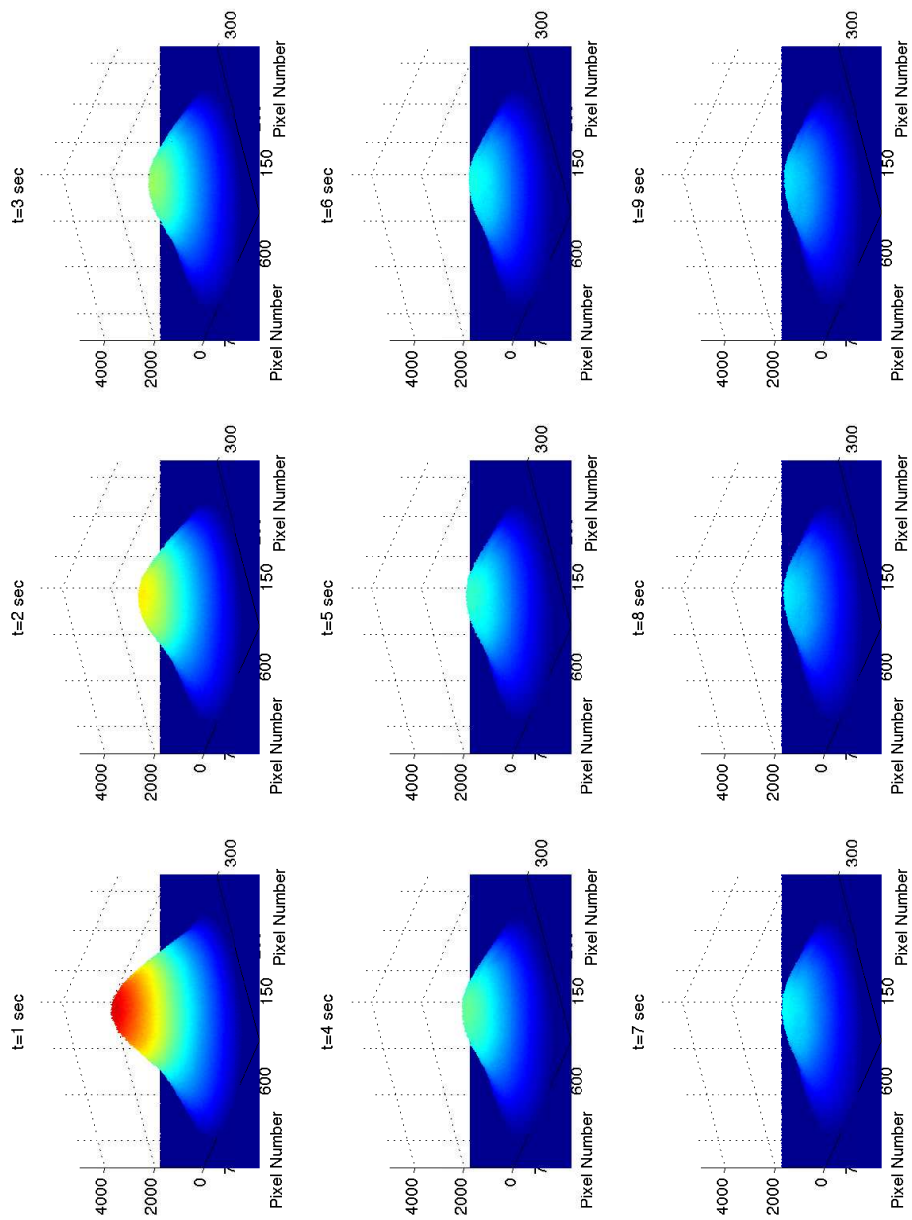


Figure 4.18: Images of neutral barium fluorescence bleaching over time.

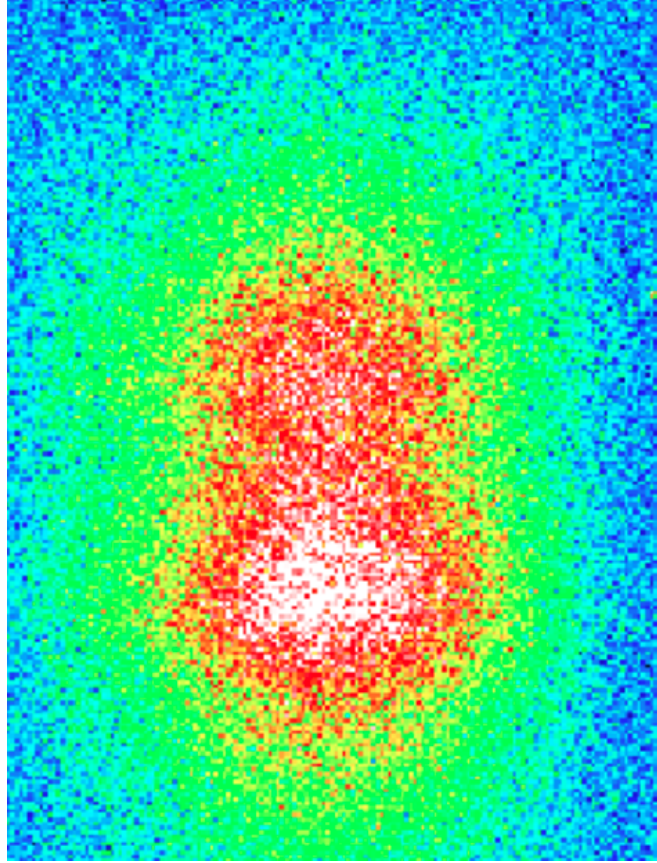


Figure 4.19: First order image of 5000 neutral barium atoms.

4.5 Emission Spectra of Ba^+ Implanted in Solid Xenon

Emission lines that are candidates for fluorescence lines of Ba^+ in solid xenon were found by comparing spectra from known neutral barium deposition to spectra from ions deposited in the matrix. These lines are merely candidates in the fact that there is a possibility that implanted ions interact with impurities in the matrix, and the emission lines observed could also be from molecules formed after implantation.

Candidate Ba^+ lines were found first by exciting the sample with the argon-ion laser lines. Background-subtracted spectra of neutral barium and barium ions taken

on the same day were compared. Peaks that were present in the ion deposition spectra that were not in the neutral spectra were attributed to species unique to the ion beam deposition, while those appearing in both were attributed to the neutral atom. Two new emission peaks at 522 nm and 575 nm were apparent when exciting with the 476.5 nm laser line.

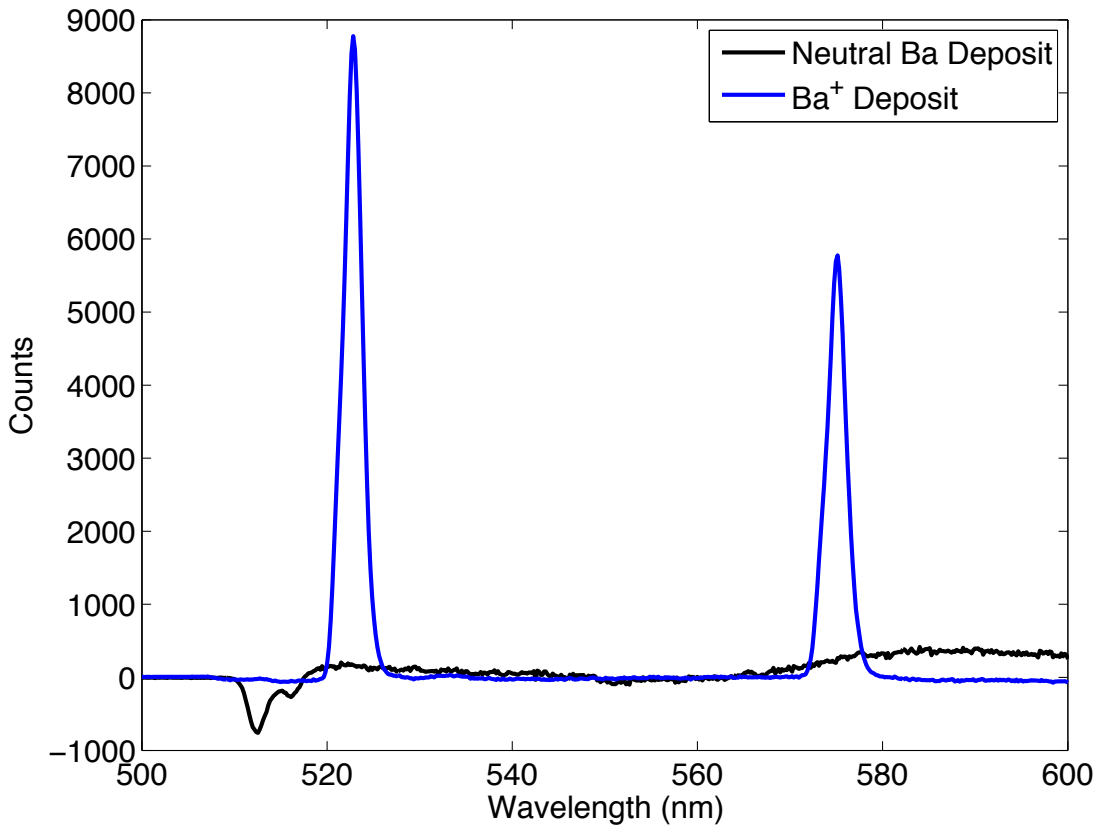


Figure 4.20: Emission spectra of Ba^+ and Ba^0 , excited by 478.5 nm laser light. Note the 522 nm and 575 nm lines found in the ion spectrum are absent in the neutral spectrum. The broad peak around 590 nm in the neutral spectra is from far-off resonance excitation of a large number of neutral atoms. Negative values on the left are the result of imperfect background subtraction.

After establishing that these lines attributed to ion implantation were more favorably excited by the 476.5 nm line, a blue dye laser was used to find the optimum

wavelength of excitation. With 478.5 nm excitation light, the sharper candidate Ba⁺ ion emission peaks stood out very clearly from the broader neutral barium peaks, as seen in Figure 4.20. Due to the ions being excited approximately an order of magnitude more efficiently with the on-resonance laser, three additional lines associated with barium ions being implanted in the matrix were found. These additional lines are at 637 nm, 712 nm, and 814 nm, as shown in Figures 4.21 and 4.22. These three lines are significantly smaller than the 522 nm and 575 nm line. The 637 nm line is approximately 14% the size of the 522 nm peak, and the 712 nm and 814 nm peaks are approximately 1.7% and 0.1% the size of the 522 nm peak. Each ion emission peak has a full-width, half-max value on the order of 4 nm. This is significantly smaller than that of the 590 nm fluorescence line of neutral barium (≈ 30 nm) [76]. Because the 712 nm and 814 nm lines lie in the midst of a large amount of background fluorescence from the sapphire window, care was needed to make proper background subtractions. The slope under the 712 nm peak in Figure 4.22 is due to imperfect background subtraction.

4.6 Excitation Spectra of Candidate Ba⁺ Emission Lines

Excitation spectra for all five candidate Ba⁺ emission lines are shown in Figures 4.23 and 4.24. Excitation spectra for all of the peaks are identical, varying only in size. In all cases, the maximum emission signal occurs when the sample is excited with 478.5 nm laser light. As an aid to see the similarity in excitation spectra, the 712 nm excitation curve in Figure 4.24 has been scaled to the same size as the 814 nm excitation curve, which has been smoothed. These spectra have a full-width at half-maximum (FWHM) of approximately 1 nm. This width is much smaller than the width of the absorption spectrum of neutral barium in solid xenon, that has a

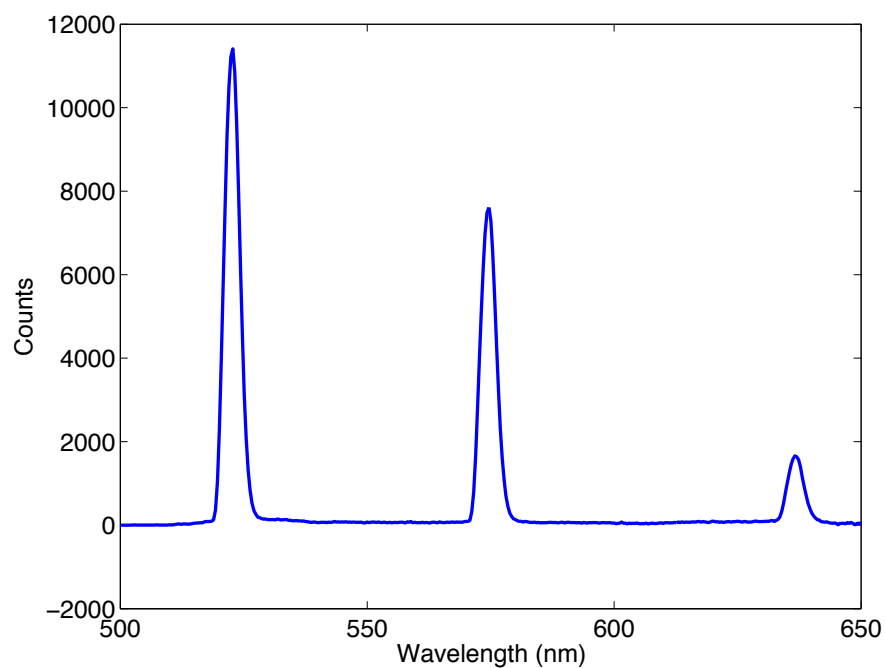


Figure 4.21: Emission spectrum of Ba⁺ implanted in SXe, showing the 522 nm, 575 nm, and 637 nm lines, with 478.5 nm excitation.

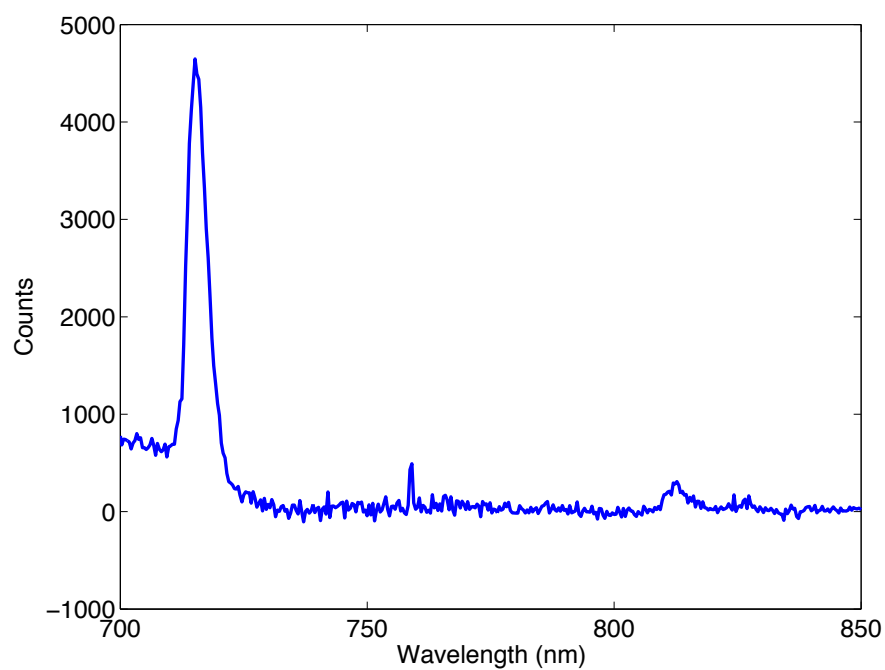


Figure 4.22: Emission spectrum of the two smallest Ba⁺ emission peaks at 712 nm and 814 nm, excited with 478.5 nm laser light.

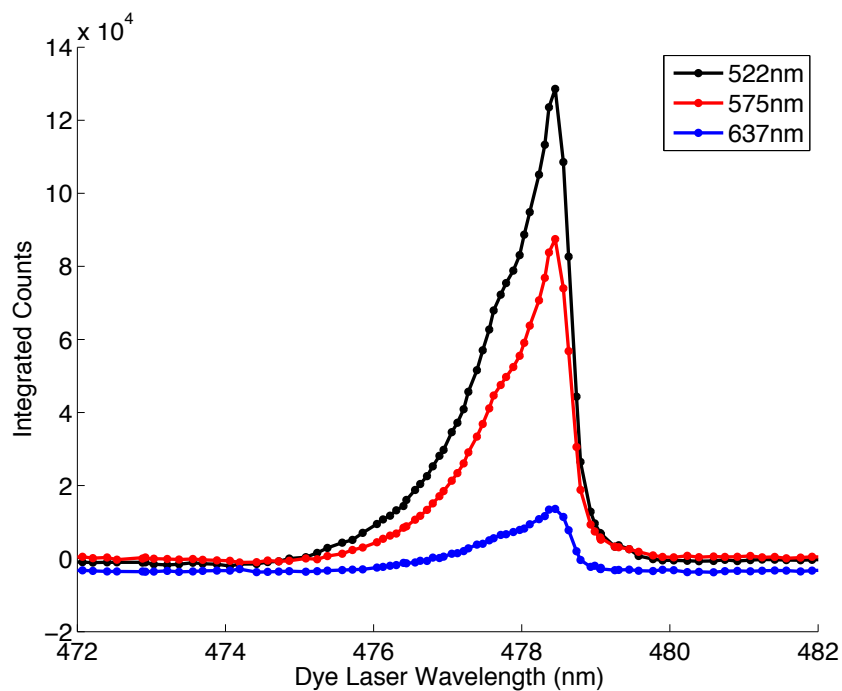


Figure 4.23: Excitation spectra of the 522 nm, 575 nm and 637 nm emission peaks.

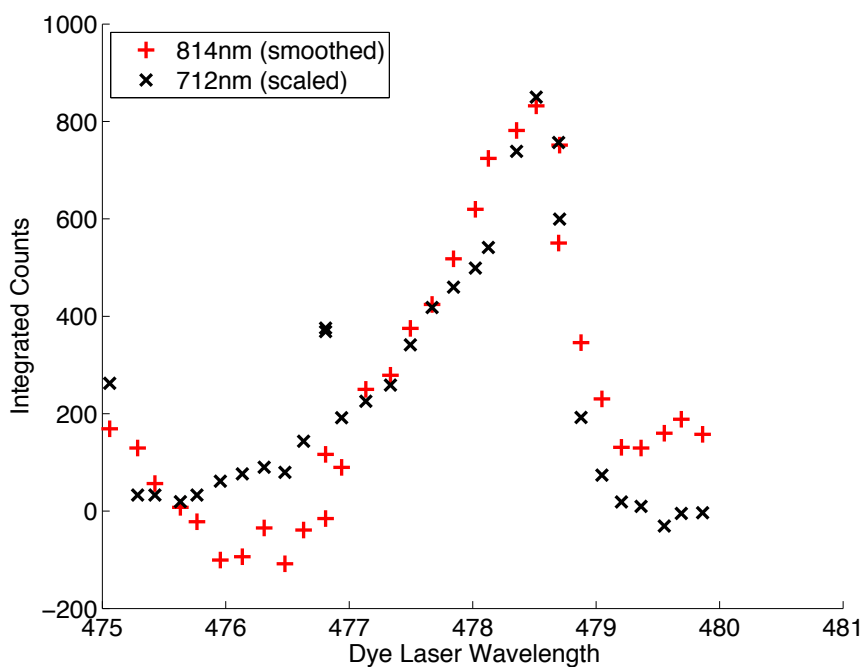


Figure 4.24: Excitation spectra of the 712 nm and 814 nm emission peaks. The 814 nm spectrum has been smoothed for sake of making identification easier, while the 712 nm spectrum has been scaled to the size of the 814 nm spectrum for ease of reference.

FWHM of 30 nm [76]. It is also very asymmetric, and has evidence of a bump on the blue side of the peak and a tail to the blue side. The sum of three Gaussian curves with peaks at 477.4 nm, 478 nm, and 478.5 nm gives a good fit to the excitation spectrum, as seen in Figure 4.25.

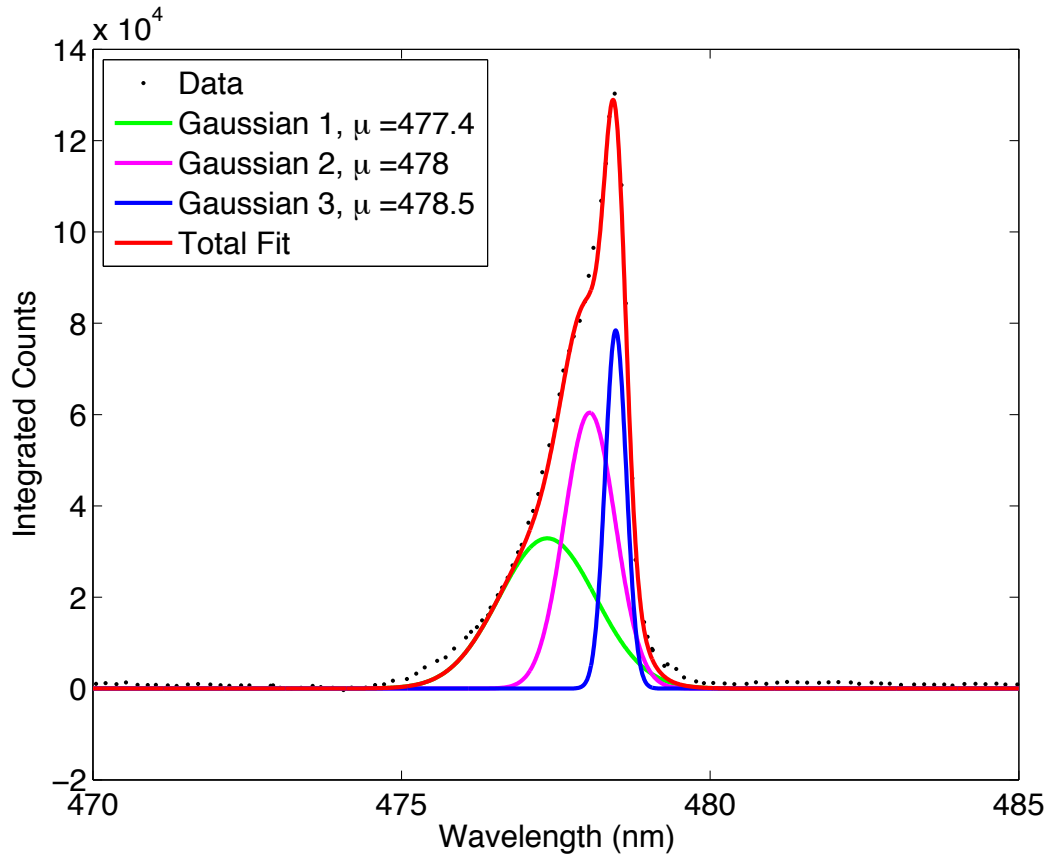


Figure 4.25: Excitation spectrum of the 522 nm fluorescence peak, with three gaussian curves fit to it, showing three distinct peaks. The μ values listed in the legend indicate the center wavelength of the corresponding gaussian curve.

4.7 Interpretation of Excitation and Emission Lines of Ba⁺

A plausible assignment of the six observed transitions to barium ion transitions between matrix perturbed states corresponding to the vacuum energy levels of Ba⁺ is given in Figure 4.26. The 478.5 nm excitation line and the 522 nm emission line are both attributed to the 6p ²P_{3/2} to 6s ²S_{1/2} transition. The 575 nm emission line comes from the 6p ²P_{1/2} to 6s ²S_{1/2} transition. The appearance of the 6p ²P_{1/2} → 6s ²S_{1/2} emission line when exciting the 6p ²S_{1/2} → 6s ²P_{3/2} transition requires a significant amount of population transfer from the ²P_{3/2} to the ²P_{1/2} state in the matrix. From the 6p ²P_{3/2} state, the 637 nm and the 712 nm emission lines correspond to the decays to the 5d ²D_{3/2} and 5d ²D_{5/2} states. Lastly, the 814 nm emission line is assigned to the decay of the 6p ²P_{1/2} state to the 5d ²D_{3/2} state. These assignments and the corresponding red-shifts are listed in Table 4.2. The red shifts are of the same order of magnitude, but vary significantly. It is expected that the fluorescence of an atom or ion will be red shifted more than the excitation in a noble gas matrix. The 522 nm emission line is significantly shifted from the excitation of same state, in agreement with this expectation. Though an additional excitation line exciting the 6s ²S_{1/2} → 6p ²P_{1/2} is expected with this interpretation, it was not found through the use of the two available dye laser with excitation wavelengths of 465 nm to 515 nm and 540 nm to 570 nm. However, based on the red shift of the 478.5 nm excitation line, it might be expected to lie in the range of the wavelengths not tested.

The wavelengths and wave numbers of the six lines resulting from implanting Ba⁺ in solid xenon are given in Table 4.3. The difference in wavenumber of each successive peak is listed in the third column. These differences have an average value of 1723 cm⁻¹ with a standard deviation of 48 cm⁻¹. The somewhat even spacing of these lines is reminiscent of vibronic lines in a molecule. The even spacing is shown in

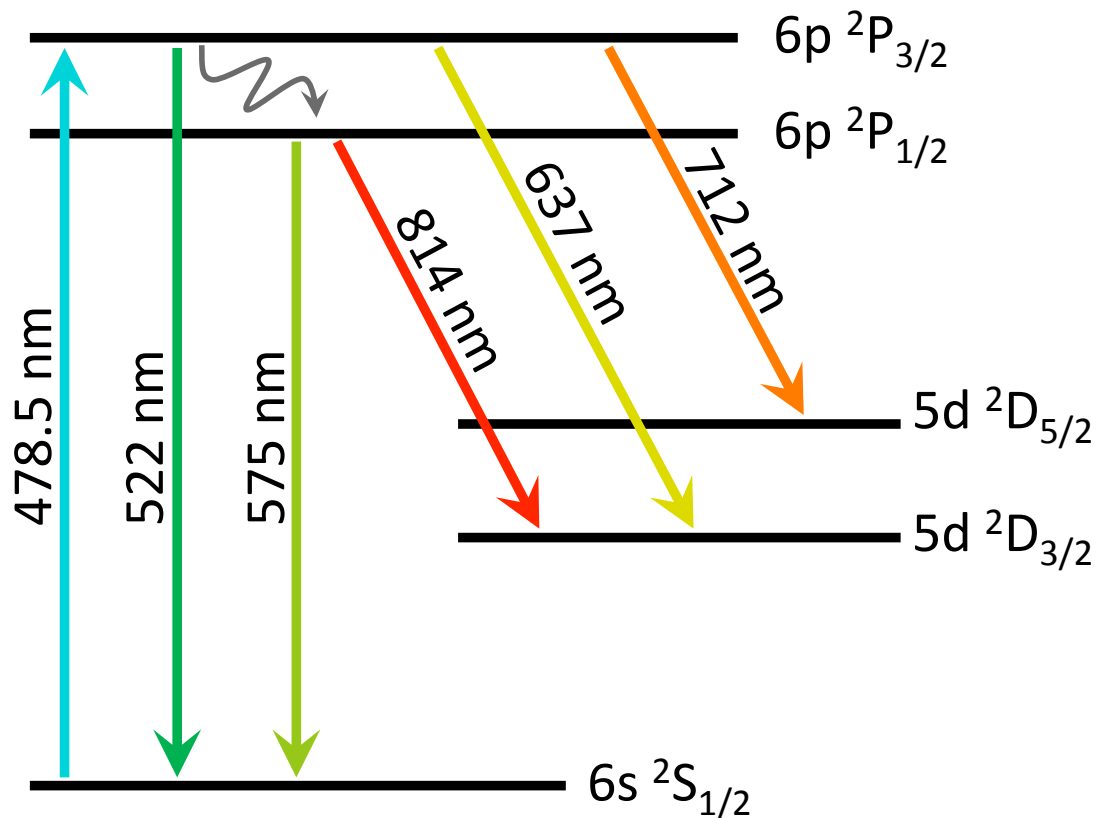


Figure 4.26: A possible interpretation of the energy level diagram of Ba^+ in solid xenon. The excitation line is red shifted, and the emission lines have a greater red shift.

Figure 4.27. This suggests another interpretation. In this model, the excitation from the $\nu'' = 0$ level of the ground state goes to the $\nu' = 0$ vibrational level of the excited state and then the decay occurs to the $\nu'' = 1 - 5$ vibrational energy levels of the ground state, as shown in Figure 4.28.

An anharmonic oscillator has line spacings that decrease at higher vibrational energy levels. This is given by the anharmonic oscillator equation:

$$E(\nu) = \omega_e(\nu + \frac{1}{2}) - \omega_e x_e (\nu + \frac{1}{2})^2 + \text{higher order terms}$$

where x_e is an anharmonicity constant, ω_e is the vibrational frequency, and ν is the

Table 4.2: Summary of assignment of Ba⁺ vacuum energy levels to Ba⁺ in solid xenon with corresponding red-shifts.

Transition	Vacuum	SXe	$\Delta\nu$ (cm ⁻¹)
	Wavenumber (cm ⁻¹)	Wavenumber (cm ⁻¹)	
6s ² S _{1/2} → 6p ² P _{3/2}	21959	20898	1061
6p ² P _{3/2} → 6s ² S _{1/2}	21959	19157	2802
6p ² P _{1/2} → 6s ² S _{1/2}	20267	17391	2876
6p ² P _{3/2} → 5d ² D _{3/2}	17142	15689	1453
6p ² P _{3/2} → 5d ² D _{5/2}	16282	14044	2238
6p ² P _{1/2} → 5d ² D _{3/2}	15392	12285	3107

vibrational level number. The first four line spacings of Ba⁺ implanted in solid xenon roughly agree with this model. The final spacing, that of the 712 nm to 814 nm peak, does not. This detracts from the strength of this model.

Ba⁺Xe, Ba⁺H₂O, Ba⁺N₂, and Ba⁺O are the molecules most likely to form with Ba⁺ ions in landing on the matrix and binding with impurity molecules. No vibration frequencies for these most likely candidates have been found in available literature, with the exception of a theoretical Ba⁺Xe calculation [52]. More complicated reactions could produce other possible molecular species, such as the ones listed in Table 4.4. Though several barium-containing molecules have Ba-H based vibrations in the 1100 cm⁻¹ range, no molecule has yet been found that is even close to matching the 1723 cm⁻¹ spacing of the barium ions implanted in solid xenon. Using the 1723 cm⁻¹ spacing, the 0 – 6 and 0 – 7 emission lines are expected at approximately 947 nm and 1131 nm. From the trend observed, these would be exceptionally small compared to the known lines. Attempts were made to observe these transitions to no avail.

Table 4.3: Emission and excitation lines of Ba⁺ implanted in SXe.

Peak Wavelength (nm)	Peak Wavenumber (cm ⁻¹)	$\Delta\tilde{\nu}$	$\nu' - \nu''$
478.5	20898	-	0 - 0
522	19157	1741	0 - 1
575	17391	1766	0 - 2
637	15689	1702	0 - 3
712	14044	1645	0 - 4
814	12285	1759	0 - 5

Table 4.4: Summary of vibration fundamentals for possible molecules in the system, along with the material or phase the molecule was in. Theoretical calculations are marked as (th) in the Vibration Frequency column.

Molecule	Vibration Frequency ω_e (cm ⁻¹)	Phase	REF
Ba ⁺ Xe	52.3 (th)	gas	[52]
Ba ₂	35 (th)	gas	[79]
BaO ₂	541	SN ₂	[80]
BaO	665.8	gas	[81]
BaO	634.2	SAr	[81]
BaH	1168.4	gas	[82]
BaH ⁺	1370 (th)	gas	[83]
BaH ₂	1131.3	SNe	[84]
BaH ₂	1128.6	SAr	[84]
BaOH	492.4	gas	[85]

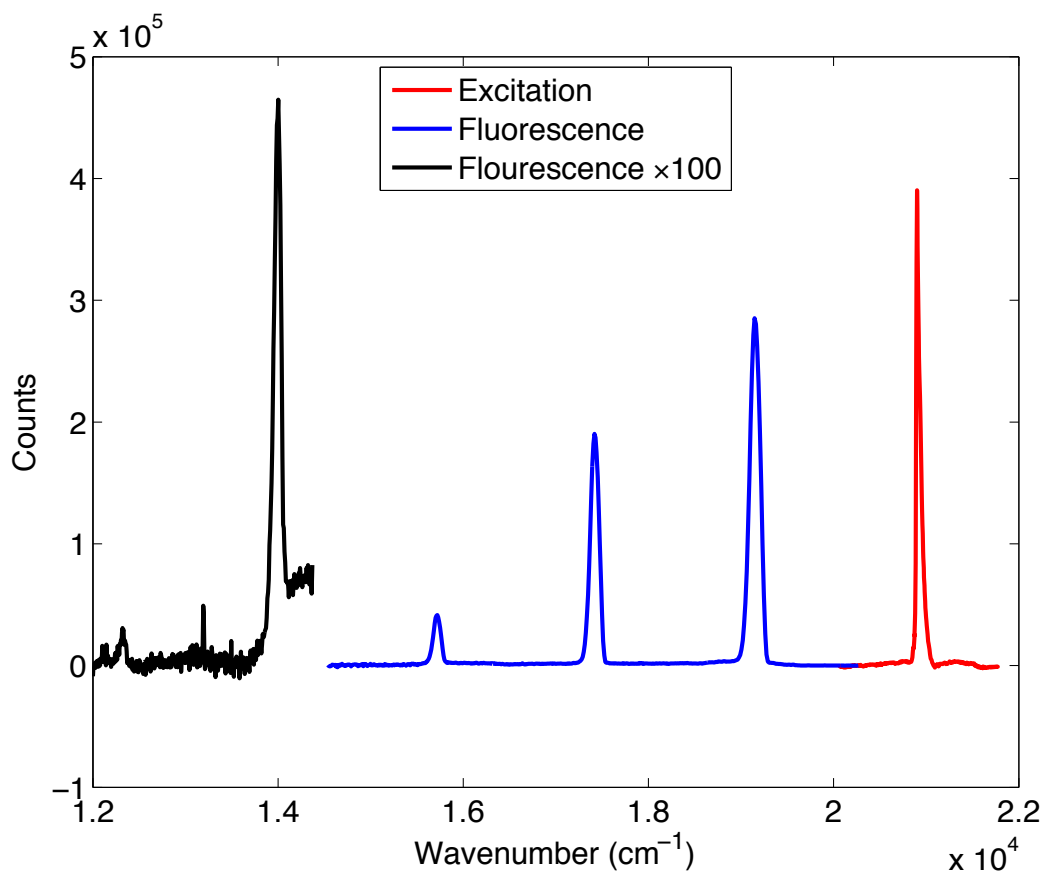


Figure 4.27: Emission and excitation lines of Ba⁺ in SXe. The excitation spectrum is in red, the large fluorescence lines are in blue, and the small fluorescence lines in black are scaled up by a factor of 100.

4.8 Bleaching and Saturation Studies of Ba⁺

To test for the possibility of optical pumping and bleaching of Ba⁺ implanted in solid xenon, the emission signals were monitored over time. Figure 4.29 shows the integrated emission peak counts in 0.2 second intervals over 200 seconds. Ions were deposited on the sample prior to being exposed to laser light. At 1 second in Figure 4.29, laser light was exposed to the sample. Though there was a slight decrease in the integrated counts in the first 10 seconds of exposure, there was no subsequent change in signal strength to 200 seconds. Ions implanted at the beginning of an experiment

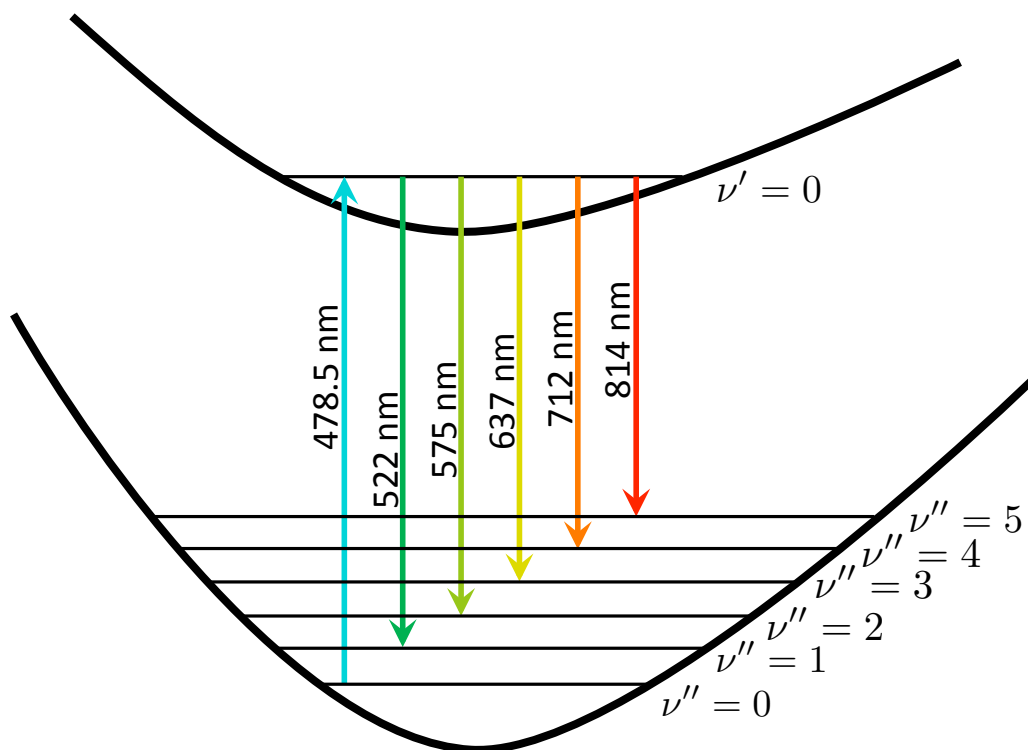


Figure 4.28: A possible assignment of the excitation and emission lines to vibrational energy levels in a molecule.

were found to still show the same emission signal later in the day, even after multiple hours. This indicates negligible bleaching of these lines due to slow processes, such as chemical reactions.

The strength of the 522 nm emission line as a function of pumping rate w_{12} is shown in Figure 4.30. For the Ba^+ model, a single ion excitation rate w_{12} can be calculated as

$$w_{12} = I \frac{\sigma}{h\nu}$$

where σ is the absorption cross section. By using the excitation spectrum discovered for Ba^+ in solid xenon, the peak cross section was calculated to be $2.15 \times 10^{-14} \text{ cm}^2$ using the A_{21} value for Ba^+ in vacuum by using the method described in Section 2.6.

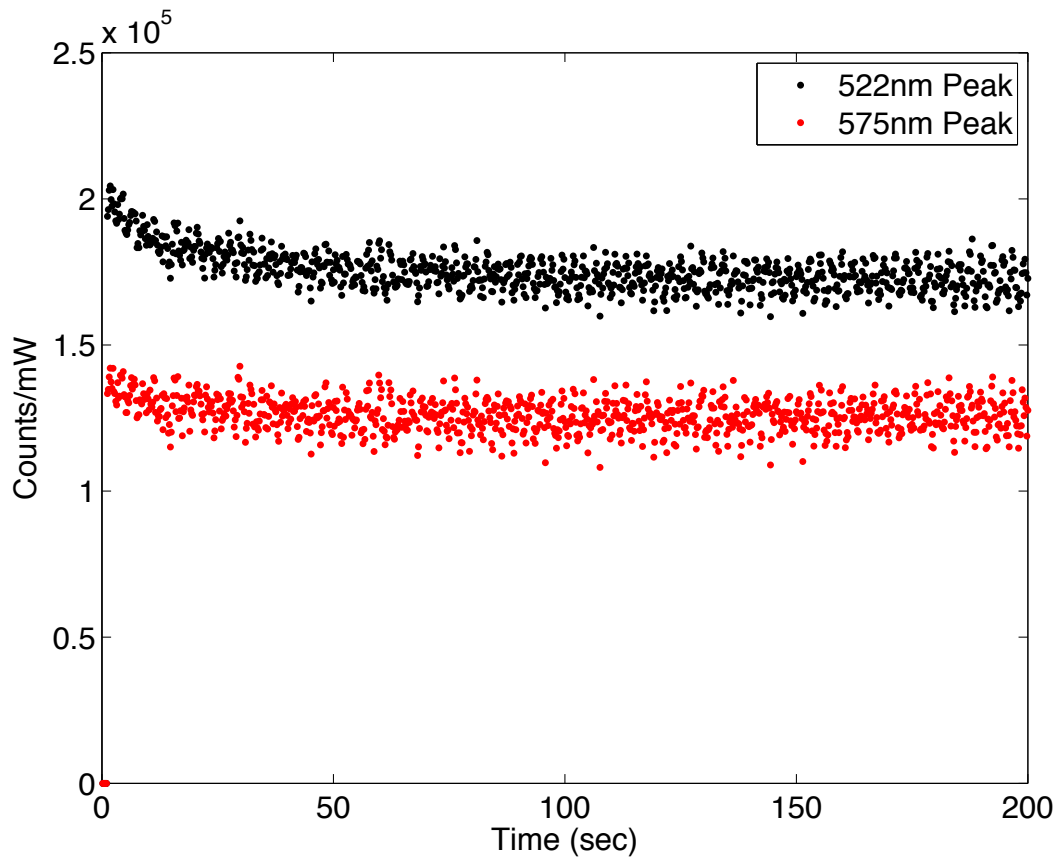


Figure 4.29: Integrated counts versus time for the 522 nm and 575 nm emission peaks after the sample is exposed to laser light of $w_{12} = 1 \times 10^7 \text{ s}^{-1}$ after five frames of no laser light.

A curve showing the cross section over the excitation wavelength range is shown in Figure 4.31.

After a deposit of barium ions was made, the laser power was varied by way of neutral density filters and by changing the krypton laser pumping power. For each laser power change, a fluorescence spectrum was taken and was verified to not exhibit bleaching. By working from low power to high power, any possible effect of bleaching was minimized. As shown in Figure 4.30, the integrated counts of the 522 nm emission peak rises linearly with laser intensity. By modeling the barium ion in solid xenon as a three level system and using known transition rates, it is possible to obtain a limit

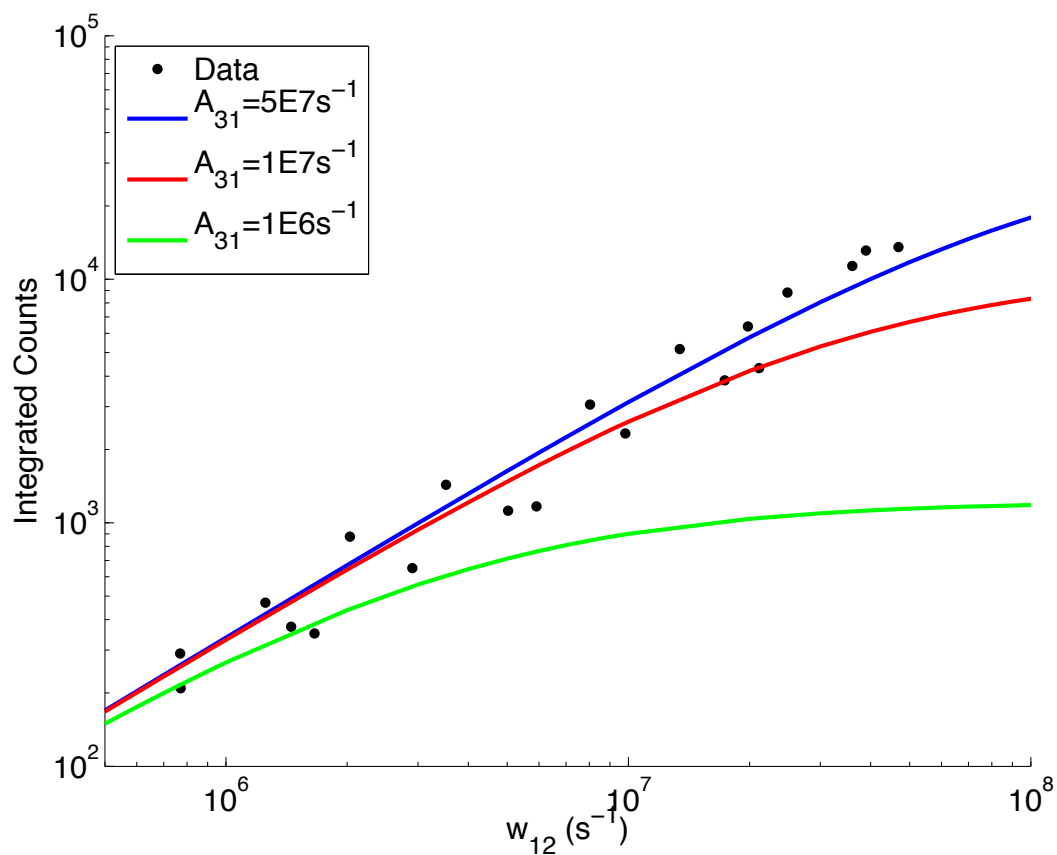


Figure 4.30: Plot of summed 522 nm emission peak counts versus w_{12} , exciting with 478.4 nm laser light. Emission increases linearly, even at high pumping rates.

on the value for the metastable decay rate A_{31} using Equation 2.4. Several possible values of A_{31} are shown in Figure 4.30. From the fact that the red curve falls below the experimental data at the highest intensity, a value of $A_{31} \geq 1 \times 10^7$ is extracted. This is at least nine orders of magnitude higher than the metastable decay rate in vacuum.

The integrated counts of the emission peak are also linear at constant laser power in the number of ions deposited at all deposit energies, as shown in Figure 4.32. This is surprising because one might expect the matrix to charge up due to the deposited ions and eventually repel subsequent ions. If the xenon matrix and barium ions are

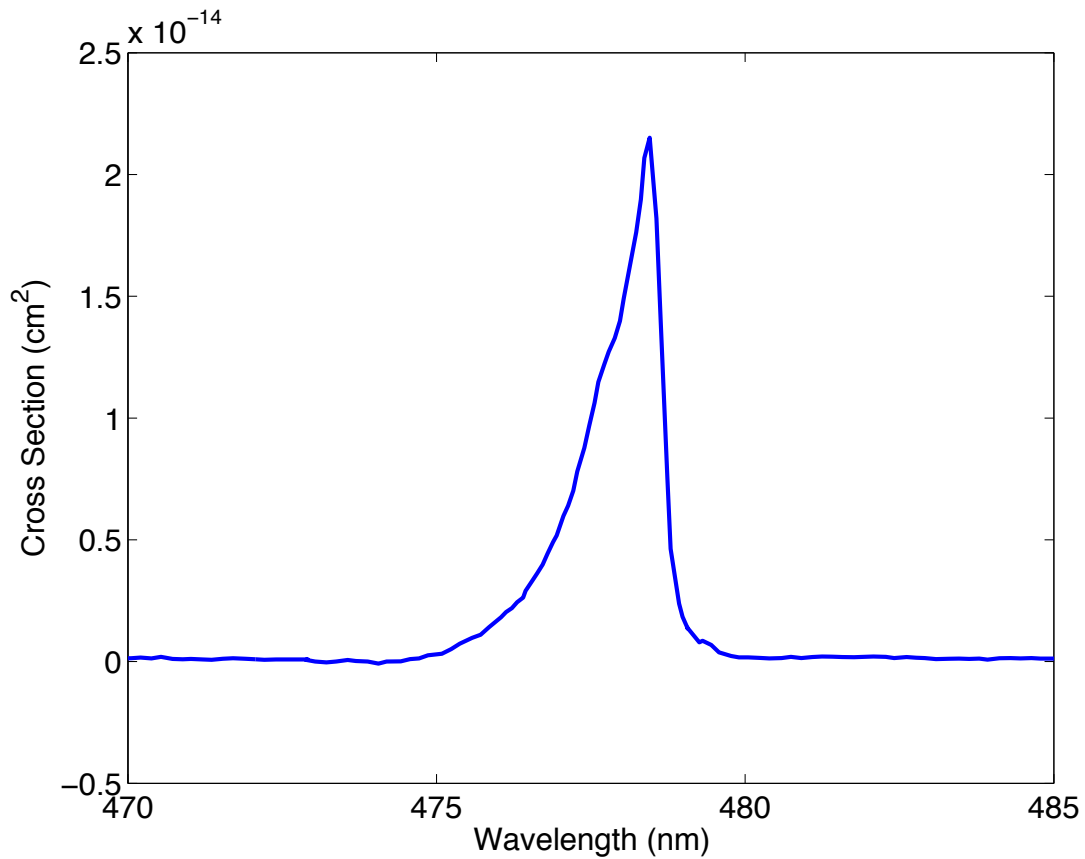


Figure 4.31: Cross section of Ba^+ ions in solid xenon. Peak value occurs at $2.15 \times 10^{-14} \text{ cm}^{-2}$ at peak wavelength of 478.5 nm.

modeled as a uniformly charged disk of charge Q and radius R , the electric potential at the center relative to infinity may be approximated as

$$V = \frac{Q}{2\epsilon_0\pi R}$$

At the highest point on Figure 4.32, 7×10^9 ions have been deposited in the laser region. This equates to a 28 kV potential. This would deflect many of the ions landing on the sample, and the integrated counts would not respond linearly to ions deposited. As the relationship is linear to very high numbers of ions deposited, many of those ions must neutralize on landing and electrons must flow from the copper

window holder in order to prevent the deflection of the beam.

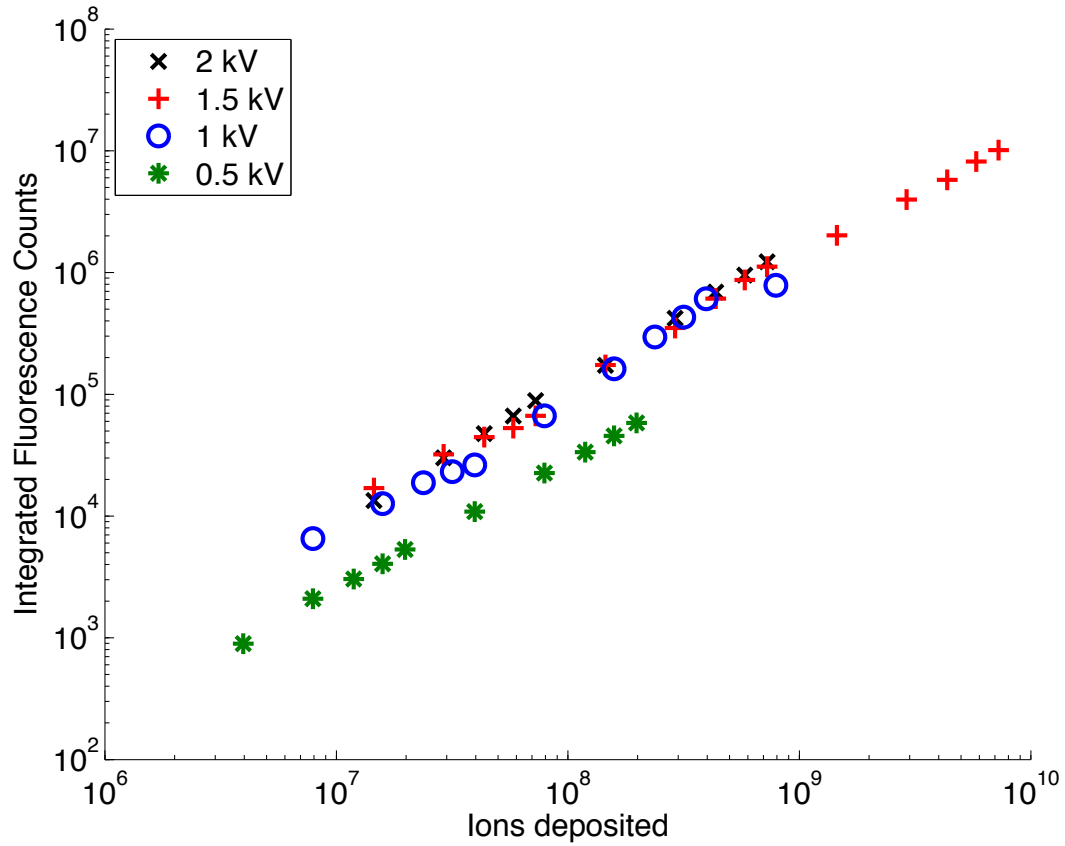


Figure 4.32: Fluorescence counts of 575 nm peak versus deposited ions for a variety of landing energies.

The candidate barium ion fluorescence efficiency cannot be calculated because the number of ions N is not known. If it is assumed that the number of ions is simply equal to the number deposited, the fluorescence efficiency derived ranges from 10^{-7} to 10^{-5} . This barium ion fluorescence efficiency is much lower than the fluorescence efficiency of 22% observed for neutral barium atoms in solid xenon.

The temperature dependence of the strength of the 522 nm line is shown in Figure 4.33. After depositing Ba^+ ions at 10 K, the sample was warmed to 15 K and then cooled. This process was then repeated for successively higher temperatures. Temper-

atures up to 35 K featured almost no reversible or irreversible loss in signal. Above 35 K, to the sublimation point of the sample, around 75 K, there was irreversible loss as the temperature increased. This differs from the temperature dependence of the strength of the 590 nm neutral barium fluorescence peak, which decreased dramatically below the sublimation point at 45 K. A possible reason for a permanent loss of fluorescence at higher temperatures are increased mobility of the Ba^+ ions, which could result in the formation of a non-fluorescing molecule with an impurity atom. Alternatively, impurity atoms or molecules could be more mobile at higher temperatures and travel to Ba^+ ions to form a non-fluorescing molecule.

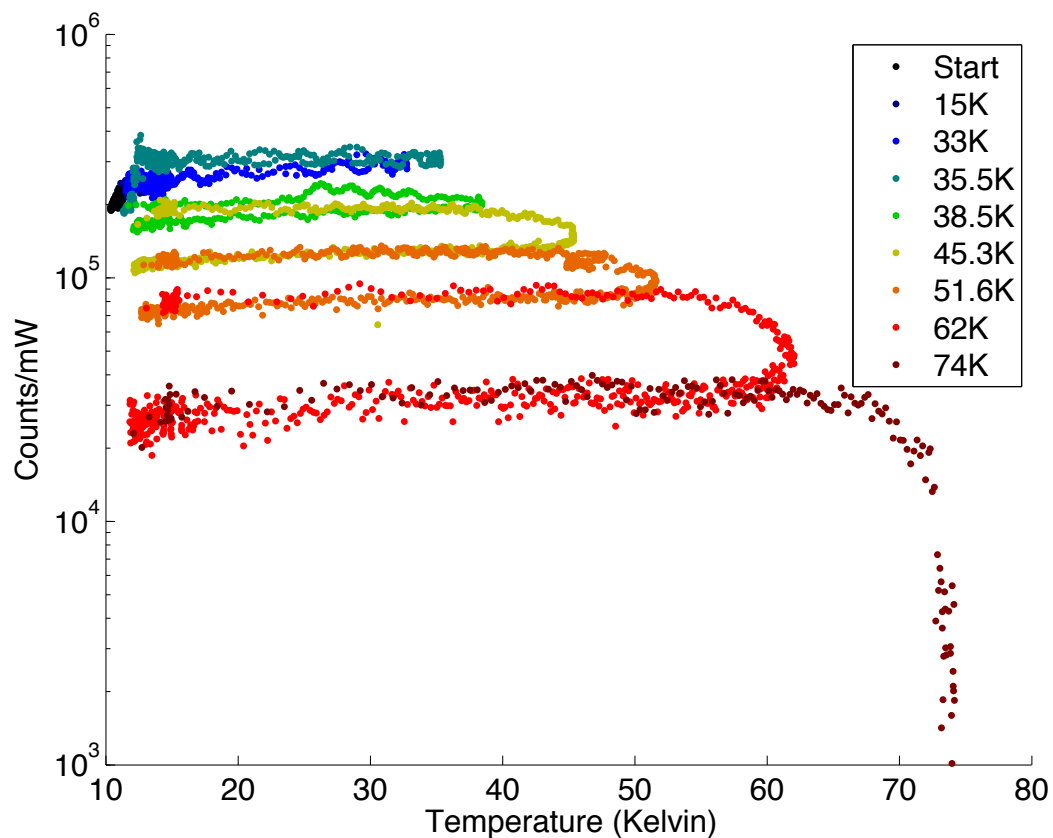


Figure 4.33: Temperature dependence of integrated 522 nm fluorescence, normalized to laser power during anneal cycles to various temperatures. Temperature values in the legend indicate the maximum temperature reached during that particular anneal cycle.

5 Conclusion

5.1 Summary

A method for tagging individual barium daughter atoms in solid xenon is desired for the Enriched Xenon Observatory in order to eliminate all background events. Pioneering work in Ba and Ba⁺ spectroscopy in solid xenon is presented in this thesis, leading to a demonstration of the detection of a small number of neutral barium atoms in solid xenon. A fluorescence spectrum of 3 neutral barium atoms is presented here for the first time. Detecting 7 atoms is a large improvement over the previous low number detection of 20,000 atoms. A significant improvement in fluorescence efficiency is also presented in this work. Prior to these experiments, the highest fluorescence efficiency achieved was about 0.1%. After increasing the xenon flow rate onto the cryostat window, leading to an expected improvement in the solid xenon purity, a fluorescence efficiency of 22% was achieved. This fluorescence efficiency is quite large, of the same order as dye molecules, which have been detected on the single molecule level for several decades. Thus it is expected that detecting single barium atoms in solid xenon can become as routine as single molecule detection and imaging is now. Data from preliminary experiments of imaging barium atom deposits with the neutral barium fluorescence show promise for single atom imaging in the near future. In future experiments, higher excitation intensities, along with higher collection efficiencies by imaging directly onto the CCD rather than at zero order through the spectrometer, will make the single atom signal even larger and will reduce the time for an image or spectrum. By adjusting the collection optics to magnify the imaged spot size on the CCD, it might be possible to map out an image of the barium ion fluorescence on the solid xenon matrix, and detect single atoms in this fashion.

Table 5.1: Comparison of numbers for the current low atom limit versus single atom detection.

Case	ϵ_F	ϵ_{det}	Laser Power	Laser Area	Counts/sec
3 atoms	1%	6.7×10^{-4}	2 mW	$32 \mu\text{m}^2$	114
1 atom	7%	20%	5 mW	$10 \mu\text{m}^2$	2.2×10^6

The parameters of the 3 atom atom detection experiment with an assumed fluorescence efficiency of 1% are compared with those of a future single atom experiment in Table 5.1. Several key improvements can be implemented for the single atom case. First, the high fluorescence efficiency of 7% is used (reduced by a factor of three from 22% due to bleaching in long exposures). The laser area is decreased using a shorter microscope objective for focusing the laser. Detection efficiency can be increased by two orders of magnitude. This could be achieved by switching to confocal microscopy modes with high collection efficiency, bypassing the spectrometer, which has several losses. Integrating all counts on the CCD also reduces readout noise. In this manner, the detected count rate from a single atom is 2.2×10^6 counts per second. Thus single atom detection is definitely feasible. Images of molecules in solid xenon matrices have been obtained with clear distinction from background [86].

Results from experiments implanting Ba^+ ions in solid xenon are reported for the first time in this thesis. One new excitation line was found to produce five new emission lines. There is a reasonable correlation between the number and wavelengths of the lines observed with known Ba^+ transitions in vacuum. The somewhat even line spacing also suggests a molecular interpretation, possibly a molecule containing Ba or Ba^+ and H. However, no known molecule with a vibrational frequency close that of the observed emission lines and that might exist in the system has been found. The observed fluorescence signal is proportional to the Ba^+ charge deposited and

laser power over several orders of magnitude. There is very little optical pumping or bleaching of these emission lines. Though barium ions implanted in the solid xenon matrix were so far found to have a much lower effective fluorescence efficiency, the value is artificially low to due to a high neutralization percentage on landing in the xenon matrix.

5.2 Future Work

To reliably implant single Ba^+ ions in solid xenon rather than depositing many ions through the ion beam used in this thesis, a radionuclide-driven single ion source [87] could be employed. In such a source, the detection of the α particle in the substrate detector shows when a recoil occurs, which knocks a Ba^+ ion off some percentage of the time. This would supply a way of counting smaller numbers of Ba^+ ions deposited in the solid xenon. This source has already been shown to work in vacuum, and is perfectly suited to this phase of the EXO tagging effort.

In order to model an EXO Full liquid xenon experiment with barium tagging in solid xenon, the next phases of the tagging effort at CSU will attempt to grab a daughter barium ion on a tip. A liquid xenon cell has already been used for studies of Ba^+ fluorescence in liquid xenon. It could be adapted for studies of grabbing in liquid xenon when using a cryo-cooled probe. A different source of Ba^+ ions will be required for tagging in liquid xenon, since there would not be sufficient recoil to get the Ba^+ into the liquid xenon with the radionuclide driven source. Such sources might use the fission of a californium isotope, of which barium is a byproduct.

REFERENCES

- [1] J. Chadwick, *Intensitätsverteilung im magnetischen Spektrum der β -Strahlen von Radium B+ C*. Druck von Friedr. Vieweg und Sohn, 1914.
- [2] W. Pauli, “Rapports du Septieme Conseil de Physique Solvay,” *Brussels (Gauthier Villars, Paris, 1934)*, 1933.
- [3] E. Fermi, “An attempt of a theory of beta radiation. 1,” *Zeitschrift fr Physik A Hadrons and Nuclei*, vol. 88, p. 161, 1934.
- [4] H. Bethe and R. Peierls, “The neutrino,” *Nature*, vol. 133, no. 3362, pp. 532–532, 1934.
- [5] F. Reines and C. Cowan, “A Proposed Experiment to Detect the Free Neutrino,” *Physical Review*, vol. 90, no. 3, pp. 492–493, 1953.
- [6] C. Cowan, F. Reines, F. Harrison, H. Kruse, and A. McGuire, “Detection of the free neutrino: A confirmation,” *Science*, vol. 124, no. 3212, p. 103, 1956.
- [7] L. Alvarez, *A proposed experiemental test of the neutrino theory*. [Lawrence] Radiation Laboratory, 1949.
- [8] F. Reines and C. Cowan Jr, “Neutrino physics,” *Physics Today*, vol. 10, p. 12, 1957.
- [9] N. Kemmer, “The charge-dependence of nuclear forces,” in *Proc. Cambridge Phil. Soc*, vol. 34, pp. 354–364, Cambridge Univ Press, 1938.
- [10] H. Yukawa, S. Sakata, and M. Taketani, “On the Interaction of Elementary Particles. III,” in *Proc. Phys.-Math. Soc. Japan*, vol. 20, pp. 319–340, 1938.

- [11] G. Danby, J. Gaillard, K. Goulianos, L. Lederman, N. Mistry, M. Schwartz, and J. Steinberger, “Observation of high-energy neutrino reactions and the existence of two kinds of neutrinos,” *Physical Review Letters*, vol. 9, no. 1, pp. 36–44, 1962.
- [12] M. Perl, G. Abrams, A. Boyarski, M. Breidenbach, D. Briggs, F. Bulos, W. Chinowsky, J. Dakin, G. Feldman, C. Friedberg, *et al.*, “Evidence for Anomalous Lepton Production in $e^+ - e^-$ Annihilation,” *Physical Review Letters*, vol. 35, no. 22, pp. 1489–1492, 1975.
- [13] M. Perl, G. Feldman, G. Abrams, M. Alam, A. Boyarski, M. Breidenbach, F. Bulos, W. Chinowsky, J. Dorfan, C. Friedberg, *et al.*, “Properties of anomalous $e \mu$ events produced in $e^+ e^-$ annihilation* 1,* 2,” *Physics Letters B*, vol. 63, no. 4, pp. 466–470, 1976.
- [14] M. Perl, “The tau heavy lepton—a recently discovered elementary particle,” *Nature*, vol. 275, pp. 273–278, 1978.
- [15] K. Kodama, N. Ushida, C. Andreopoulos, N. Saoulidou, G. Tzanakos, P. Yager, B. Baller, D. Boehnlein, W. Freeman, B. Lundberg, *et al.*, “Observation of tau neutrino interactions,” *Physics Letters B*, vol. 504, no. 3, pp. 218–224, 2001.
- [16] R. Davis Jr, D. Harmer, and K. Hoffman, “Search for neutrinos from the sun,” *Physical Review Letters*, vol. 20, no. 21, pp. 1205–1209, 1968.
- [17] J. Bahcall, N. Bahcall, and G. Shaviv, “Present Status of the Theoretical Predictions for the ^{36}Cl Solar-Neutrino Experiment,” *Physical Review Letters*, vol. 20, no. 21, pp. 1209–1212, 1968.
- [18] B. Cleveland, T. Daily, R. Davis Jr, J. Distel, K. Lande, C. Lee, P. Wildenhain, and J. Ullman, “Measurement of the solar electron neutrino flux with the Homestake chlorine detector,” *The Astrophysical Journal*, vol. 496, p. 505, 1998.

- [19] J. Bahcall, M. Pinsonneault, and G. Wasserburg, “Solar models with helium and heavy-element diffusion,” *Reviews of Modern Physics*, vol. 67, no. 4, p. 781, 1995.
- [20] S. Turck-Chieze and I. Lopes, “Toward a unified classical model of the sun—On the sensitivity of neutrinos and helioseismology to the microscopic physics,” *The Astrophysical Journal*, vol. 408, pp. 347–367, 1993.
- [21] I. Sackmann *et al.*, “Our sun. I - the standard model: Successes and failures,” *The Astrophysical Journal*, vol. 360, pp. 727–736, 1990.
- [22] B. Pontecorvo, “Mesonium and antimesonium,” *Zhur. Eksptl'. i Teoret. Fiz.*, vol. 33, 1957.
- [23] Z. Maki, M. Nakagawa, and S. Sakata, “Remarks on the unified model of elementary particles,” *Progress of Theoretical Physics*, vol. 28, no. 5, pp. 870–880, 1962.
- [24] B. Pontecorvo, “Neutrino experiments and the problem of conservation of leptonic charge,” *Soviet Journal of Experimental and Theoretical Physics*, vol. 26, p. 984, 1968.
- [25] V. Gribov and B. Pontecorvo, “Neutrino astronomy and lepton charge,” *Physics Letters B*, vol. 28, no. 7, pp. 493–496, 1969.
- [26] S. Eidelman *et al.*, “Particle Data Group,” *Physics Letters B*, vol. 592, no. 1, p. 15, 2004.
- [27] M. Doi, T. Kotani, and E. Takasugi, “Double beta decay and Majorana neutrino, Prog,” *Theoretical Physics Supplement*, vol. 83, no. 1, 1985.
- [28] J. Levy, “On the derivation of the neutrino oscillation length formula,” *Arxiv preprint hep-ph/0004221*, 2000.

- [29] L. Wolfenstein, “Neutrino oscillations in matter,” *Physical Review D*, vol. 17, no. 9, p. 2369, 1978.
- [30] S. Mikheyev and A. Smirnov, “Resonance amplification of oscillations in matter and spectroscopy of solar neutrinos,” *Soviet Journal of Nuclear Physics*, vol. 42, p. 913, 1985.
- [31] M. Tórtola, J. Valle, and D. Vanegas, “Global status of neutrino oscillation parameters after recent reactor measurements,” *Arxiv preprint arXiv:1205.4018*, 2012.
- [32] P. Vogel, “Neutrinoless double beta decay,” in *Intersections of Particle and Nuclear Physics: 9th Conference CIPAN2006*, vol. 870, pp. 124–131, 2006.
- [33] B. Pritychenko, “On double-beta decay half-life time systematics,” *Arxiv preprint arXiv:1004.3280*, 2010.
- [34] H. Klapdor-Kleingrothaus and I. Krivosheina, “The evidence for the observation of $0\nu\beta\beta$ decay,” *Modern Physics Letters A*, vol. 21, no. 20, pp. 1547–1566, 2006.
- [35] K. Zuber, “Neutrinoless double beta decay,” *Neutrinos in Particle Physics, Astrophysics and Cosmology*, vol. 61, p. 287, 2008.
- [36] N. Ackerman, B. Aharmim, M. Auger, D. Auty, P. Barbeau, K. Barry, L. Bartoszek, E. Beauchamp, V. Belov, C. Benitez-Medina, *et al.*, “Observation of two-neutrino double-beta decay in Xe-136 with EXO-200,” *Arxiv preprint arXiv:1108.4193*, 2011.
- [37] M. Auger, D. Auty, P. Barbeau, E. Beauchamp, V. Belov, C. Benitez-Medina, M. Breidenbach, T. Brunner, A. Burenkov, B. Cleveland, *et al.*, “Search for Neutrinoless Double-Beta Decay in ^{136}Xe with EXO-200,” *Arxiv preprint arXiv:1205.5608*, 2012.

- [38] V. Rodin, A. Faessler, F. Simkovic, and P. Vogel, “Assessment of uncertainties in QRPA $0\nu\beta\beta$ -decay nuclear matrix elements,” *Nuclear Physics A*, vol. 766, pp. 107–131, 2006.
- [39] E. Caurier, J. Menéndez, F. Nowacki, and A. Poves, “Influence of pairing on the nuclear matrix elements of the neutrinoless $\beta\beta$ decays,” *Physical Review Letters*, vol. 100, no. 5, p. 52503, 2008.
- [40] L. Kaufman, “Searching for double beta decay with the Enriched Xenon Observatory,” in *Journal of Physics: Conference Series*, vol. 203, p. 012067, IOP Publishing, 2010.
- [41] J. Curry, “Compilation of wavelengths, energy levels, and transition probabilities for Ba I and Ba II,” *Journal of Physical and Chemical Reference Data*, vol. 33, no. 3, pp. 725–746, 2004.
- [42] S. Niggli and M. Huber, “Transition probabilities in neutral barium,” *Physical Review A*, vol. 35, no. 7, p. 2908, 1987.
- [43] W. Nagourney, J. Sandberg, H. Dehmelt, *et al.*, “Shelved optical electron amplifier: Observation of quantum jumps,” *Physical Review Letters*, vol. 56, no. 26, pp. 2797–2799, 1986.
- [44] N. Yu, W. Nagourney, and H. Dehmelt, “Radiative lifetime measurement of the Ba^+ metastable $D_{3/2}$ state,” *Physical Review Letters*, vol. 78, no. 26, pp. 4898–4901, 1997.
- [45] A. Gallagher, “Oscillator strengths of Ca II, Sr II, and Ba II,” *Physical Review*, vol. 157, no. 1, p. 24, 1967.

- [46] M. Davidson, L. Snoek, H. Volten, and A. Dönszelmann, “Oscillator strengths and branching ratios of transitions between low-lying levels in the barium II spectrum,” *Astronomy and Astrophysics*, vol. 255, p. 457, 1992.
- [47] N. Kurz, M. Dietrich, G. Shu, R. Bowler, J. Salacka, V. Mirgon, and B. Blinov, “Measurement of the branching ratio in the $6P_{3/2}$ decay of Ba II with a single trapped ion,” *Physical Review A*, vol. 77, no. 6, p. 060501, 2008.
- [48] J. E. Sansonetti and J. J. Curry, “Wavelengths, transition probabilities, and energy levels for the spectra of barium (Ba III through Ba LVI),” *Journal of Physical and Chemical Reference Data*, vol. 39, p. 043103, 2010.
- [49] E. Saloman, “Energy levels and observed spectral lines of xenon, Xe I through Xe LIV,” *Journal of Physical and Chemical Reference Data*, vol. 33, no. 3, pp. 765–922, 2004.
- [50] C. Crepin-Gilbert and A. Tramer, “Photophysics of metal atoms in rare-gas complexes, clusters and matrices,” *International Reviews in Physical Chemistry*, vol. 18, no. 4, pp. 485–556, 1999.
- [51] C. Jouvét, C. Lardeux-Dedonder, S. Martrenchard, and D. Solgadi, “Fluorescence excitation spectrum of silver–argon van der Waals complex,” *The Journal of Chemical Physics*, vol. 94, p. 1759, 1991.
- [52] M. McGuirk, L. Viehland, E. Lee, W. Breckenridge, C. Withers, A. Gardner, R. Plowright, and T. Wright, “Theoretical study of Ba–RG (RG= rare gas) complexes and transport of Ba through RG ($n= 1, 2$; RG= He–Rn),” *The Journal of Chemical Physics*, vol. 130, p. 194305, 2009.
- [53] S. Panov, J. Williamson, and T. Miller, “The electronic spectroscopy of the Ba^+ -Ar complex: Potential surface and dissociation energies,” *Journal of Chemical Physics*, vol. 102, no. 19, pp. 7359–7368, 1995.

- [54] S. Xantheas, G. Fanourgakis, S. Farantos, and M. Velegrakis, "Spectroscopic constants of the X Σ and A Π states of Sr+Ar from first principles: Comparison with experiment," *The Journal of Chemical Physics*, vol. 108, p. 46, 1998.
- [55] E. Whittle, D. Dows, and G. Pimentel, "Matrix isolation method for the experimental study of unstable species," *The Journal of Chemical Physics*, vol. 22, p. 1943, 1954.
- [56] P. Lahr and W. Eversole, "Compression Isotherms of Argon, Krypton, and Xenon Through the Freezing Zone.," *Journal of Chemical and Engineering Data*, vol. 7, no. 1, pp. 42–47, 1962.
- [57] D. Sears and H. Klug, "Density and expansivity of solid xenon," *The Journal of Chemical Physics*, vol. 37, p. 3002, 1962.
- [58] E. Becker and G. Pimentel, "Spectroscopic studies of reactive molecules by the matrix isolation method," *The Journal of Chemical Physics*, vol. 25, p. 224, 1956.
- [59] D. Maillard, A. Schriver, J. Perchard, C. Girardet, and D. Robert, "HX, N double doping experiments in monatomic matrices: Near infrared spectra and symmetry properties of the intermolecular potential," *The Journal of Chemical Physics*, vol. 67, p. 3917, 1977.
- [60] H. Reyher, H. Bauer, C. Huber, R. Mayer, A. Schäfer, and A. Winnacker, "Spectroscopy of barium ions in He II," *Physics Letters A*, vol. 115, no. 5, pp. 238–244, 1986.
- [61] P. Kasai, "Generation and Trapping of Charged Species in Rare-Gas Matrix at 4 K: esr spectra of Cd⁺, Cr⁺, and Mn⁺," *Physical Review Letters*, vol. 21, no. 2, pp. 67–69, 1968.

- [62] V. Bondybey and J. English, “Ion–matrix interactions: Optical spectrum of the Ca cation in solid argon,” *The Journal of Chemical Physics*, vol. 75, p. 492, 1981.
- [63] G. Zizak, J. Bradshaw, and J. Winefordner, “Rate equation solution for the temporal behavior of a three-level system,” *Applied Optics*, vol. 19, no. 21, pp. 3631–3639, 1980.
- [64] D. M. Lindsay, F. Meyer, and W. Harbich, “Neutralization and matrix deposition experiments on mass-selected silver atoms and clusters,” *Zeitschrift für Physik D Atoms, Molecules and Clusters*, vol. 12, pp. 15–18, 1989. 10.1007/BF01426896.
- [65] A. Kolmakov and V. Stankevich, “Inelastic interaction of low-energy mass-selected ions with a surface of solid xenon,” *Low Temperature Physics*, vol. 20, p. 926, 1994.
- [66] K. Waldeer and H. Urbassek, “keV-atom bombardment of condensed rare gases: Molecular dynamics simulation,” *Nuclear Instruments and Methods in Physics Research Section B: Beam Interactions with Materials and Atoms*, vol. 73, no. 1, pp. 14–28, 1993.
- [67] M. Menzinger and L. Wåhlin, “High Intensity, Low Energy Spread Ion Source for Chemical Accelerators,” *Review of Scientific Instruments*, vol. 40, no. 1, pp. 102–105, 2009.
- [68] Colutron Research Corporation, 2321 Yarmouth Ave. Boulder, CO 80301 USA, *Colutron Ion Gun Assemblies*.
- [69] R. G. Wilson and G. R. Brewer, *Ion Beams; with Applications to Ion Implantation*. Wiley, 1973.
- [70] L. Wåhlin, “The Colutron, a Zero Deflection Isotope Separator,” *Nuclear Instruments and Methods*, vol. 27, no. 1, pp. 55–60, 1964.

- [71] A. Adams and F. Read, “Electrostatic cylinder lenses II: Three element einzel lenses,” *Journal of Physics E: Scientific Instruments*, vol. 5, p. 150, 1972.
- [72] R. D. LaBelle, *Isotopically selective atom counting using photon burst mass spectrometry*. Colorado State University Thesis/Dissertation, Colorado State University, 1993.
- [73] Spellman High Voltage Electronics Corporation, 475 Wireless Boulevard, Hauppauge, NY 11788, *Bertan 602C High Voltage Module*.
- [74] H. Wollnik, *Optics of charged particles*. Academic Press Inc., Orlando, FL, 1987.
- [75] S. Ramo, “Currents induced by electron motion,” *Proceedings of the IRE*, vol. 27, no. 9, pp. 584–585, 2006.
- [76] B. Mong, *Barium Tagging in Solid Xenon for the EXO Experiment*. Colorado State University Thesis/Dissertation, Colorado State University, 2011.
- [77] W. Driscoll, *Handbook of Optics*. McGraw-Hill Companies, 1978.
- [78] A. Dobi, C. Hall, S. Herrin, A. Odian, C. Prescott, P. Rowson, N. Ackerman, B. Aharmin, M. Auger, P. Barbeau, *et al.*, “A xenon gas purity monitor for EXO,” *Nuclear Instruments and Methods in Physics Research Section A: Accelerators, Spectrometers, Detectors and Associated Equipment*, 2011.
- [79] A. Allouche, M. Aubert-Frécon, G. Nicolas, and F. Spiegelmann, “Theoretical study of the electronic structure of the Ba₂ molecule,” *Chemical Physics*, vol. 200, no. 1-2, pp. 63–77, 1995.
- [80] B. S. Ault and L. Andrews, “Infrared spectra of alkaline earth metal oxides and superoxides isolated in nitrogen matrices,” 1974.
- [81] L. Andrews, J. Yustein, C. Thompson, and R. Hunt, “Reactions of Pulsed-Laser Evaporated Ca, Sr, and Ba Atoms with O₂. Infrared Spectra of the Metal Oxides,

- Oxide Dimers, Dioxides, and Peroxides in Solid Argon,” *The Journal of Physical Chemistry*, vol. 98, no. 26, pp. 6514–6521, 1994.
- [82] U. Magg, H. Birk, and H. Jones, “The ground-state infrared spectrum of four isotopic forms of barium monohydride (BaH),” *Chemical Physics Letters*, vol. 149, no. 3, pp. 321–325, 1988.
- [83] A. Allouche, F. Spiegelmann, and M. Aubert-Frécon, “Theoretical study of the low-lying electronic states of the BaH⁺ molecular ion,” *Chemical Physics Letters*, vol. 204, no. 3-4, pp. 343–349, 1993.
- [84] X. Wang and L. Andrews, “Metal dihydride (MH₂) and dimer (M₂H₄) structures in solid argon, neon, and hydrogen (M= Ca, Sr, and Ba): Infrared spectra and theoretical calculations,” *The Journal of Physical Chemistry A*, vol. 108, no. 52, pp. 11500–11510, 2004.
- [85] S. Kinsey-Nielsen, C. Brazier, and P. Bernath, “Rotational analysis of the B Σ –X Σ transition of BaOH and BaOD,” *The Journal of Chemical Physics*, vol. 84, p. 698, 1986.
- [86] J. Sepioł, A. Starukhin, R. Kołos, T. Latychevskaia, J. Jasny, A. Renn, and U. Wild, “Detection and spectroscopy of single molecules in rare gas matrices: dibenzanthanthrene in krypton and xenon,” *Chemical Physics Letters*, vol. 311, no. 1, pp. 29–35, 1999.
- [87] M. Montero Díez, K. Twelker, W. Fairbank, G. Gratta, P. Barbeau, K. Barry, R. DeVoe, M. Dolinski, M. Green, F. LePort, *et al.*, “A simple radionuclide-driven single-ion source,” *Review of Scientific Instruments*, vol. 81, no. 11, p. 113301, 2010.